Monthly Notices of the ROYAL ASTRONOMICAL SOCIETY

MNRAS **541,** 2674–2706 (2025) https://doi.org/10.1093/mnras/staf1113
Advance Access publication 2025 July 10

The Type I superluminous supernova catalogue – II. Spectroscopic evolution in the photospheric phase, velocity measurements, and constraints on diversity

Aysha Aamer [1★] Matt Nicholl [1] Sebastian Gomez [2] Edo Berger [2,3] Peter Blanchard [2] Joseph P. Anderson [4,5] Charlotte Angus [1] Amar Aryan [6] Chris Ashall [7] Ting-Wan Chen [6] Georgios Dimitriadis [8] Lluís Galbany [9,10] Anamaria Gkini [11] Mariusz Gromadzki [12] Claudia P. Gutiérrez [10,9] Daichi Hiramatsu [2,3] Griffin Hosseinzadeh [13] Cosimo Inserra [14] Amit Kumar [15,16] Harsh Kumar [2] Hanindyo Kuncarayakti [17,18] Giorgos Leloudas [19] Paolo Mazzali,[20,21] Kyle Medler [7] Tomás E. Müller-Bravo [22,23] Mauricio Ramirez,[24,5] Aiswarya Sankar.K [6] Steve Schulze [25] Avinash Singh [11] Jesper Sollerman [11] Shubham Srivastav [26] Jacco H. Terwel [22] and David R. Young [1]

Affiliations are listed at the end of the paper

Accepted 2025 July 1. Received 2025 June 13; in original form 2025 March 27

ABSTRACT

Hydrogen-poor superluminous supernovae (SLSNe) are among the most energetic explosions in the universe, reaching luminosities up to 100 times greater than those of normal supernovae. This paper presents the largest compilation of SLSN photospheric spectra to date, encompassing data from the advanced Public ESO Spectroscopic Survey of Transient Objects (ePESSTO+), the Finding Luminous and Exotic Extragalactic Transients (FLEET) search, and all published spectra up to December 2022. The data set includes a total of 974 spectra of 234 SLSNe. By constructing average phase binned spectra, we find SLSNe initially exhibit high temperatures (10 000−11 000 K), with blue continua and weak lines. A rapid transformation follows, as temperatures drop to 5000−6000 K by 40 d post-peak, leading to stronger P-Cygni features. Variance within the data set is slightly reduced when defining the phase of spectra relative to explosion, rather than peak, and normalising to the population's median e-folding decline time. Principal Component Analysis (PCA) supports this, requiring fewer components to explain the same level of variation when binning data by scaled days from explosion, suggesting a more homogeneous grouping. Using PCA and K-means clustering, we identify outlying objects with unusual spectroscopic evolution and evidence for energy input from interaction, but find no support for groupings of two or more statistically significant subpopulations. We find Fe II λ5169 line velocities closely track the radius implied from blackbody fits, indicating formation near the photosphere. We also confirm a correlation between velocity and velocity gradient, which can be explained if all SLSNe are in homologous expansion but with different scale velocities. This behaviour aligns with expectations for an internal powering mechanism.

Key words: stars: massive – supernovae: general – transients: supernovae.

1 INTRODUCTION

Hydrogen-poor superluminous supernovae (SLSNe) are some of the brightest explosions in the universe, releasing 10−100 times more energy than normal supernovae, and spanning over hundreds of days (e.g. Barbary et al. 2009; Gal-Yam et al. 2009; Chomiuk et al. 2011; Quimby et al. 2011; Inserra 2019; Gal-Yam 2019a; Nicholl 2021; Gomez et al. 2024; Moriya 2024). Originally, these events were defined as any events with an absolute magnitude brighter than −21. However, this strict cut-off has now been relaxed to include fainter events that still look spectroscopically similar. Understanding, the physical mechanisms behind these extraordinarily bright explosions is one of the major unsolved problems in stellar astrophysics. Despite significant observational efforts, the origins and powering mechanisms of SLSNe remain elusive, signalling that we lack a complete understanding of stellar life cycles, particularly at the upper end of the powering scale.

Spectroscopically, H-poor SLSNe-I (hereafter SLSN) are characterized by a steep blue continuum, often alongside a series of singly ionized oxygen (O II) absorption lines, indicating extremely high temperatures and non-thermal excitation at early times (Dessart et al. 2012; Mazzali et al. 2016). These lines found between 3737 and 4650 Å (Quimby et al. 2018; Gal-Yam 2019b) produce a

★ E-mail: aaamer01@ads.qub.ac.uk

characteristic W-shape that weakens with time as the temperature of the photosphere drops (Quimby et al. 2011). However, some SLSNe do not show these O II absorption lines (e.g. Gutiérrez et al. 2022). During this photospheric phase, the spectrum is dominated by blackbody radiation from the hot, dense photosphere of the SN, with absorption features from elements in the outer ejecta (e.g. Pastorello et al. 2010; Howell et al. 2013; Inserra et al. 2013; Nicholl et al. 2016a). As the temperature drops, the spectra increasingly resemble those of traditional stripped envelope SNe (SE-SNe) at the same temperatures, likely indicating similar progenitors or environments between the two classes (Pastorello et al. 2010). As the ejecta expand and cool, the SN transitions to the nebular phase where the photosphere becomes optically thin and stops producing continuous blackbody emission. Instead, the spectrum is dominated by emission lines from elements such as oxygen and magnesium (Gal-Yam et al. 2009; Nicholl et al. 2016b; Jerkstrand et al. 2017; Nicholl et al. 2019a).

Although their star-forming environments (Neill et al. 2011; Chen et al. 2013; Lunnan et al. 2014; Leloudas et al. 2015; Angus et al. 2016; Perley et al. 2016; Schulze et al. 2018) point to the explosions of massive stars, there are still many questions regarding their powering mechanisms. The light-curve evolution for typical SE-SNe is dictated by the decay of ^{56}Ni produced in the explosion (Colgate & McKee 1969). The mass of ^{56}Ni produced by typical SE-SNe is $\lesssim 0.2\,M_\odot$ (e.g. Drout et al. 2011; Anderson 2019; Rodríguez, Maoz & Nakar 2023). For SLSNe, several solar masses of ^{56}Ni would be needed to power such a long duration light curve, as well as power the peak luminosities observed. Observations of SLSNe suggest total ejecta masses ranging from a few up to a few tens of solar masses (Blanchard et al. 2020a; Gomez et al. 2024), which would often result in ejecta compositions dominated by nickel. This is not supported by SLSN spectra, which are dominated by intermediate mass elements such as carbon and oxygen (Dessart et al. 2012). The amount of nickel needed could be synthesized in pair-instability SNe (PISNe), which are theorized to occur in main sequence stars with masses 140–260 $M_\odot$. In these stars, spontaneous pair production of electron and positron pairs can reduce the internal radiation pressure, resulting in explosion of a PISN with over 100 $M_\odot$ of ejecta (Barkat, Rakavy & Sack 1967; Heger & Woosley 2002). These explosions could have been more common in the very early universe when the metallicity was lower and stars could retain more mass (Bromm & Larson 2004; Woosley, Blinnikov & Heger 2007). So far the only promising candidate for this mechanism is SN 2018ibb (Schulze et al. 2024). Instead another mechanism is needed to power most SLSNe. Current theories propose a range of both internal and external powering mechanisms.

A possible explanation for the powering mechanism of SLSNe is interaction with circumstellar material (CSM). This theory also proposes an SE-SN that has large amounts of CSM created through stellar winds and ejections throughout the stars life (Chevalier & Irwin 2011; Chatzopoulos, Wheeler & Vinko 2012, 2013). Pulsational pair instability (PPI) is a mechanism thought to occur in lower mass stars (95–130 $M_\odot$) than required for PISNe where the star ejects material towards the end of its life due to pair instability; this has been suggested as a way to get massive CSM in interaction models (Woosley et al. 2007). The SN ejecta are able to catch up to this material because they have much higher velocities, and are rapidly decelerated if the CSM is massive enough. This creates a shock that deposits energy in the ejecta and CSM, the cooling of which can produce a bright and long-lived light curve (Smith et al. 2007; Chevalier & Irwin 2011; Ginzburg & Balberg 2012; Moriya et al. 2013; Sorokina et al. 2016). Interaction with CSM is the mechanism thought to power H-rich SLSNe-II (Kangas et al. 2022; Hiramatsu et al. 2024), but is less easily reconciled with H-poor SLSNe-I. Several PPI candidates exist showing a variety of different observables such as multipeaked light curves (e.g. Bose et al. 2018; Gomez et al. 2019; Hosseinzadeh et al. 2022; Wang et al. 2022; Zhu et al. 2023), early emission of 'nebular' lines (e.g. Aamer et al. 2024; Angus et al. 2024), discovery of late time interaction with H (e.g. Yan et al. 2017b), or the discovery of CSM shells through Mg II absorption lines (e.g. Lunnan et al. 2018a; Schulze et al. 2024; Gkini et al. 2025).

The most popular theory, with observational support particularly from late-time observations, is the magnetar central engine model. In this picture, a high-mass star undergoes an SN explosion at the end of its life much like a typical core collapse SN (CCSN). However, in this case the remnant is a fast rotating neutron star with a very strong magnetic (B) field (around $10^{13} - 10^{14}$ G) called a magnetar (Kasen & Bildsten 2010; Woosley 2010; Dexter & Kasen 2013; Metzger et al. 2015). Although these are very strong B-fields, nearly 10 per cent of newly born neutron stars have B-fields in the range $10^{13} - 10^{15}$ G lasting over 1000 yr after their birth, so it is plausible that these could exist to produce SLSNe (Kouveliotou et al. 1998; Woods & Thompson 2006). As these magnetars spin down, they inject energy into the system, powering the observed light curves. If the initial spin period is close to maximal, around a few milliseconds, the energy released is sufficient to boost the luminosity to the levels observed in SLSNe (Ostriker & Gunn 1971; Kasen & Bildsten 2010). There is also growing evidence that some CCSNe at peak luminosity are not solely powered by radioactive ^{56}Ni decay, and instead require the presence of a central engine such as a magnetar (Rodríguez, Nakar & Maoz 2024). If true, this would support the presence of magnetars in SLSNe. Despite the magnetar model being widely applied to SLSNe (e.g. Inserra et al. 2013; Nicholl, Guillochon & Berger 2017c), multiple powering mechanisms may be at play (Chen et al. 2023a), depending on the progenitor star and its environment.

SLSNe show striking diversity in their observed properties with some events reaching peak absolute magnitudes as bright as $M = -22.5$ (Gomez et al. 2024). Similarly, their light curves can vary vastly in duration from around 50 to over 600 d (Nicholl et al. 2015a; De Cia et al. 2018; Lunnan et al. 2018b; Angus et al. 2019; Chen et al. 2023b). This variability extends to the mass of material ejected in the explosion, which can range from a few solar masses, up to around 40 solar masses in most SLSNe (Blanchard et al. 2020a; Chen et al. 2023b; Gomez et al. 2024). However, this number can reach up to 100 $M_\odot$ like in the case of SN 2018ibb (Schulze et al. 2024). Understanding this diversity is key to determining whether SLSNe represent a single class of explosion or whether they encompass multiple sub-types. This observed diversity may also point to the possibility of multiple progenitor channels.

A key question is whether SLSNe represent an extension of normal SNe Ic (Pastorello et al. 2010; Inserra et al. 2013; Metzger et al. 2015; Liu, Modjaz & Bianco 2017; Gomez et al. 2022a). These are stripped envelope SNe without H or He lines present. Spectroscopically, H-poor SLSNe share some similarities with SNe Ic, especially in the late-time nebular phase (Nicholl et al. 2019a; Gutiérrez et al. 2022) when the ejecta becomes optically thin and individual element lines dominate the spectrum. However, the extreme luminosity and extended light curves of SLSNe require an additional, long-term heating source compared to the ^{56}Ni that powers normal SNe Ic. Moreover, unlike typical SNe Ic, SLSNe occur almost exclusively in low-metallicity galaxies (Chen et al. 2013; Lunnan et al. 2013, 2014; Leloudas et al. 2015; Perley et al. 2016; Schulze et al. 2018; Cleland, McGee & Nicholl 2023). This likely influences the distribution of

natal stellar masses, and the loss of mass and angular momentum prior to explosion.

The spectroscopic evolution of SLSNe is key to understanding their origins, and the diversity of this class necessitates a statistical approach with large samples of objects. For example, recent work from the Zwicky Transient Facility (ZTF; Bellm et al. 2019) contains a sample of 78 SLSNe, focusing on the photometry and light curves of these events, with spectra used to derive photospheric velocities (Chen et al. 2023a, b). A study by Lunnan et al. (2018b) analyses the light curves and spectra of 17 SLSNe from the Panoramic Survey Telescope and Rapid Response System (Pan-STARRS1; Chambers et al. 2016) Medium Deep Survey. However, the spectral analysis in that work was again limited to expansion velocities derived from the spectra. A more comprehensive study was conducted by Quimby et al. (2018) on spectra of 23 objects from the Palomar Transient Facility (PTF; Rau et al. 2009). That work looked at specific features within the spectra such as the ionized Mn II and O II lines, how they evolved with time and analysed the velocity distributions of different element absorption lines. A sample of 12 events with 41 spectra from Nicholl et al. (2019a) focussed only on the nebular phase. Other studies have looked at the possibility of subpopulations within the class such as Inserra et al. (2018) who analysed the photometric evolution in combination with spectroscopic properties of 22 SLSNe. Work by Könyves-Tóth & Vinkó (2021) claimed differences between fast and slow events for 28 SLSNe based on photospheric velocities and the appearance of O II absorption lines. Another study of note is the work by Liu et al. (2017) looking at spectral similarities between 32 SLSNe, 17 normal SNe Ic, and 21 broad-lined SNe Ic (Ic-BL), with particular focus on the Fe II λ5169 line. That work found similarities between SLSNe and SNe Ic-BL that displayed similar absorption velocities and line widths, compared to SNe Ic that had systematically lower velocities and narrower lines. This raises the question of whether these classes are distinct populations or if they exist on a smooth continuum.

In this paper, we present a sample of 974 spectra from 234 H-poor SLSNe. This is the second paper in our series analysing the largest data set to date of SLSNe, and constitutes the second data release, focusing on the photospheric spectra. In the first data release, Gomez et al. (2024) present photometry and light-curve modelling of 262 SLSNe. The final data release, featuring late-time nebular spectra (Blanchard et al. in preparation), will serve as the third instalment. This data will be publicly available on Github,[1] and in the supplementary material of this journal. Previously unpublished raw spectra will also be publicly uploaded to the Weizmann Interactive Supernova Data Repository (WISeREP[2]).

The paper is structured as follows. Section 2 describes where the data was collected from, how it was processed, and key properties of the sample. Section 3 analyses the average spectra in different time bins, as well as general line identifications. In Section 4, we discuss potential subpopulations of SLSNe based on their spectra. Section 5 presents our measurements and analysis of the key spectral line Fe II λ5169, and how it compares to the photospheric velocity. We present our conclusions in Section 6.

2 SLSN SAMPLE

2.1 Data collection

In total this collective study contains data from 234 events with 1252 spectra collected and reduced from public and private sources detailed below. The focus of this paper is on the photospheric phase of the SN where the spectra are dominated by blackbody emission and absorption lines. For the scope of this paper, we limit this to spectra with a phase of up to 200 d post-explosion, or corresponding phases up to +160 d relative to the *r*-band peak of the light curve, both defined in Gomez et al. (2024). This results in 974 photospheric spectra used in the analysis of this paper after applying the phase cuts and coadding spectra from the same instrument on the same day. These spectra will be made available in the data release alongside this paper.

This sample contains fewer objects than Gomez et al. (2024) as some objects in that sample do not have publicly available spectra or are due to be published in future works. The majority of the public data consisting of 1064 spectra were obtained from WISeREP, and the Transient Name Server (TNS[3]), with 32 obtained through private communications such as spectra of SN 2002gh, SN 2011kl, SN 1999as, and those from Lunnan et al. (2018b). 82 private spectra were obtained through the extended-Public ESO Spectroscopic Survey for Transient Objects (ePESSTO+) (Smartt et al. 2015), and 74 spectra from the Finding Luminous and Exotic Extragalactic Transients (FLEET) search (Gomez et al. 2020a, 2023a).

All spectra from PESSTO, ePESSTO, and ePESSTO+ were obtained using the 3.56m European Southern Observatory New Technology Telescope (ESO NTT) at La Silla Observatory in Chile, with Grisms 11, 13, and 16. All spectra were reduced using the PESSTO pipeline[4] (Smartt et al. 2015). Spectra dating up to 2019 April have been obtained from PESSTO Spectroscopic Data Releases 1–4. We also include in our analysis previously unpublished spectra from ePESSTO+ shown in Table 1.

Spectra collected through the FLEET follow-up programme were obtained using both the Blue Channel (Schmidt, Weymann & Foltz 1989) and Binospec (Fabricant et al. 2019) on the MMT 6.5m Telescope, the Low Dispersion Survey Spectrograph (LDSS3c; Stevenson et al. 2016) and the Inamori-Magellan Areal Camera and Spectrograph (IMACS; Dressler et al. 2011) on the Magellan 6.5m telescopes, as well as the FAst Spectrograph for the Tillinghast Telescope (FAST; Fabricant et al. 1998) on the 1.5m Tillinghast Telescope. The objects with unpublished spectra are shown in Table 1.

2.2 Data processing

After obtaining all the available 1D spectra for this sample, the data were required to be standardized and processed into a homogeneous data set.

The first step was to remove telluric absorption lines due to the Earth's atmosphere; this was done using the PYTHON package tellurics-begone.[5] This package works by convolving model spectra of H_2O and O_2 with each spectrum and subtracting them off. If a spectral resolution was specified in the original file headers, this value was used, otherwise a default value of 10 Å was used. This process was also only applied to spectra with any flux between 4000

[1] https://github.com/gmzsebastian/SLSNe
[2] https://www.wiserep.org
[3] https://www.wis-tns.org
[4] https://github.com/svalenti/pessto
[5] https://github.com/EJRidley/tellurics-begone

Table 1. Objects with previously unpublished spectra included in this sample, the number of spectra included, and the data source.

Object	Spectra	Source
SN 2018bym	2	FLEET
SN 2018cxa	2	FLEET
SN 2018fcg	2	FLEET
SN 2018fd	1	FLEET
SN 2018ffs	1	FLEET
SN 2018lfe	4	FLEET
SN 2019gfm	5	PESSTO
SN 2019gqi	3, 1	PESSTO, FLEET
SN 2019itq	4	FLEET
SN 2019kcy	5	PESSTO
SN 2019nhs	4	PESSTO
SN 2019otl	2	FLEET
SN 2019pvs	2	FLEET
SN 2019sgh	1	FLEET
SN 2019ujb	2	FLEET
SN 2019unb	11	PESSTO
SN 2019une	1	FLEET
SN 2020abjc	1	FLEET
SN 2020abjx	2	PESSTO
SN 2020adkm	1, 2	PESSTO, FLEET
SN 2020ank	7	PESSTO
SN 2020myh	1	FLEET
SN 2020qlb	1	FLEET
SN 2020rmv	1	FLEET
SN 2020uew	16	PESSTO
SN 2020xgd	4	FLEET
SN 2020wnt	4	FLEET
SN 2020znr	7	FLEET
SN 2020zzb	1	FLEET
SN 2021een	3, 1	PESSTO, FLEET
SN 2021ek	4	PESSTO
SN 2021fpl	2, 2	PESSTO, FLEET
SN 2021hpx	1	PESSTO
SN 2021txk	2	FLEET
SN 2021uvy	11, 3	FLEET
SN 2021vuw	4	FLEET
SN 2021xfu	2	FLEET
SN 2021ybf	1, 1	PESSTO, FLEET
SN 2021ynn	2	FLEET
SN 2021zcl	13, 3	PESSTO, FLEET
SN 2022le	2	FLEET
SN 2022lxd	1	FLEET
SN 2022npq	1	PESSTO
SN 2022pjq	1	FLEET
SN 2022vxc	3, 1	PESSTO, FLEET
SN 2022ued	1	FLEET

and 10 000 Å, as the model spectra of H_2O and O_2 only covered this wavelength range.

The data were then corrected for Galactic extinction with the host galaxy extinction assumed to be negligible. This is typically a reasonable assumption for SLSNe, as the host galaxies are very low mass (Lunnan et al. 2014) and light curve studies find extinctions consistent with zero (Nicholl et al. 2017c). This was done using values from Schlafly & Finkbeiner (2011) and using the implementation of the Gordon et al. (2023) extinction law in ASTROPY (Astropy Collaboration et al. 2018). This uses four representative samples of extinction curves and combines them into an extinction relation from 912 Å in the far UV, up to 32μm in the MIR (Gordon, Cartledge & Clayton 2009; Fitzpatrick et al. 2019; Gordon et al. 2021; Decleir et al. 2022). The visual extinction to reddening ratio was assumed to be $R_V = 3.1$.

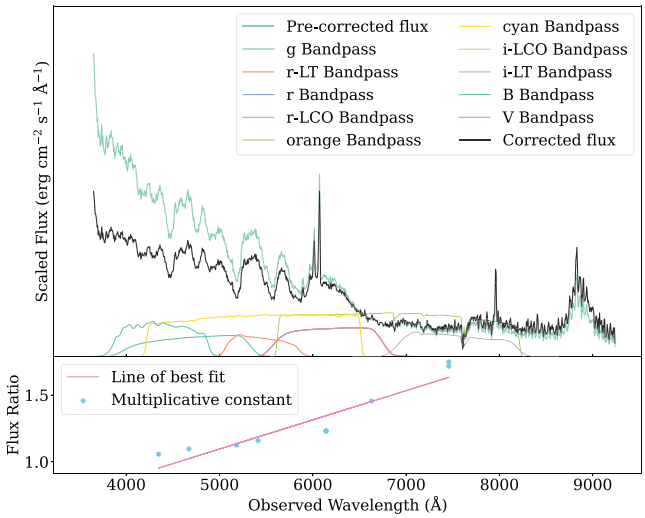

Figure 1. Flux correction (mangling) of an example spectrum of SN 2019szu (Aamer et al. 2024). Top: In green is the pre-corrected spectrum of SN 2019szu. The filter passbands used for the correction are overlaid. The black line represents the flux corrected spectrum. Both spectra are normalized to their median values and remain uncorrected for redshift at this stage of processing. Bottom: The cyan points indicate the multiplicative constants required in each filter passband to align the observed spectrum with the photometry from Gomez et al. (2024), plotted against the effective wavelength of each filter. These constants correspond to the ratio of the spectral derived flux and model fluxes in each passband. The pink line shows the line of best fit, which is used to scale the spectrum for flux correction by extending it over the full wavelength range of the spectrum.

The spectra were then flux calibrated in a process called 'mangling' (Hsiao et al. 2007) to model photometry from Gomez et al. (2024). The real photometry is host subtracted as described in Gomez et al. (2024). This data was first vetted and cleaned by removing points with errors larger than 0.2 mag. For flux calibration, we only used bands that had at least one data point meeting this criterion. Filter passbands were obtained for each band from the SVO filter profile server.[6] We caveat that some of the filters obtained from SVO do not account for atmospheric absorption. The integrated flux in each of the bandpasses with a full overlap with the target spectrum was measured and this was compared with the observed flux in each band. The ratio of these values is plotted in Fig. 1 against the effective wavelength in each band for an example spectrum of SN 2019szu. Calculating a linear fit to these ratios indicated the correction needed to be applied to the entire spectrum to calibrate to the photometry. If only one band fit the criteria then the multiplicative constant for that band was applied to the entire target spectrum. Fig. 1 shows in green the original, uncorrected spectrum of SN 2019szu, and in black the flux-corrected spectrum. The wavelengths of the spectra were then redshift corrected, using the redshifts from Gomez et al. (2024). These values were verified spectroscopically where possible.

The last step was to co-add spectra obtained from the same telescope and instrument in the same night if they were obtained with the same observing set-up (i.e. the same grism, grating or arm). As the spectra were already flux corrected, this was done by interpolating the fluxes onto the same wavelength grid and then averaging them.

[6]http://svo2.cab.inta-csic.es/theory/fps/

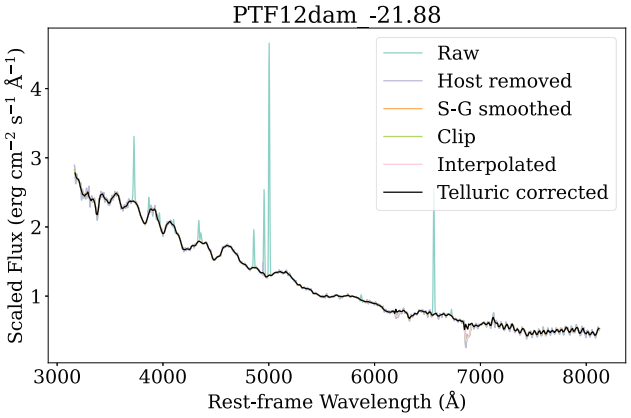

Figure 2. Spectrum of PTF12dam at a phase of −21.88 d with respect to peak. The figure illustrates the steps applied at the post-processing stage to all spectra with host galaxy line removal, Savitzky–Golay smoothing, clipping the edges of the spectra if needed, telluric removal, and interpolating and remapping onto the same wavelength grid. The legend indicates the order these steps were performed in.

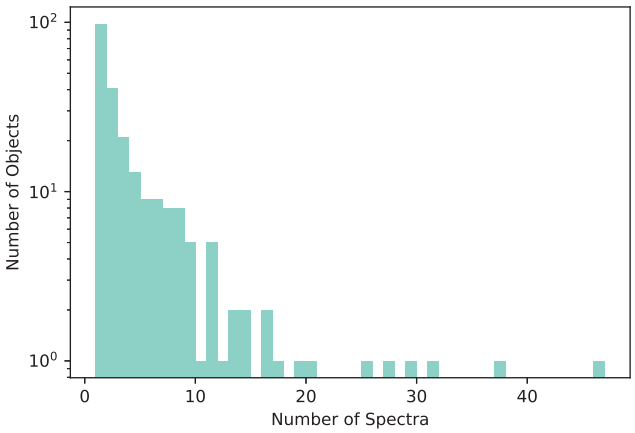

Figure 3. The total number of spectra per event in this sample. This is calculated after processing the spectra and co-adding spectra taken on the same night using the same instrument and grisms.

This final version of the spectra will be available in the data release on the SLSNe repository.[7]

For the spectra used in further analysis in this paper, post-processing was applied to remove unwanted artefacts. The spectra were all smoothed using a Savitzky–Golay filter (Savitzky & Golay 1964) with a filter window of 19, and polynomial order of 2 to reduce noise. Spectra that contained any flux between 3000 and 9000 Å were remapped onto a constant wavelength grid running between these wavelengths in 10 Å intervals to create a uniform data set. Spectra that did not cover this entire wavelength range were padded with NaN values. Lastly, all spectra were normalized to their median value. An example of this post-processing is shown in Fig. 2, where these steps are applied to a spectrum of PTF12dam.

Host galaxy lines were removed by fitting a Gaussian around the central wavelengths of prominent host galaxy lines within a 50 Å window and with a 20 Å leeway in central wavelength. These lines were identified by having narrow widths ($\lesssim 200\,\mathrm{km\,s^{-1}}$)and, in the case of hydrogen, by exhibiting similar line widths to other host lines in the spectrum. The lines used were [O II] λλ3726, 3728, H I λ3835, H I λ3889, H I λ3969, Hδ λ4101, Hγ λ4340, [O III] λ4363, Hβ λ4861, [O III] λ4959, [O III] λ5007, He I λ5876, Hα λ6563, [S II] λ6716, and [S II] λ6731. In most cases, [N II] λ6548 and λ6583 were blended with Hα. These Gaussians were then subtracted off from the target spectra. A further check was made by choosing a 20 Å buffer on either side of a 40 Å region centred on each line. The median and standard deviation (σ) was calculated in this buffer region. The central region was then checked and any flux that was more than 1σ above or below the median of the buffer region was clipped. Finally, some prominent noise spikes remained in the data. These were removed by clipping any flux above 10 times the median, or below −5 times the median. This process also accounted for any residuals from imperfect single-Gaussian fits to the Hα + [N II] blends. Further telluric removal was applied to a small subset of spectra after smoothing and rebinning where the original removal was unsuccessful, these are denoted in Appendix A.

There were 101 spectra with either noisy edges or chip gaps that could not be removed. In these cases, these wavelength regions were clipped to eliminate as much noise as possible. Noisy spectra with no discernable SN flux were omitted from further analysis and are denoted in Table A.1.

We label each spectrum with an observed phase, the number of rest-frame days from maximum light in the r band, at which the spectrum was obtained. The time of maximum is taken from Gomez et al. (2024). Because SLSNe evolve over very different time-scales, with different rise times, this observation time may not be the most physically-motivated label. We therefore also define a 'scaled phase from explosion', where the explosion time is measured by fitting a magnetar plus radioactive decay model to the light curves in Gomez et al. (2024). This was done by normalizing the phases to the decay time (τ_e), defined as the time taken to reach 1/e times the maximum bolometric luminosity, and scaling up by the median value of $\tau_e = 44$ d for the entire sample determined in Gomez et al. (2024). For the phases from explosion, this resulted in the phase range extending up to 500 scaled days. For one spectrum this resulted in a negative phase (SN 2017egm at −3.2 d before explosion). This is likely due to an uncertain explosion time due to the unusual bumpy light curve. For this spectrum, the time was instead given as time of explosion.

2.3 Sample properties

Fig. 3 shows the distribution of the number of events versus the number of spectra after processing. There are 98 objects in this sample with only a single spectrum, typically the publicly uploaded classification spectrum. This does not rule out the possibility that there exists further follow-up for these objects.

Fig. 4 shows the redshift distribution of all of the events in our sample, and also all the events with at least three spectra, in bins of $\Delta z = 0.1$. At higher redshifts there is a dearth of events with multiple spectra, likely owing to the dimmer apparent magnitude and therefore difficulty obtaining spectra over a longer time frame. This is especially apparent between redshifts of $z = 1 - 1.8$. Performing a two-sample Kolmogorov–Smirnov (KS) test on the two samples, we find a p-value of 0.03, indicating the samples are not drawn from the same distribution and the lack of multiple spectra affects the objects at higher redshifts disproportionately. However, as these spectra are collated from both public and private data, this may have introduced biases into the sample. It is also important to note that events at higher redshifts will only contribute to the bluer part of the

[7] https://github.com/gmzsebastian/SLSNe

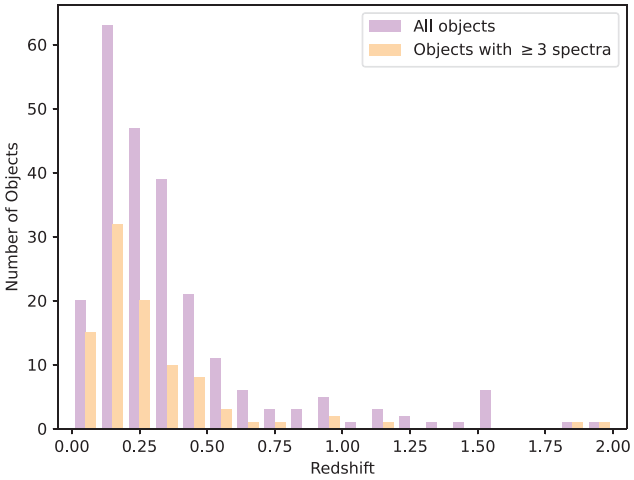

Figure 4. Distribution of redshifts of objects in this sample in bins of 0.1. In purple are all objects within this sample, and orange are objects with at least three spectra.

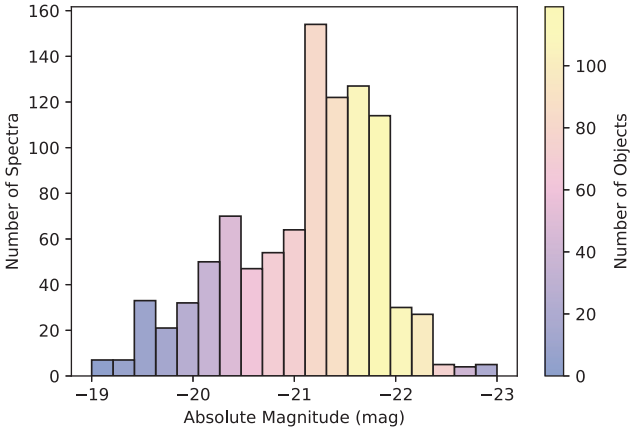

Figure 5. Absolute magnitude distribution. Absolute magnitudes are in the r band and determined based on the model fits from Gomez et al. (2024).

wavelength range once shifted to the rest frame. This is dealt with in further analysis by imposing minimum wavelength ranges for the data to be included in the analysis.

Fig. 5 shows the distribution of absolute magnitude (M) of the spectra within this sample, with the colourbar representing the number of objects in each bin. The numbers of total spectra and observed objects both peak between $M \approx -21$ to -22 mag. This is likely due to the historical cut off for SLSNe at $M \leq -21$ leading to more targeted follow-up for objects brighter than this value. However, both the numbers of spectra and objects also drop off above $M \sim -22$ mag. It is harder to imagine a selection effect that would cause this, so it may indicate an upper bound to the underlying luminosity distribution.

The distribution in Fig. 3 shows a long tail above 20 spectra per object. These are typically the most nearby events: the eight events within this tail have an average redshift of $\bar{z}_{\rm tail} = 0.08$, much lower than the overall average of $\bar{z}_{\rm all} = 0.23$. The events with the most spectra, SN 2018hti and SN 2017egm, have 50 and 51 spectra, respectively. These events had peak observed magnitudes of $m_{\rm V} = 14.74(\pm0.06)$ and $m_{\rm r} = 15.26(\pm0.01)$, at redshifts of $z = 0.0612$ and $z = 0.0307$ (Nicholl et al. 2017b; Lin et al. 2020). The event with the lowest redshift, SN 2018bsz, had a redshift of $z = 0.0267$

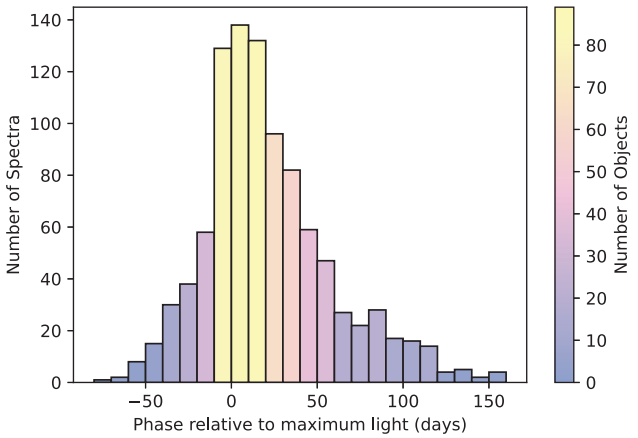

Figure 6. Phases of spectra within this sample relative to maximum light in rest frame. Colourmap indicates the number of objects within each bin.

(Anderson et al. 2018), but a comparable observed peak magnitude to these other two events. SN 2018bsz has 23 spectra within this sample.

Fig. 6 shows the distribution of phases relative to maximum light of all of the spectra within this sample. The colourmap indicates the number of objects that fall into each 10 d bin. As expected the majority of spectra are taken soon after peak where the SN is the brightest.

3 AVERAGE SPECTRA

To investigate the typical behaviour of SLSNe as a function of time, we constructed average spectra in different time bins. This was also done so features that may be faint in some spectra could become more evident in the averages. Similar techniques have been applied to other astrophysical transients such as SNe Ic, GRB afterglows and quasars (e.g. Christensen et al. 2011; Modjaz et al. 2016; Selsing et al. 2016). The evolution of the average spectra in this analysis was examined using both the phases from peak and the scaled phases from explosion. Bin sizes were chosen by starting at the earliest phase, and incrementing the sizes by 10 d until a minimum of 20 objects were included, with a minimum bin size of 20 d. These average spectra will be included in this data release.

3.1 Method of averaging

The average spectra were created by taking the smoothed and remapped spectra described in Section 2.2. Each spectrum was first normalized by its mean value to 1. Then, for each wavelength point, the median flux across all spectra was calculated. In order to not bias bins with multiple spectra from the same objects, this process was first applied to each object to create a single median spectrum per object per bin, which were then used to compute the overall statistics for that time bin.

The average spectra created are displayed in Fig. 7 for phases from peak, and in Fig. 8 for scaled phases from explosion as described in Section 2.2. The 1σ uncertainty is measured by calculating the standard deviation of the flux measurements at each wavelength. Each panel has been fit with a single blackbody, the temperature of which is indicated in the legend. This is a very good approximation at early times where the equivalent widths of absorption/emission lines are weak compared to the flux from the blackbody. At these earliest epochs, the blackbody temperature is ∼10 000 K. However, SLSNe

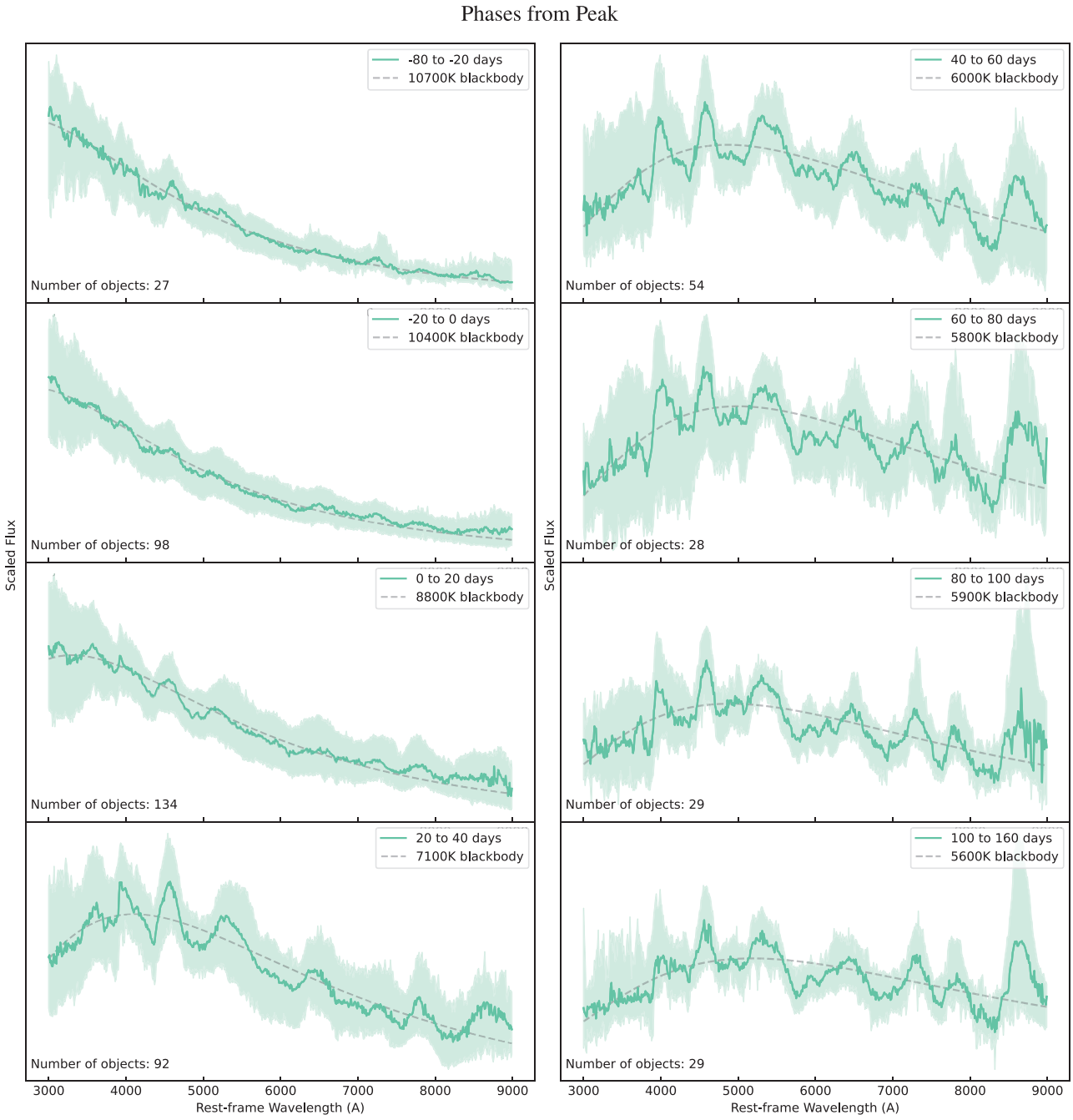

Figure 7. Composite average spectra in time bins relative to maximum light. The light green shaded region denotes the 1σ uncertainty. Number of objects contained in each bin are tagged, with a minimum of 20 events imposed per bin. Best-fitting blackbody is indicated in grey dashed lines.

are often described using a modified blackbody, where the flux below a cut-off wavelength has a linear suppression applied to it (Nicholl et al. 2017c; Yan et al. 2018). This is due to the significant absorption in the UV from lines such as C II λλ2325, 2328, Si III λ2543, and Mg II λ2800 (Chomiuk et al. 2011; Quimby et al. 2011; Howell et al. 2013; Vreeswijk et al. 2014). In SLSNe, this cut-off wavelength has been found to be $\lambda = 3400^{+1000}_{-700}$ Å (Gomez et al. 2024). However, our spectral analysis does not extend beyond 3000 Å into the UV and so we cannot comment on any trends regarding the use of a modified blackbody.

Over the next few months, the spectra begin to transition to more emission lines, and the underlying blackbody temperature decreases to 7000−8000 K. We can see the blackbody still captures the general shape of the spectral energy distribution (SED) very well. Popular light-curve fitting codes for SLSNe such as MOSFiT and REDBACK assume that at optical wavelengths ($\gtrsim$ 3000 Å) the SED can we well represented by a blackbody (Nicholl et al. 2017b; Sarin et al. 2024). Our analysis suggests that this is a reasonable assumption.

MOSFiT and REDBACK also introduce an additional free parameter to fit of the final plateau temperature ($T_{\rm min}$) in their magnetar models. This parameter is important for extending these fits to late times and simply introduces a minimum temperature to which the fits converge. In MOSFiT, the default prior for this parameter is a Gaussian with a mean of 6000 K and a standard deviation

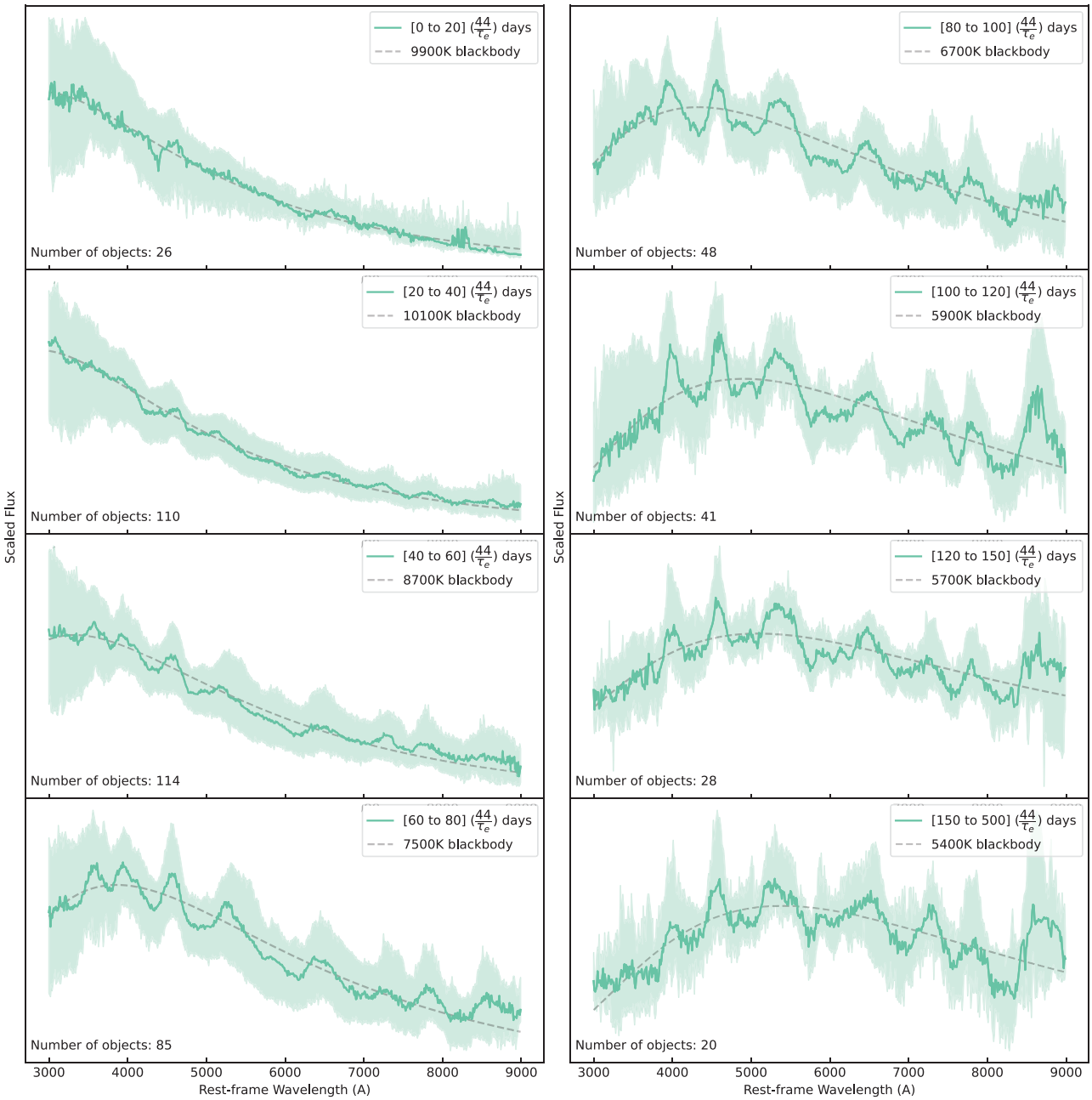

Figure 8. Composite average spectra in time bins relative to explosion, and scaled. The light green shaded region denotes the 1σ uncertainty. Number of objects contained in each bin are tagged, with a minimum of 20 events imposed per bin. Best fit blackbody are indicated in grey dashed lines.

of 1000 K, whereas in REDBACK the default is a uniform prior between 3000−10 000 K. Applying `MOSFiT` to a sample of 238 SLSNe, Gomez et al. (2024) obtain a value of $T_{\rm min} = 6500^{+1700}_{-1400}$ K. This is consistent with previous work by Nicholl et al. (2017b), who used a sample of 38 SLSNe and obtained an average of ∼6400 K. We can see the blackbody temperature in both Figs 7 and 8 plateauing to about 5000–6000 K that supports the use of $T_{\rm min}$ in the fitting.

We can also compare the average temperature evolution derived from the spectra to the temperature derived from fitting `MOSFiT` models to the light curves. This is shown in Fig. 9 which displays the mean, 1σ, 2σ, and 3σ ranges for the population. The temperatures derived from the spectra fall within the 2σ spread and are therefore consistent with those obtained from photometry. However, they are systematically lower, which may be attributed to our spectra not extending as far into the UV as the photometry. This sample is limited to 3000−9000 Å in the rest frame (the range covered by the vast majority of spectra). This restriction likely prevents us from capturing the peak of the blackbody fits, particularly at early times.

3.2 Time from peak versus time from explosion

Looking at the evolution of the spectra in Figs 7 and 8, we can see the earliest two bins corresponding to the time before maximum light

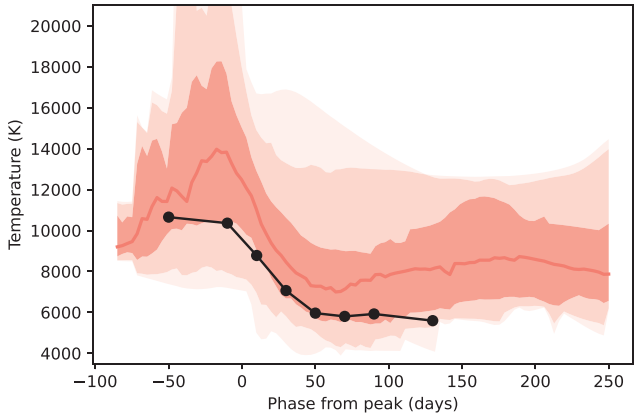

Figure 9. The temperature evolution of average spectra from Fig. 7. These are grouped in phase from peak and plotted in black. In comparison, the temperature evolution derived from the photometry in Gomez et al. (2024) is plotted in red. The shades of red denote the 1, 2, and 3σ ranges. The spectroscopic temperatures fall within the 2σ spread of photometric values but are systematically lower, likely due to the spectral coverage not extending as far into the UV.

show high and roughly constant temperatures, between 10 000 and 11 000 K. At these phases we see a hot blue continuum with weak absorption lines in comparison. The next three bins show a fairly rapid change in properties, with the emergence of stronger P-Cygni and potentially emission lines which will be discussed further in Section 3.3. This is accompanied by a drop to ∼6000 K. The final three bins then show a very slow evolution, with the continuum emission decreasing in strength relative to the lines, but no evidence for further cooling. We note that we see very similar behaviour using both binning schemes.

We investigated whether the behaviour of SLSNe is more homogeneous when grouped by phase from peak (convenient observationally), or scaled phase from explosion (perhaps better motivated physically). The fits from these methods were quantified by calculating the relative scatter (standard deviation, σ_F, divided by the median flux, $F_{\rm med}$) in each group, averaged over wavelength. Averaging over the eight time bins in each binning scheme, we find only a marginal change in the scatter using the two methods. The averages using phases from peak showed $\langle \sigma_{F,\rm peak}/F_{\rm med,peak}\rangle = 0.66$, whereas using the scaled phases from explosion showed $\langle \sigma_{F,\rm exp}/F_{\rm med,exp}\rangle = 0.64$. This quantifies the visual observation that both Figs 7 and 8, and therefore both methods of averaging produce reasonable results. However, the averages obtained when binning in scaled phases from explosion exhibit slightly tighter fits, but only marginally.

As the fractional standard deviations were so close, we cannot say for certain if either binning scheme provides a more homogenous grouping. The reason for this may be that SLSNe seem to show a constant temperature and very little spectral evolution up to maximum light. After this, the spectra only evolve significantly during the rapid photospheric cooling phase, usually immediately after peak. Since we scale the explosion phases based on the light-curve evolution rate, so that all scaled spectral series effectively peak in the same bin, this largely erases any differences in temperature in the bins between measuring from peak or measuring from explosion. This is also apparent in the blackbody fits, which are very similar for the two binning schemes. Physically, this suggests that a characteristic temperature evolution drives the spectral evolution we see in SLSNe.

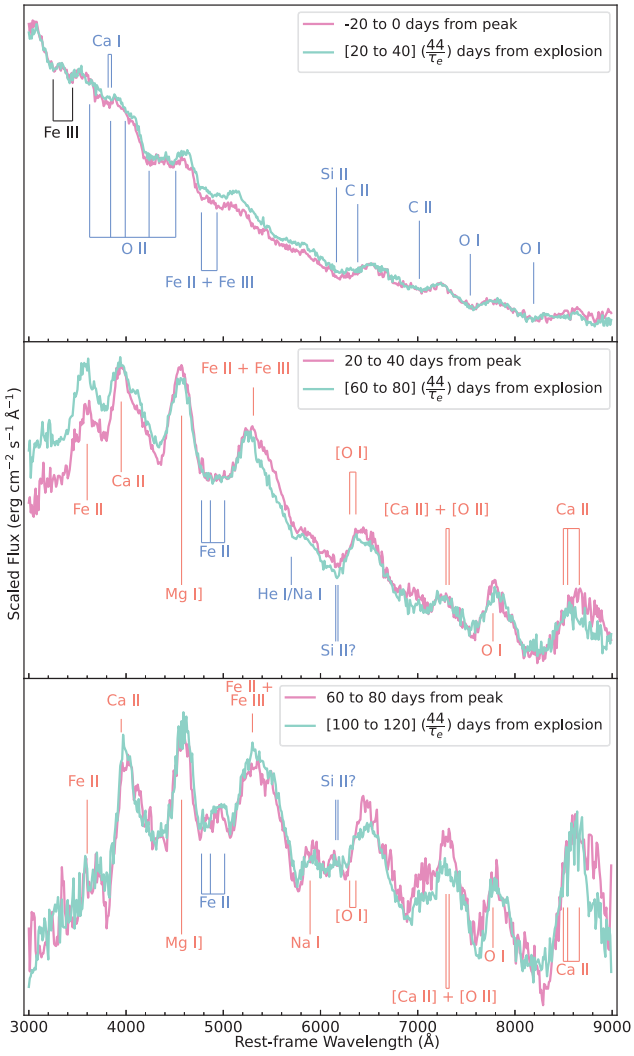

Figure 10. Subset of average spectra. Plotted both in days from peak, as well as scaled days from explosion to match the median e-folding decline time of SLSNe (44 d). τ_e refers to the time taken for the light curve to reach 1/e times the maximum luminosity. Blue labels indicate absorption lines which have all been shifted by 9000 km s^{-1}. Red labels are for emission lines which are shown at rest.

3.3 Line identifications

Fig. 10 shows a subset of the average spectra at representative epochs. Averages from both explosion and peak are plotted together in corresponding bins from each, with both having the same bin sizes. As discussed in Section 3.2, both methods result in a similar spectral evolution, and therefore it is not surprising to see that the corresponding bins look similar. There are only minor discrepancies in the shape of the continua and line strengths but these fall into the 1σ uncertainties (not plotted in this figure for visibility). All absorption lines are labelled in blue and have been blueshifted by ∼9000 km s^{-1} to match the observed troughs of features. Emission lines are labelled in red and are plotted at rest.

The top panel shows the spectra between −20 and 0 d relative to peak, and 20–40 scaled days from explosion. The blackbody temperature is about 10 000 K. We note that although we can see the series of characteristic O II absorption lines, these spectra do not show a strong 'W' shape. Instead this shape appears to be more of a broad trough due to dilution when averaging over spectra with a

range of velocities. The effective wavelengths of these O II blends are 4650.71 Å, 4357.97 Å, 4115.17 Å, 3959.83 Å, and 3737.59 Å (Quimby et al. 2018). At redder wavelengths, we see lines from Si II λ6355, C II λ6580, C II λ7234, and O I λ7774 and O I λ8446. There are also potential Fe III lines at around 3200 Å (Leloudas et al. 2012; Nicholl et al. 2013). This is supported by spectral models created by Dessart (2019) around peak, where Fe III is the only ion to show significant features in the form of P-Cygni lines.

Looking at Figs 7 and 8, at the very early spectra from −80 d before peak, and 20 scaled days from explosion, we can see a small bump indicating excess flux around ∼7300 Å. This is coincident with a known nebular line due to emission from forbidden lines of [Ca II] and [O II]. This shows early emission of nebular lines may be more prevalent than previously thought. Only a handful of SLSNe have shown this line before or at peak, including SN 2019szu (Aamer et al. 2024) and SN 2018ibb (Schulze et al. 2024). Some normal SNe Ic have also shown early appearances of this line. This includes SN 2022xxf, an unusual event with a double peaked light curve and appearance of forbidden lines before the second peak Kuncarayakti et al. (2023). There does not seem to be any evidence at these phases for [O III] λλ4959, 5007, which could imply that in the majority of these events the early emission is dominated by calcium. This does not rule out the excess flux being attributed to [O II] λλ7320,7330 as this line is expected to be stronger than both [O III] lines based on models due to the higher temperatures required for [O III] (Jerkstrand et al. 2017; Omand & Jerkstrand 2023). In the case of SN 2019szu, the identification of [O II] at peak is secure (Aamer et al. 2024). We therefore performed a visual search through all objects for other events that show evidence of other [O II] and [O III] lines, which would suggest that [O II] dominates the early emission at 7300 Å. We find one additional case similar to SN 2019szu, SN 2022le which also displays strong forbidden lines of oxygen at early phases. This object will be the subject of a future paper (Blanchard et al. in preparation).

The middle panel shows the spectra between 20 and 40 d relative to peak, and 60 to 80 scaled days from explosion. The blackbody temperature is about 7000 K at these phases. By this stage the hot blue continuum has decreased and the line profiles are mostly P-Cygni shaped. These include a blend of Fe II at ∼3600 Å and ∼5300 Å, Ca II λλ3934, 3968, [Ca II] λλ7291, 7323, and [O II] λλ7320, 7330. Some of the lines look more symmetrical and therefore may consist of pure emission such as Mg I] λ4571, and O I λ7774. The feature around 6000–6500 Å is difficult to identify, with a complex profile and an emission peak wavelength that does not match any common line. We suggest this could be caused by [O I] λλ6300, 6364 in emission combined with Si II λλ6347, 6371 in absorption. It is interesting to note the appearance of more forbidden and semi-forbidden transitions which require lower density material in order to form. At this stage in the evolution, the spectral lines look very similar to those of typical SNe Ic. The one exception to this is the region around 5700–6500 Å, where SNe Ic often do not display the same multipeaked profiles in the complex of lines as seen in SLSNe (Nicholl et al. 2016a). However, it is difficult to reconcile the hotter underlying continua for SLSNe, compared to the cooler temperature of the line forming region if the SN ejecta is in radiative equilibrium. Chen et al. (2017) explain this by the presence of porous or clumpy, H- and He-poor material, which the ejecta can interact with and introduces an additional hot black-body component to the flux. Alternatively, the ejecta can become clumped due to engine-driven turbulence, leaving low-density regions capable of producing the emission lines and dense regions that provide the continuum (Chen, Woosley & Whalen 2020).

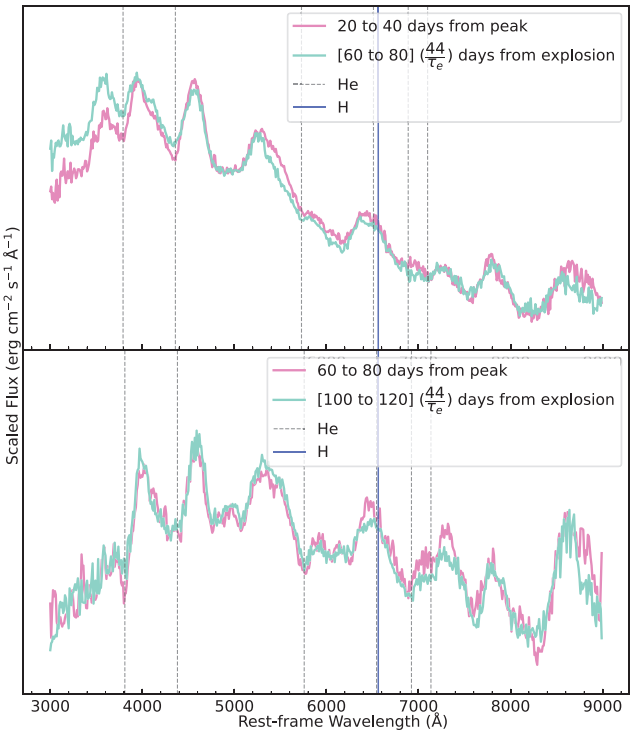

Figure 11. Subset of average spectra. Plotted both in days from peak, as well as scaled days from explosion to match the median e-folding decline time of SLSNe (44 d). Dashed vertical lines indicate He absorption lines which have been blueshifted by 7500 km s^{-1} in the top panel, and by 6000 km s^{-1} in the bottom panel in order to match observed troughs in the spectra. The solid blue line corresponds to rest-frame H α.

The final panel in Fig. 10 presents the spectra from 60 to 80 d relative to peak and 100 to 120 scaled days from explosion. While many of the same lines visible in the middle panel remain, the profiles have transitioned from P-Cygni-like features to being more emission dominated. Additionally, the underlying blackbody continuum has cooled significantly to approximately 6000 K. In this phase, we observe the emergence of the Na I λλ5890, 5896 doublet and a more pronounced Fe II absorption feature. A prominent feature appears around 7100 Å in the averages relative to peak, though it remains unidentified and is not labelled in this panel. The profile shape could be a result of absorption from He (see the next section). Notably, the Fe II emission near 3800 Å is weaker compared to the previous panel.

3.4 Degree of envelope stripping

The post-maximum spectra exhibit a weak absorption feature around 5700 Å which could be attributed to either He I λ5876 or Na I λλ5890, 5896, both of which would need to be blueshifted by ∼9000 km s^{-1}. A He-rich sub-class of SLSNe has been proposed by Yan et al. (2020). To investigate whether this feature is indeed due to helium, we searched for evidence of other He lines in the average spectra. This is illustrated in Fig. 11, where prominent He lines at 3888 Å, 4471 Å, 5876 Å, 6678 Å, 7065 Å, and 7281 Å are plotted for the bottom two panels of Fig. 10. By blueshifting the lines in the top panel by approximately 7500 km s^{-1}, we observe that several lines align with troughs in the spectra. Notably, the 7065 Å and 7281 Å

lines match up to small dips in the spectra that are not attributed to other features. This trend continues in the bottom panel with the lines blueshifted by ∼6000 km s^{-1}. Determining with certainty whether all these lines are present is difficult, particularly since the 3888 Å and 4471 Å lines coincide with troughs caused by other emission lines, and the 6678 Å line overlaps with an emission peak. However, it could be argued that a slight dip is visible at the location of the 6678 Å line, which is especially noticeable in the spectra grouped by phase from peak. This shows creating average spectra helps identify features which may not be obvious in individual spectra, but are strengthened by combining them. The possible presence of He in the averages suggests that many SLSNe may retain some residual He at the time of explosion.

Checks were also performed to look for signatures of H and C; however, we did not find evidence for these elements in the averages. Rest-frame H α is plotted in Fig. 11 with a solid blue line. The lack of H is to be expected as this sample looks at Type I SLSNe which are inherently H poor. There have been some events with evidence for H at late times, in the form of emission lines from late-onset interaction with CSM (Yan et al. 2015, 2017b); however, we do not find strong indicators for this in our sample showing this is not ubiquitous in the population. The lack of C shows the presence of this may also be a unique and rare feature (e.g. Anderson et al. 2018; Gutiérrez et al. 2022; Gkini et al. 2024).

4 PRINCIPAL COMPONENT ANALYSIS

In Section 3, we investigated the evolution for 'representative' SLSNe and searched for similarities between the population as a whole. Now, we will investigate the diversity of the population and which spectral features account for this.

Principal Component Analysis (PCA) is a technique used to reduce the dimensionality of a data set, while retaining its key information. This decomposition creates a set of principal components, from which all the spectra in that set can be recreated. The first principal component explains the most variance, and each subsequent one explains the next largest portion of variation, with the key requirement that each new component is uncorrelated with the ones before it. The resulting set of principal components form an orthogonal basis in the space of the data (Pearson 1901; Hotelling 1933). Spectral data often contains a lot of redundant information because flux from nearby wavelengths tend to be highly correlated. PCA can summarize the data by identifying a few key components that describe most of the variability in the sample. These components can then be used to group samples, identify outliers, or understand underlying patterns in the data. This is a technique that has been applied to large data sets of SN spectra (e.g. Williamson, Modjaz & Bianco 2019; Nicholl et al. 2019b).

The data in this sample was split by phase into four bins. Using the same bin sizes as in Section 3 would result in too few spectra per time bin and so new boundaries were chosen. Each bin was chosen to contain roughly 150 objects. We note that we see little evolution over the phase ranges included in these broader bins. Spectra that did not cover at least 60 per cent of the wavelength range between 3000 and 9000 Å were not included in this analysis. Cuts were also applied to objects that were too noisy to contribute meaningfully to the analysis. The breakdown of these bins is given in Tables 2 and 3. The data was also standardized by normalizing to the median. This was to ensure all spectra were contributing equally to the analysis.

Table 2. Bin sizes used for the PCA analysis using phases from peak, the number of spectra in each bin after removing noisy spectra, and the number of components needed to explain 85 per cent of the variation in the sample.

Phases from peak (d)	Spectra	Objects	Components
−80–−5	154	56	5
−5–15	168	103	5
15–40	155	84	8
40–160	185	70	8

Table 3. Bin sizes used for the PCA analysis using scaled phases from explosion, the number of spectra in each bin after removing noisy spectra, and the number of components needed to explain 85 per cent of the variation in the sample.

Scaled phases from explosion (d)	Spectra	Objects	Components
0–35	160	71	5
35–55	154	red92	4
55–80	162	red85	5
80–500	186	red65	8

4.1 Component spectra

Figs 12 and 13 show the component spectra from the PCA decomposition for phases from peak, and scaled phases from explosion, respectively. The columns on the right indicate the percentage that each component contributes to the total variation, and the cumulative total when adding these components sequentially. These components form the basis of the set from which all spectra in the sample can be created. A threshold of 85 per cent was used, meaning only components that can explain up to 85 per cent of the total variation are included. This threshold was chosen to maximize the level of variation explained by the components while reducing the level of noise in the components. Using a higher threshold included components that explained less than 1 per cent of the variation and were constituted of primarily noise. We can see that as the phase increases, the number of components needed to explain the same amount of variation in the data increases. This means the spectra at early times tend to be more similar to one another than at late times. This can be seen in both Figs 12 and 13 and has been summarized in Tables 2 and 3. Although this increase in components in the final bin could be due to a much broader bin width, we showed in Section 3 that the spectra do not evolve very much over this period. We can also see in Tables 2 and 3 that these final bins also contain the fewest number of unique objects meaning the diversity must be inherent to the phase.

In Figs 12(a) and 13(a), we see that only five components are needed to explain 85 per cent of the variation within the sample. The first couple of components in both Figs 12(a) and 13(a) show different continuum shapes implying the majority of the variation at early times is due to the underlying blackbody temperature. This implies at early times the spectra are relatively simple, likely due to the flux being dominated by the blackbody continuum and the lines being comparatively weak.

The final component in Figs 12(a) and 13(a) show the characteristic O II 'W'-shape just below 4500 Å meaning there is significant variation in these lines at these early phases. This feature is also clearly visible in Fig. 12(b), in contrast to Fig. 13(b), which only marginally shows variation at the location of this feature. Sample studies of SLSNe by Könyves-Tóth (2022) have suggested separate sub-classes of SLSNe where the O II absorption lines at peak either display

a strong 'W'-shape, or a '15bn'-like shape with no discernable double trough. Here we see that if we remove the dependence on observing relative to peak, the diversity in O II lines decreases, indicating that the separate sub-classes may just be a reflection of the different times the objects are observed relative to explosion. Quimby et al. (2018) suggested a similar spectroscopic division into '2011ke'-like or 'PTF12dam'-like events. Spectra were assigned a spectral phase ϕ which ranged from $\phi = -1$ for early-phase spectra with strong O II lines, $\phi = 0$ when the O II lines disappeared, and $\phi = 1$ when the spectra resembled SNe Ic near maximum light. Spectra grouped into the '2011ke'-like category exhibited broader absorption features between $-0.3 < \phi < 0.3$, suggesting high ejecta velocities.

The middle panels of Figs 12 and 13 correspond to the rapid cooling stages seen in Section 3. Here, many more components are required to explain the same level of variation, especially when grouping the spectra by phases from peak. This is especially apparent in Fig. 12(c) that corresponds to the latter stages of this cooling period and requires eight components to reach the threshold. This suggests that at least some of the diversity in SLSN spectra results from comparing objects evolving with different time-scales. By contrast, Fig. 13(c) only requires five components, which is the largest discrepancy we find in terms of numbers of components needed for corresponding bins. This may indicate that grouping spectra by scaled phases from explosion could group together more similar spectra, offering a more effective way of describing the spectral evolution of SLSNe.

The middle panels of Figs 12 and 13 begin to show more individual lines and the differences in these line strengths. There appears to be a line at 7300 Å in the final components of Fig. 12 a which persists at later epochs. This is coincident with a forbidden emission line either from [Ca II] or [O II]. This line also shows up in the average spectra created in Section 3 as early as −80 d before peak, and can be seen in the 1σ spread. Early appearance of this line (such as at the phases in Fig. 12b) has been linked to interaction with low-density CSM which, as discussed, may be a sign of PPI in SLSNe. By contrast, the panels in Fig. 13 do not show as clear variation at the location of the feature until 55 d post-explosion (Fig. 13c). This reinforces the idea that these lines are formed outside the SN ejecta, as it takes time for the ejecta to reach these line forming regions and interact with them.

The last set of panels show the spectra once they have started transitioning to the pseudo-nebular phase, but still with an underlying blackbody component. We once again see the most variation explained by the underlying continuum. These panels correspond to the plateau in temperature seen in Section 3. We can see that at these later times as the SLSNe are evolving more slowly, the diversity is less dependent on binning scheme and therefore the number of components is the same regardless of whether we normalize the time-scales. This is because the evolution time-scale at this phase is much longer and is therefore less sensitive to the bin edges. We also begin to see the emergence of different lines to explain the variation. At these stages, more of the diversity is attributable to the strengths of identifiable emission lines. These include Fe II at ∼3500 Å, Ca II λλ3934, 3968, Mg I] 4571, Fe II at around 5100 Å [O I] λλ6300, 6364, [Ca II] λλ7291, 7323, [O II] λλ7320, 7330, and Ca II λλλ8498, 8542, 8662. Once the spectra fully evolve into the nebular phase, the diversity can largely be explained by a few strong emission lines (Nicholl et al. 2019a). However, we caveat this with the fact that at these later phases, the SLSNe are much fainter and noise plays a significant role in the variation seen.

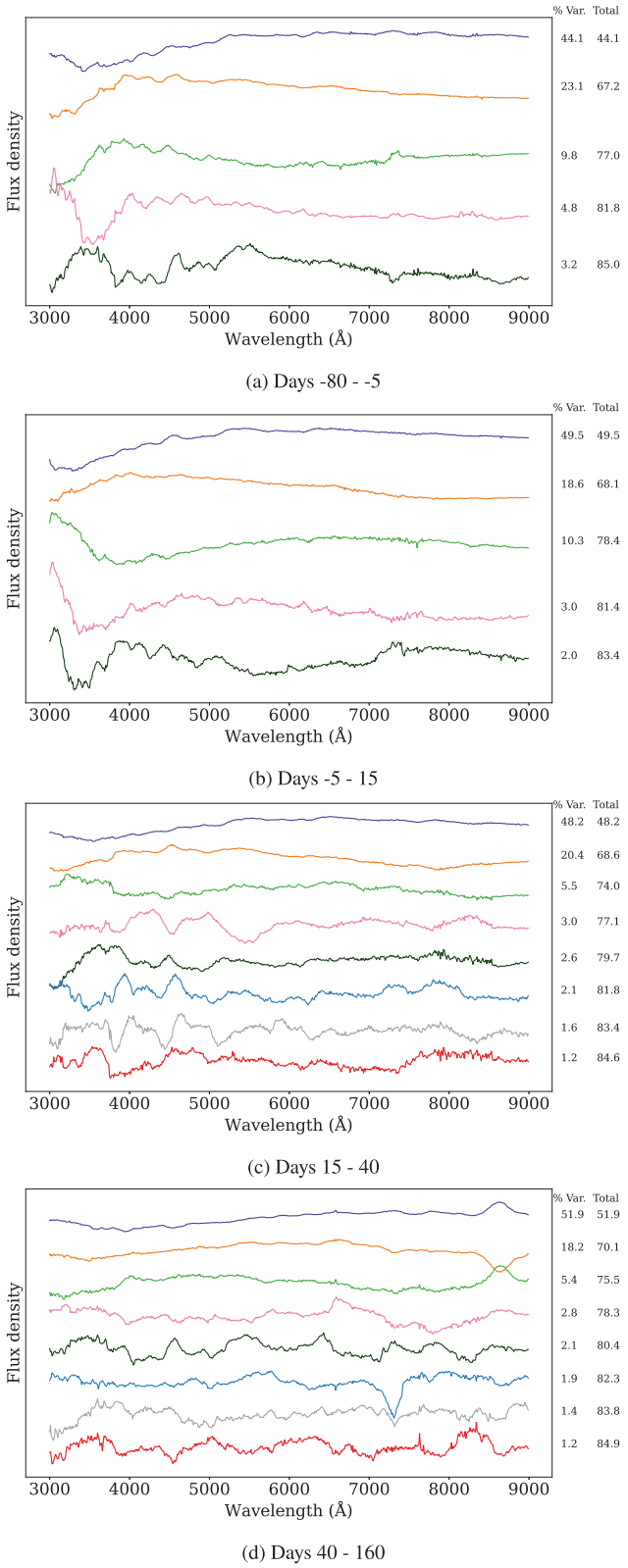

Figure 12. PCA decomposition of SLSN spectra in different time bins relative to peak. Explaining variations up to 85 per cent of the sample. The Var column indicates the percentage variation explained by each component, and the Total percentage column shows the cumulative percentage explained by the addition of each new component. More components are needed at later times meaning greater variation in the spectra at late times.

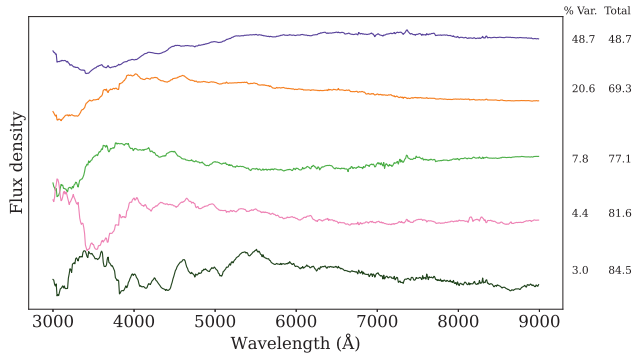

(a) Days 0 - 35

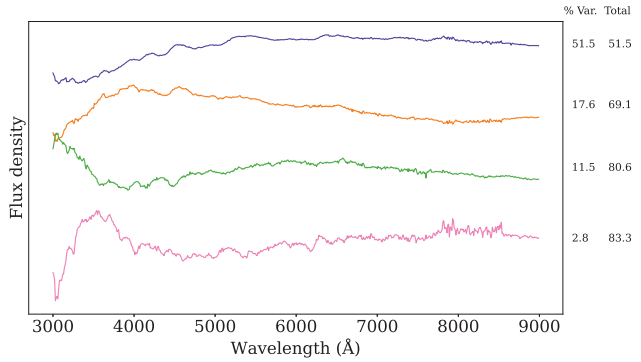

(b) Days 35 - 55

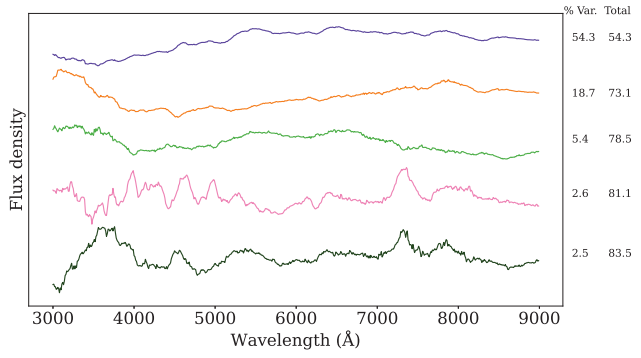

(c) Days 55 - 85

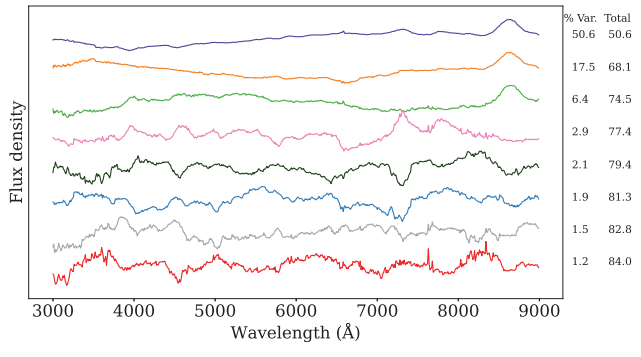

(d) Days 80 - 500

Figure 13. PCA decomposition of SLSN spectra in different time bins relative to explosion, with the phase scaled to match the median e-folding decline time of SLSNe (44 d). Explaining variations up to 85 per cent of the sample. The Var column indicates the percentage variation explained by each component, and the Total percentage column shows the cumulative percentage explained by the addition of each new component. More components are needed at later times meaning greater variation in the spectra at late times.

4.2 Clustering

In order to search for subpopulations, K-means clustering (Lloyd 1982) was used on the first two PCA components of each phase bin. This is an unsupervised learning algorithm that separates the data based on the distance of each point from its centroid. In K-means clustering, the number of clusters must be specified in advance. The algorithm then iteratively assigns each data point to the nearest centroid and updates the centroids until the assignments stabilize, resulting in clusters that minimize within-cluster distances. To visualize this, 'silhouette plots' were created, which evaluate the quality of clustering results by assessing how well the data points fit within their assigned cluster. The silhouette coefficient, a key metric displayed in these plots, measures how close a point is to the centroid of its own cluster compared to the centroid of the nearest neighbouring cluster. This coefficient ranges from -1 to 1, where values close to 1 indicate that the point is well separated from other clusters and strongly belongs to its assigned cluster, while values near 0 suggest the point lies near a cluster boundary. Negative values indicate potential misclassification, where the point is closer to a different cluster than its assigned one. In silhouette plots, each cluster is represented as a bar showing the distribution of silhouette coefficients for all points within the cluster, sorted in descending order. The overall clustering quality is summarized by the mean silhouette coefficient, shown as a vertical line. A mean value above 0.5 typically indicates that the clustering structure is reasonable, while values exceeding 0.7 are considered strong evidence of well-separated and cohesive clusters. Clusters with significant internal variability or many negative silhouette values may indicate overlapping cluster boundaries or misclassified points.

Silhouette plots were created for each phase bin using numbers of clusters between two to five. A representative version of these plots is shown in Fig. 14, which shows a grouping of the data into two clusters for the spectra from 0 to 35 scaled days post-explosion. We can see that although the groups are all of roughly similar size based on the thickness of each plot, and exceed the average silhouette scores, they do not exceed ∼0.5 indicating they are not very defined clusters. This is visualized in the right-hand side plots where we can see which points belong to which groups, and see the lack of distinct groups visually. For most cluster sizes and time bins, there was no evidence for clusters of any size between two and five. The only exception to this are the silhouette plots created with a cluster size of two for the 80–500 scaled days post-explosion data (Fig. 15), specifically when comparing component one against components two, three, four, and five. This second cluster is primarily composed of spectra from SN 2017egm which we show to be spectrally unique later in this section. The process was performed for all possible component combinations for the first five PCA components. Overall, this indicates there is no evidence for separate subpopulations within the spectral data when considering the five most important PCA components needed to describe the variance in each time bin.

We also searched for clusters using Bayesian information criterion (BIC; Schwarz 1978) shown in Appendix B. This method assesses the fit of using different numbers of clusters, while penalizing models with more parameters (i.e. larger numbers of clusters). This is important as using more clusters could result in over-fitting the data. These were then fit using K-means clustering for clusters of sizes one to five, shown in Appendix B. The plots show there is no evidence of separate clusters as shown by the consistent decrease in BIC values as the number of clusters increases. We would expect to observe a sharp drop at the point corresponding to the optimal

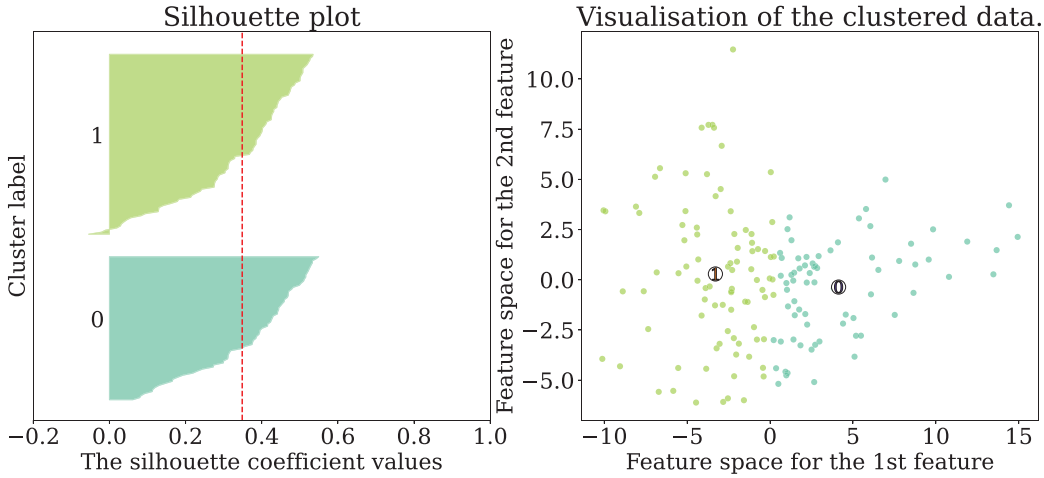

Figure 14. Silhouette plot using a cluster size of two for the first two components from the PCA decomposition in the time bin 0–35 scaled days post-explosion. These plots show the quality of clustering by displaying the silhouette coefficient for each point, which measures how well the point fits within its assigned cluster compared to the nearest neighbouring cluster. Values range from −1 to 1, with higher values indicating well-separated clusters, while negative values suggest possible misclassification. The mean silhouette score, shown as a red vertical line, summarizes clustering performance. With a score below 0.5, this suggests no evidence of clustering. The right panel displays these clusters in the PCA parameter space.

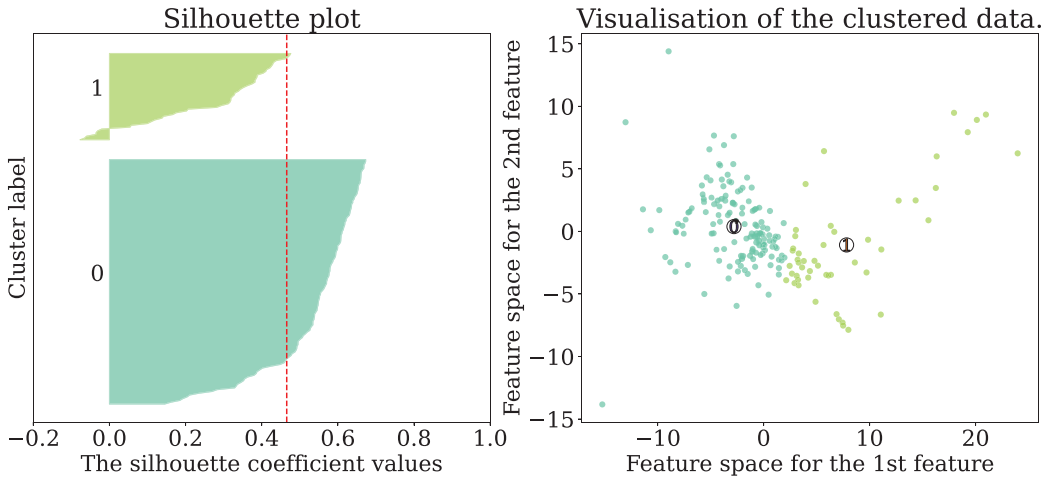

Figure 15. Silhouette plot using a cluster size of two for the first two components from the PCA decomposition in the time bin 80–500 scaled days post-explosion. These plots show the quality of clustering by displaying the silhouette coefficient for each point, which measures how well the point fits within its assigned cluster compared to the nearest neighbouring cluster. Values range from −1 to 1, with higher values indicating well-separated clusters, while negative values suggest possible misclassification. The mean silhouette score, shown as a red vertical line, summarizes clustering performance. With a score just below 0.5, this suggests a slight preference for two distinct clusters. However, the second cluster is primarily composed of spectra from SN 2017egm which we show to be spectrally unique in Section 4.2. The right panel displays these clusters in the PCA parameter space.

number of clusters if this truly represented the number needed to describe the data. This again suggests there is no statistical evidence for multiple populations within the data when accounting for the majority of the variation in the spectra.

Figs16 and 17 show the component spectra from Section 4.1 represented in PCA parameter space. This plots the PCA coefficients of some of the components against each other to see if there are any correlations between them. Each object is represented by a unique colour consistent across both figures and all panels. This analysis is also explored in Appendix C in the context of 'fast' and 'slow' evolving SLSNe. As expected from the cluster search, there do not seem to be any significant trends or groups within the data. However, there do seem to be several individual events that are outliers from the central clumps. Visual assessment of the spectra of all outliers showed that they fall into one of two categories: the spectrum is noisy but still with discernable SN flux, or the spectrum truly deviates from the average spectra calculated in Section 3. The spectra of interest are the ones that fall into this latter category and include spectra from SN 2019pud, PTF12hni, and SN 2017egm.

In the early phases of Figs 16 and 17, an outlier spectrum marked as a blue square is apparent. This corresponds to a spectrum of PTF12hni, shown in Fig. 18 at −6.54 d relative to peak, alongside the average spectrum from Section 3 in the corresponding time bin. In the bluer wavelengths, this spectrum looks more similar to the averages from later time bins such as the average from 20 to 40 d post-peak. However, the weak lines compared to the continuum emission in the redder wavelengths beyond 7000 Å looks more similar to the average from −20 to 0 d before peak. The unusual nature of this object is complicated by its discovery after its peak, meaning the time of peak is estimated either from modelling the light curve as is

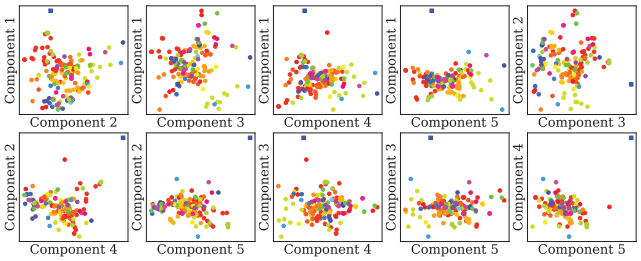

(a) Days -80 - -5

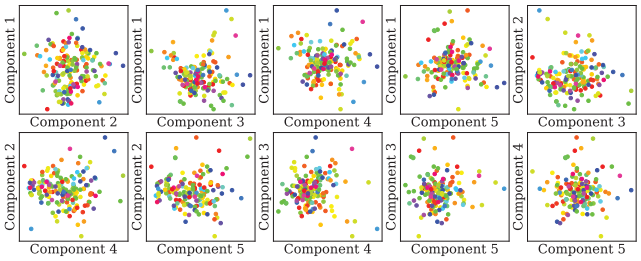

(b) Days -5 - 15

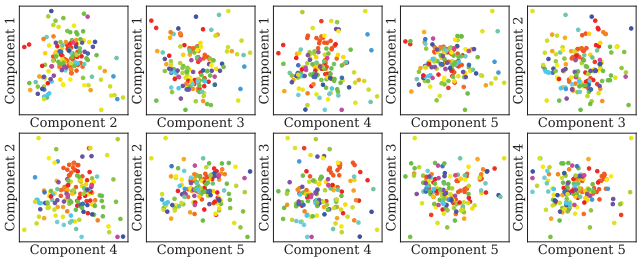

(c) Days 15 - 40

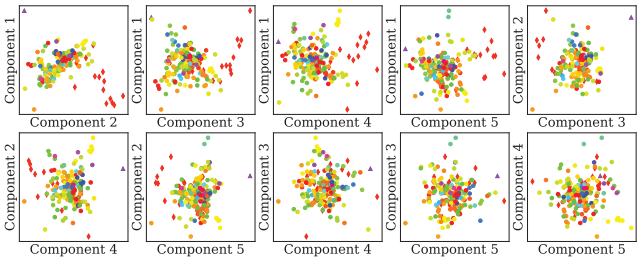

(d) Days 40 - 160

Figure 16. Representation of the SLSN photospheric spectra in the PCA parameter space in time bins relative to peak. Only the first five components for each bin are plotted for visualization. Each SLSN event is marked by a unique colour, consistent across all panels. Interesting outliers are marked by different shapes and discussed in Section 4.2.

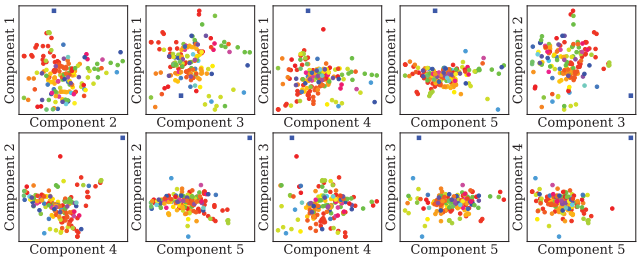

(a) Days 0 - 35

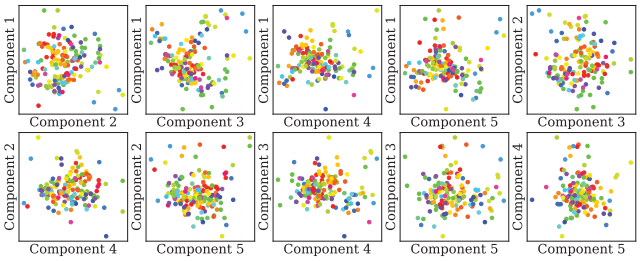

(b) Days 35 - 55

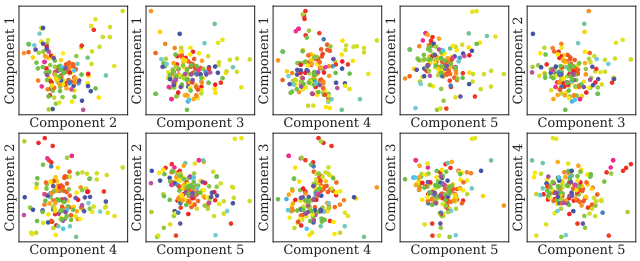

(c) Days 55 - 80

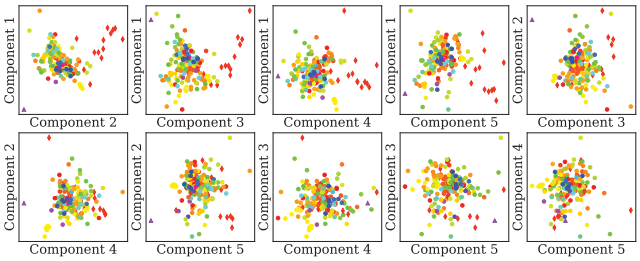

(d) Days 80 - 500

Figure 17. Representation of the SLSN photospheric spectra in the PCA parameter space in time bins relative to explosions with the phase scaled to match the median e-folding decline time of SLSNe (44 d). Only the first five components for each bin are plotted for visualization. Each SLSN event is marked by a unique colour, consistent across all panels. Interesting outliers are marked by different shapes and discussed in Section 4.2.

the case for the analysis in Gomez et al. (2024), or from template matching of the spectra as in Quimby et al. (2018). Although these methods estimate a similar time of peak, Quimby et al. (2018) also acknowledge plausible matches to SLSN templates up to 100 d post-peak. For this reason, PT12hni as an outlier in both binning schemes may simply be due to an uncertain time of explosion and time of peak.

An outlier spectrum of SN 2019pud is shown in Figs 16(d) and 17(d) as a purple triangle. This spectrum is obtained at 53.18 d post-peak is shown in Fig. 18, and compared to the average spectrum from Section 3 in the corresponding time bins. We can see that SN 2019pud looks similar to the average at bluer wavelengths except with a slightly broad emission line around 5000 Å, that is not visible in the average. However, it also does not display any emission or P-Cygni features redwards of 7000 Å. This object appears in a sample paper of H-rich SLSNe (Kangas et al. 2022), where it is also noted for its unusual features even within the class of H-rich SLSNe. The strong emission feature at ∼6500 Å peaks further to the red than the [O I] line in the average spectrum, and was attributed to Hα. However, this object did not show H emission until ∼50 d after peak and was therefore classed as a 'SLSNe I.5' by Kangas et al. (2022).

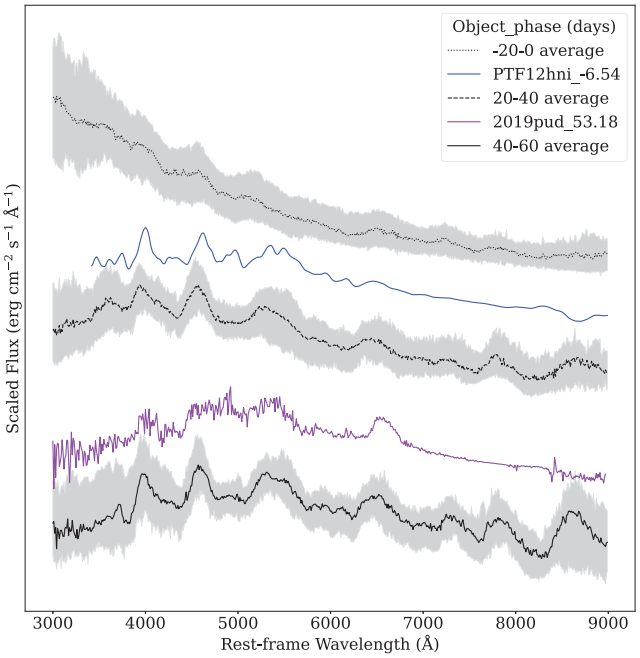

Figure 18. Spectra of PTF12hni and SN 2019pud that fall outside the central grouping in the PCA parameter space. The colours of the spectra are consistent with the colour of the outlier points in Figs 16 and 17. In black are the relevant average spectra from Fig. 7 for comparison. We can see how the spectrum of PTF12hni looks similar to spectra at much later phases. In the case of SN 2019pud, the spectrum looks different from its respective average with the presence of a strong Hα emission line, and lack of features in the red end of the spectrum. The spectrum of PTF12hni is from Quimby et al. (2018), and the spectrum of SN 2019pud is from Kangas et al. (2022).

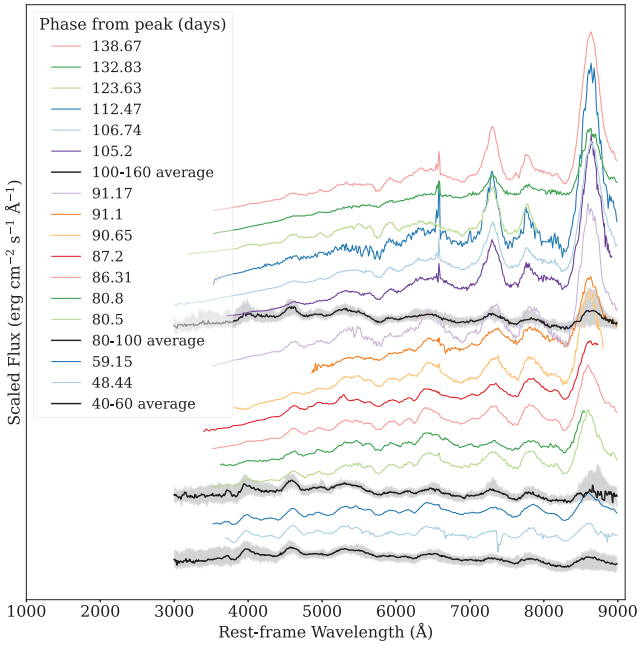

Figure 19. Spectra of SN 2017egm with phases from peak above 35 d. Inter-spaced are the average spectra from Fig. 7 for comparison. All spectra including the averages are scaled to the median flux between 5000−6000 Å. We can see how the spectra at 40−60 d look very similar to the average spectra. The object quickly deviates from the average after this point particularly around the Ca NIR triplet and the Mg I] λ4571 emission line. Spectra are from Nicholl et al. (2019a), Lin et al. (2023), and Zhu et al. (2023).

The event also has a steep rise time, and although the colour initially reddens, it becomes bluer about 30 post-peak (Kangas et al. 2022). The deviation of this object from the general population at late times demonstrates the effectiveness of PCA in picking out events with unique observables.

In the final panels from both Figs 16(d) and 17(d), we can see a cluster of red diamonds quite distinct from the central grouping. These red points correspond to the spectra of SN 2017egm. The separation of this object from the rest is particularly pronounced when comparing the first component to the rest. This separation is supported by Fig. 15, which shows a silhouette plot for the parameter space corresponding to the first two components in the bin at 80–500 scaled days from explosion. This panel had one of the highest silhouette score at 0.47, close to the 0.5 threshold generally used to distinguish reasonable clusters. In fact, comparing component one against components three, four, and five resulted in silhouette scores of 0.56, 0.59, and 0.60 respectively. This may initially suggest there are two distinct groups here, however, when we consider that the majority of these points are from a single object it supports the idea that there is a unique object rather than distinct group. We can also see in Fig. 15 that a few points in the second group, from objects other than SN 2017egm, have negative silhouette scores.

The spectra of SN 2017egm in the final time bins are shown in Fig. 19. In this Figure, all spectra including the averages are normalized to the median flux between 5000 and 6000 Å. From this, we can see how the spectra of SN 2017egm look very similar to the average spectra between 40 and 60 d; however, they deviate increasingly from the averages calculated in Section 3 at later times. We can see that at later times SN 2017egm has a cooler underlying blackbody continuum compared to the averages, but the most striking feature is the Ca II NIR triplet, which is significantly stronger than the other emission lines. This is not the case in the average spectra, where this line is much more comparable in strength to other nearby lines. The inclusion of SN 2017egm in the PCA decomposition could be driving the multiple components with strong Ca II NIR features as this object is likely responsible for a lot of the variance in the data set. This is explored in Appendix D where this analysis is rerun with the spectra of SN 2017egm removed. This event is also unusual in terms of its light curve, displaying undulating features and multiple bumps (Lin et al. 2023; Zhu et al. 2023). The time period of the spectra displayed in Fig. 19 correspond to a bump in the light curve, followed by a steep decline. This has been attributed to interaction with a shell of CSM, followed by a sharp decline as the shockwave reaches the edge of the material (Zhu et al. 2023). If the late-time line excitation in SN 2017egm is dominated by interaction, the fact that it is a significant outlier from the average spectrum could imply that a different mechanism dominates the line formation in more typical SLSNe.

5 LINE VELOCITIES

The dynamics of SN explosions can be investigated through the study of absorption velocities, which probe the structure of the expanding ejecta. Light-curve measurements only constrain the ratio of ejecta mass and velocity (Arnett 1982). Instead, an independent velocity measurement is essential to break this degeneracy and estimate the mass.

Different theoretical models predict different time evolution for line velocities in SLSNe, depending on the source of energy injection. Early 1D magnetar models predicted that observed velocities would

initially decline with time as the photosphere receded, followed by a plateau in the velocity evolution (e.g. Kasen & Bildsten 2010; Dessart et al. 2012). This behaviour was caused by the internal magnetar wind sweeping up the inner ejecta into a dense shell with a constant velocity. However, multidimensional simulations have provided a different perspective. 2D models show that the magnetar energy can induce turbulence in the ejecta, disrupting the formation of a narrow, dense shell (Chen, Woosley & Sukhbold 2016; Suzuki et al. 2021). This instead spreads the inner ejecta down to lower velocities. In 3D models (Suzuki & Maeda 2019; Chen et al. 2020), we again see a density profile that declines smoothly as a function of velocity coordinate and therefore would expect to see a smooth decline in the observed line velocity too.

Within the CSM interaction model, we might expect the velocity of the lines to decrease quickly as the rapid deceleration of ejecta produces the observed luminosity. Sorokina et al. (2016) suggest that the spectra of SLSNe could result from interactions with a fast-moving shell, where the outer edge reaches the observed absorption velocities, while the inner edge remains nearly stationary. However, there are issues with this model such as the broad spectral features of SLSNe pointing towards a significant amount of high-velocity material, which conflicts with the idea of a thin shell. Other theories propose that the interaction layer may not produce the absorption lines, but instead dilute them by enhancing the blue continuum (Branch et al. 2000; Sollerman et al. 2020). However, the broad absorption lines in SLSNe seem to show similar equivalent widths even when the continuum luminosity is different, suggesting no such dilution effect in observed events (Nicholl et al. 2017a; Yan et al. 2018). Even if broad lines are observed from the SN ejecta, we might also expect to see some lines with lower velocities, from any absorption or emission that takes place in the dense CSM.

Notably, the Fe II λ5169 absorption line has been identified by Branch et al. (2002) as a valuable tracer of photospheric velocity. Iron is a useful tracer in SN ejecta because its distribution peaks towards the centre, with the most iron-rich region of the line forming region coinciding with the photosphere. From a previous study of 21 SLSNe by Liu et al. (2017), we know that the velocity of this line decreases over time as the ejecta expands, and inner, slower moving layers of material are revealed. In their analysis, the velocity of the line at 10 d post-peak was around 15 000 km s^{-1}, before gradually decreasing to about 10 000 km s^{-1} by 30 d post-peak.

5.1 Velocity measurements

For the current analysis, we measured the velocity of the Fe II λ5169 line. This line is usually blended with Fe II λ4924 and Fe II λ5018, making it difficult to measure the absorption minimum of the 5169 Å line cleanly. Therefore Liu et al. (2017) used a template matching method developed in Modjaz et al. (2016) using template spectra of SNe Ic, and applied to SNe Ic-BL and SLSNe, as this feature is present in all three sub-types. This method applies a convolution with a Gaussian to broaden the line profiles, and a blueshift assumed to reflect the velocity difference between the template and the spectrum of interest.

Here we apply a modified version of the Modjaz et al. (2016) code to our sample of SLSN spectra. This method uses Markov chain Monte Carlo (MCMC) to fit SN Ic template spectra at different phases to the SLSN spectra. It does this by first identifying peaks on either side of the absorption profile, either from the continnum level or the P-Cygni maxima, and using the wavelength range between these peaks for fitting the line. For this analysis, the allowed region used to search for the 'blue' peak was constrained to 4300−4800 Å and the 'red' peak to 5000−5700 Å across all spectra. Using MCMC, the following parameters were fit: v, the blueshift velocity of the line with respect to the template spectrum; σ, the broadening of the line with respect to the template spectrum; Δw, a parameter that adjusts the initial wavelength range using the 'blue' and 'red' peaks; a, the amplitude; and offset, this applies a vertical offset to the template. Here, we implement a method with uniform priors for all parameters and ranges between v: −5000 and 30 000 km s^{-1}, σ: 0.1 and 50 km s^{-1}, a: 0 and 9, Δw: −100 and 100 Å, offset: −1 and 1. We also initiated the walkers at randomly sampled values along these priors. This differs from Modjaz et al. (2016), who used a Gaussian prior for Δw centred on 0 and set the 99.7$^{\text{th}}$ percentile to be 100 Å. An example fit is shown in Fig. 20 for a spectrum of SN 2016wi.

Before employing the MCMC, spectra were first flattened by taking continua regions on either side of the profile between 4000−4500 Å and 5500−6000 Å. These regions were used to compute a linear fit for the underlying continuum that was then subtracted from the spectrum. The continuum-subtracted spectrum between 4000 and 6000 Å was then used for our analysis.

Only spectra with phases between 10 and 80 d with respect to peak were fit. This is due to the contamination from Fe III at early times. Liu et al. (2017) disregard all spectra before 15 d due to this contamination; however, Inserra et al. (2018) use phases as low as 10 d. For this reason we include phases from 10 d to be inclusive in our measurements. The phases also had an upper limit imposed of 80 d as the template spectra only cover phases up to 72 d after peak.

For each velocity measurement, a SN Ic template needs to be selected. The Fe II line in each template also has an inherent velocity, reported in Modjaz et al. (2016). This was added to the relative blueshift velocity derived by each template fit to calculate a final physical velocity. The line profiles and relative strengths of the Fe II blend vary with phase from peak, so that different templates provide more appropriate comparisons at different phases. However, as SLSNe evolve more slowly than SNe Ic, the same phase for SNe Ic cannot be assumed for SLSNe. We tried several methods for selecting template spectra at different phases based on the relative decline rates of SLSNe and SNe Ic. In the end we found that this did not make a significant difference to the velocity measurements, and in some cases decreased the fit quality. We therefore report results based on fits that used the template at the same phase from peak as the SLSN spectrum in question.

The difficulty in matching the phases of SLSNe and SNe Ic for such a large sample is a possible caveat in this analysis. Other caveats include that in some cases the Fe II lines could not be fit very well either due to the line being too noisy, or too weak. These spectra were removed manually after visual inspection of the fits. Performing a KS test on the peak apparent magnitudes of the spectra that were retained, and those that were removed gives a p-value of 0.68, indicating they are likely drawn from the same distribution. A KS test was also performed on the redshift distribution of these spectra resulting in a p-value of 0.53. From this we can infer that the removal of spectra was likely not biased by luminosity or redshift. In total, this resulted in 247 velocities from 111 different objects.

The final velocities of the Fe II λ5169 line are plotted in Fig. 21 against phase from peak. We can see a significant spread in velocities across the entire time frame. Close to 10 d post-peak, some events, such as SN 2019otl, exhibit velocities nearing 27 000 km s^{-1}, whereas other events such as SN 2018fcg and PTF10bjp, show velocities closer to 10 000 km s^{-1}. This wide range of velocities persists even at late times, with a spread of approximately 10 000 km s^{-1}

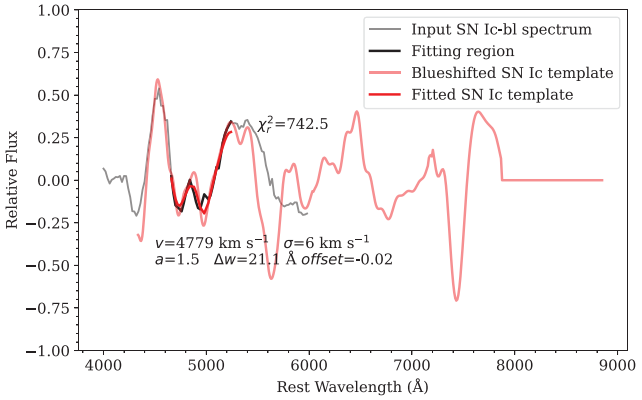

Figure 20. Example fit of the Fe II λ5169 feature to a spectrum of SN 2016wi. The blueshifted template spectrum is shown in red matched to the target spectrum in black. The bold lines for both colours show the fitting region chosen by the code with the bold red line also broadened to match the width of the target feature. Median values for the parameter fits are printed.

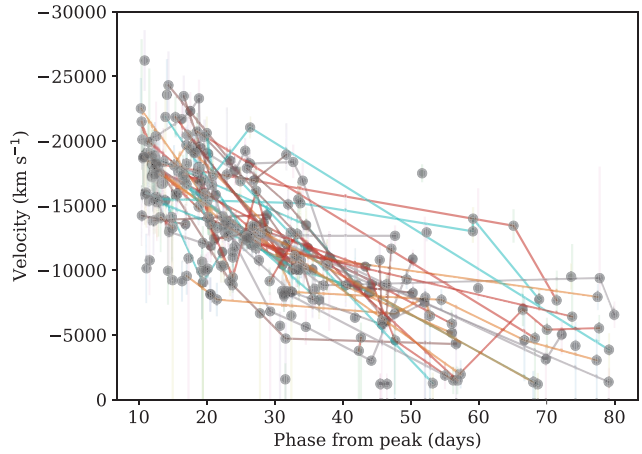

Figure 21. Velocity evolution over time in the rest-frame for the Fe II λ5169 line. Phase is measured from the peak of the light curve. Displayed are velocities 247 velocity measurements from 111 different objects. Coloured lines connect the velocities for individual events.

still observed at 80 d post-peak. We note that the velocity for some events using this method does not match reported velocities in the literature. For example, SN 2018ibb shows a velocity from ∼15 000 km s^{-1} to ∼6000 km s^{-1} over the time frame. Comparing this to the velocity measured in Schulze et al. (2024), which remains consistent around ∼8500 km s^{-1} over this time frame. This may be a result of the different methods used to measure the velocity, and also the broad range of priors required to the fit the line profiles in this sample. Fig. 21 also displays a gradual decrease in measured velocity over time. This is due to the photosphere receding inwards, allowing us to see slower moving material closer to the SN core.

Comparing our results to the sample of 21 SLSNe from Liu et al. (2017), we can see that their sample exhibit comparable velocities to our sample at similar epochs. They also applied this method to measure the velocity of the Fe line of SNe Ic and SNe Ic-BL. To investigate the evolution of each population, they employed moving weighted averages to compare velocities across the three SN classes. Their analysis showed that SLSNe and SNe Ic-BL follow a similar pattern of velocity evolution, with both displaying significantly higher velocities than SNe Ic at early times. By approximately 40 d after peak brightness, however, the velocities of all three classes converged to similar values.

Further insights into this relationship were provided by Finneran, Cotter & Martin-Carrillo (2024), who analysed 61 SNe Ic-BL, and 13 SNe Ic associated with gamma-ray bursts (GRB-SNe). Their findings showed that SNe Ic-BL have velocities comparable to GRB-SNe, though the latter consistently occupy the upper end of the velocity distribution. The velocities of SLSNe in this sample overlap with those measured in Finneran et al. (2024), but they generally fall below the velocities observed for GRB-SNe.

Our findings and previous work show that SLSNe have similar velocities to some SNe Ic-BL, but at the lower end of the distribution. This may provide an important clue to the energy sources that accelerate and heat the ejecta. The discovery of a SLSN associated with an ultra-long GRB (Greiner et al. 2015) suggests that SLSNe and GRBs may represent different manifestations of the same type of stellar explosion.

This is supported by their spectral similarities in the nebular phase (Nicholl et al. 2016b) and their preference for low-metallicity host environments (Lunnan et al. 2014), with SLSNe typically found in galaxies with less than 0.4 solar metallicity and long GRBs in environments with less than 0.7 solar metallicity (Leloudas et al. 2015; Schulze et al. 2018). The distinction could lie in the time-scale of energy injection: SLSNe are thought to involve prolonged energy injection, which drives late-time heating, whereas GRBs are characterized by a rapid release of energy that accelerates the ejecta (Metzger et al. 2015; Margalit et al. 2018; Metzger, Beniamini & Giannios 2018). In the magnetar central engine model, this variation in time-scale could arise from differences in magnetar field strength.

5.2 Where are the lines and the continuum formed?

As mentioned in Section 5.1, the velocity of the Fe II λ5169 line is often used as a proxy for the photospheric velocity for rapidly expanding ejecta. This is often an assumption made in the expanding photosphere method for SNe II (Kirshner & Kwan 1974). However, depending on the assumed powering mechanism of SLSNe, this is not necessarily at the same location where the bulk of the continuum luminosity is produced. For example, in SNe with strong CSM interaction, most of the continuum emission will be generated in the shocked CSM exterior to the fast-expanding ejecta. In order to gain an understanding of where the line and continuum form in relation to one another, we can compare the implied photospheric radius derived from fitting a blackbody model to the SED, to the photospheric radius derived from the Fe II λ5169 line velocity.

The Fe II radius was derived by taking the earliest velocity measurement for each object and multiplying it by the time from explosion to when the spectrum was obtained in rest-frame days. This provides an estimated upper limit for the distance the material could have travelled in that time. This was then compared to the blackbody radius derived from fitting the light-curve SED in Gomez et al. (2024) using `extrabol` (Thornton et al. 2024) at the same phase. Fig. 22 shows the ratio of the Fe II radius to the blackbody radius, plotted against the blackbody radius. The mean of the ratio is 1.39 ± 0.90 indicating the radii measured using both methods are consistent with one another. From this we can infer that the velocity measured by the Fe II λ5169 line is indeed a good tracer for the photospheric velocity and therefore the Fe line forms in a region close to the rapidly expanding photosphere. This suggests that the bulk of the light is coming from a region close to the fast-moving ejecta. This picture

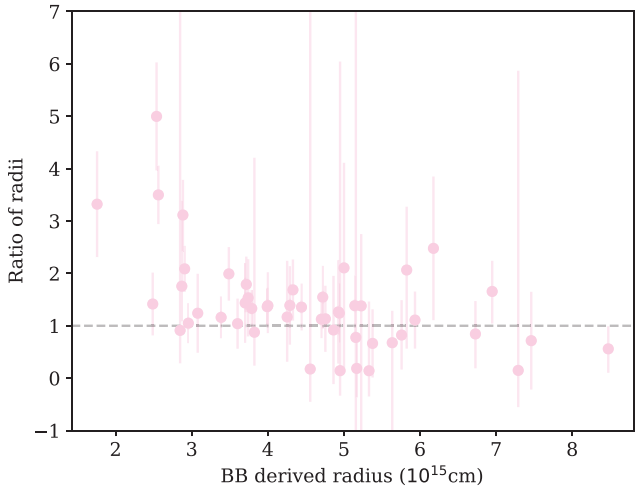

Figure 22. The blackbody radius of the SNe at peak plotted against the ratio of the radius derived from the iron line velocity, to the blackbody radius. The blackbody derived values are taken from Gomez et al. (2024). The dashed horizontal line indicates the value at which both radii would be equal.

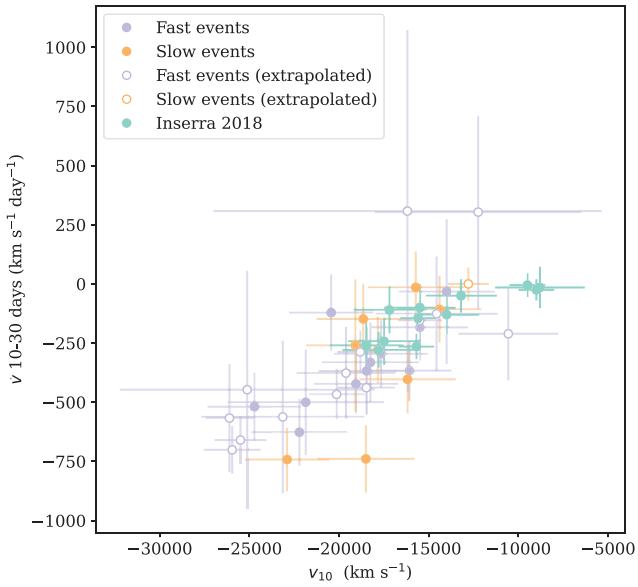

Figure 23. Velocity at 10 d versus the change in velocity from 10 to 30 d for 34 events. Events with 'fast' light-curve evolutions (defined as $\tau_e \leq 30$ d) are shown in purple. Unfilled circles indicate extrapolated points for those events without a spectrum between 10 and 15 d post-peak, and therefore the velocity at 10 d has been extrapolated from the line of best fit. Plotted in blue are the measurements from Inserra et al. (2018).

is consistent with centrally powered models, where the electron-scattering photosphere that produces the continuum lies within the SN ejecta and the Fe II lines form just outside, but still within the ejecta. It could also be consistent with interaction models, if the CSM is quite confined, and the optically thick CSM is not much larger than the radius reached by the fast ejecta at maximum light. However, this situation may require an aspherical CSM and a viewing angle that allows us to see the fast ejecta at the same time as the dense CSM.

5.3 Change in photospheric velocity

We investigated the photospheric evolution in this sample by looking at the velocity from the Fe II λ5169 line at 10 d (v_{10}), versus the rate of change of velocity from 10 to 30 d ($\dot{v}$) following Inserra et al. (2018). Objects were first checked to identify those with two or more spectra taken between 10 and 50 d post-peak, with a minimum time span of 5 d between the earliest and latest observations within this window. For these objects, the velocity evolution over time was linearly fit with the reciprocal of the errors used as weights. If there was a spectrum between 10 and 15 d post-peak, the spectrum closest to 10 d was used for v_{10}. Otherwise the linear fit was used to extrapolate v_{10} and these points are marked as unfilled circles in Fig. 23. The velocity at 30 d (v_{30}), was extrapolated from the line of best fit. If only two spectra were available, the errors on v_{10} and v_{30} were obtained by using the errors on the first and last spectrum. If more than two spectra were available, the errors were derived from the covariance matrix of the fit. There are large error bars for a few points with extrapolated values for v_{10}. This can be explained by the need to extend the linear fits of the velocity evolution in some cases by over 10 d.

Comparing our sample to that in Inserra et al. (2018), we find both samples follow the same shape as shown in Fig. 23. However, our sample extends further into higher v and $\dot{v}$ values. This systematic offset could be due to differences in the way the velocities were calculated. In Inserra et al. (2018), the velocity is measured by fitting the absorption minima of the profile but this is affected by blending from Fe II λ4924 and Fe II λ5018 at early times. Inserra et al. (2018) state that the strong linear relationship of their version of this plot indicates that the faster the photospheric velocity, the faster the velocity decreases. For this data set we find a Spearman's rank correlation coefficient of 0.78, with a p-value $\ll 0.05$, indicating a strong positive correlation between $\dot{v}$ and v_{10} that is statistically significant. We can therefore conclude a linear relationship between these parameters and so also find that for faster initial velocities, the decrease in velocity is also faster.

Physically, we can interpret this result by considering the SN ejecta to be in homologous expansion as shown:

$$v(r) = v_0 \frac{r}{R}. \tag{1}$$

In equation (1), $v(r)$ represents the velocity at a given radius r. R is the radius of the outer most ejecta, and v_0 is the scale velocity. The velocity at the photosphere follows $v_{\rm phot} = v(r_{\rm phot})$. We know the location of the photosphere relates to the optical depth (τ) through the relation:

$$\tau = \int_{r_{\rm phot}}^{R} \kappa\, \rho(r,t) {\rm d}r = \frac{2}{3}. \tag{2}$$

Here, κ is the opacity, and ρ is the density. This density is a function of the radius r, which itself evolves with time (and is proportional to v_0). Therefore,

$$\rho(t) \propto \frac{1}{R^3} \propto \frac{1}{v_0^3}. \tag{3}$$

For events with a larger-scale velocity, the density decreases faster and from equation (2) we see deeper into the ejecta to slower moving material at any given time. This results in a larger change in the measured photospheric velocity within a given time interval. Using v_{10} as a proxy for v_0, we do indeed see that events with a larger scale velocity show larger velocity changes within 30 d. This suggests that the observed correlation is consistent with all SLSNe forming these lines close to the photosphere of the homologously expanding ejecta of comparable density, with a scale velocity that varies between events.

We also split our sample into events with 'fast' and 'slow' light-curve evolution, coloured by purple and orange points respectively. The split of events into fast and slow categories was assigned based on having an e-folding decline time in the light curve of above or below 30 d. This is motivated by the debate in the literature over whether they represent distinct populations or a continuum of properties. Some argue that these systems arise from the same explosion mechanism with differences in evolution explained by different ejecta masses (Nicholl et al. 2015a) and heating time-scales (Nicholl et al. 2017c). Others argue that the diversity of the population points to distinct sub-groups (Quimby et al. 2018; Könyves-Tóth 2022) that could be powered by different engines (Inserra et al. 2018).

Inserra et al. (2018) claimed that when splitting the data based on light-curve time-scale, the slow events also showed low v and slow $\dot{v}$, while the faster events showed both high v and $\dot{v}$. Although this divide looks clear in Inserra et al. (2018), in our sample the two groups overlap significantly with no clear distinction between fast and slow events. To support this visual assessment, KMeans clustering was applied to this data to see if the data could be explained by two groups. We can see a silhouette plot to represent this in Fig. 24. The top panel shows the silhouette scores for each point, with an average silhouette score of 0.57 for the whole sample. This indicates a preference for two clusters; however, it is not a strong clustering. From the bottom panel of this figure, we can see that the grouping of points do not have a distinct cut off and are blended into one another. This is supported by calculating the median decline time in each group, producing a comparable 38 d for group 0, and 37 d for group 1. This indicates that both clusters in this case contain a mix of both fast and slow events. We also performed BIC analysis on this data for 2–5 clusters and find no strong evidence for any of these numbers of clusters.

6 CONCLUSIONS

In this paper we have presented the largest sample of photospheric spectra for Type I SLSNe. This has been collated from ePESSTO+, the FLEET search, and all published spectra up to 2022 December. The main conclusions from this analysis are as follows:

(i) Creating average spectra shows that SLSNe initially have high temperatures of around 10000−11000 K before peak, with blue continua and relatively weak lines. This is followed by a rapid spectral change in a period of cooling up to 40 d after peak, where the lines transition to P-Cygni profiles, and strengths increase relative to the continuum.
This indicates spectral changes are driven by the temperature evolution.

(ii) In the late photospheric phase from 40 d post-peak, temperatures plateau to 5000−6000 K. These spectra show much more pronounced line features, though still with a strong underlying blackbody continuum. This temperature range matches the results from light-curve models such as MOSFiT and REDBACK which introduce a final temperature parameter that generally converges to a similar value.

(iii) The average spectra suggest there may be a small amount of He retained by many SLSNe at the time of their explosion. This is seen by the consistent troughs for prominent He lines at ∼7500 km s^{-1} for spectra 20−40 d post-peak, and at ∼6000 km s^{-1} at 60−80 d post-peak.

(iv) There is no evidence for distinct spectral subclasses within the SLSN population when decomposing using KMeans clustering

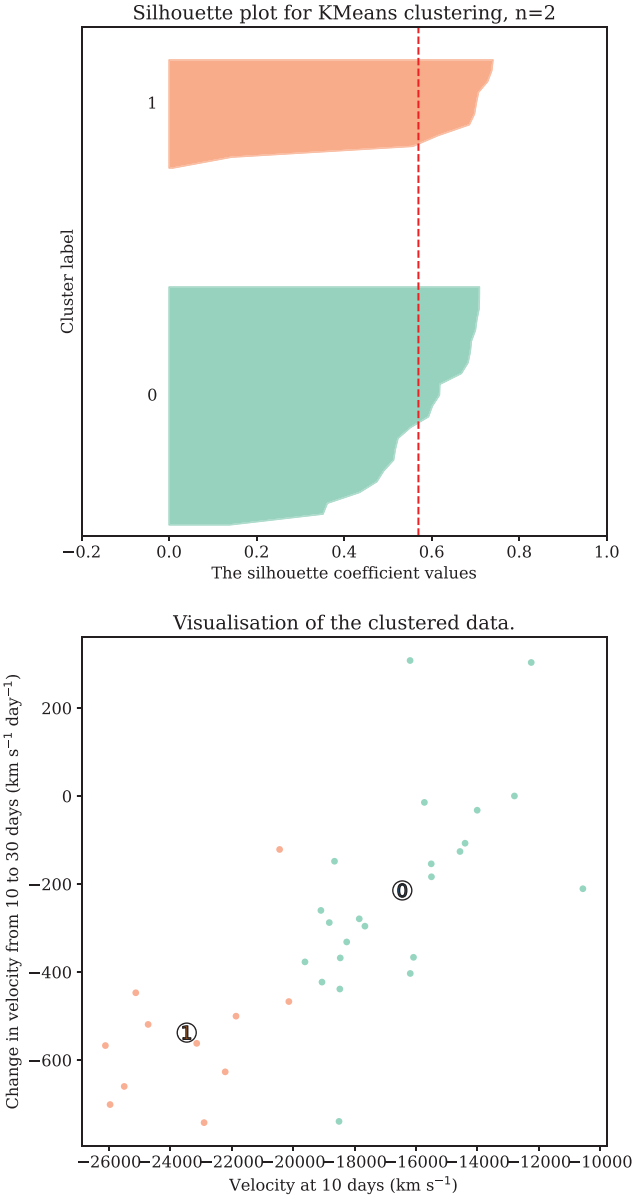

Figure 24. Silhouette plot using a cluster size of two applied to the data from Fig. 23. These plots show the quality of clustering by displaying the silhouette coefficient for each point, which measures how well the point fits within its assigned cluster compared to the nearest neighbouring cluster. Values range from −1 to 1, with higher values indicating well-separated clusters, while negative values suggest possible misclassification. The mean silhouette score, shown as a red vertical line, summarizes clustering performance. With a score of 0.57, this suggests a preference for two distinct clusters. However, these clusters do not coincide with the separate groupings of 'fast' and 'slow' events.

and testing with the Bayesian Information Criterion, however, there are a few outliers. Notably SN 2017egm deviates from the general population due to its very strong Ca NIR triplet emission. This coincides with when the event undergoes bumps in its light curve due to interaction with shells of CSM. This suggests that significant CSM interaction can influence both the light-curve and spectral evolution, and line emission of these events.

(v) We find that the variance between spectra within a given time bin was slightly reduced when binning with respect to the time of explosion, rather than peak, and after normalizing the phase using

the decline time-scale of each light curve. This is supported by the PCA decomposition which required fewer components to explain the same level of variation when grouping the spectra based on scaled phase from explosion rather than phase from peak. However, we find that the overall reduction in variance is surprisingly small. We suggest that this is because most SLSNe have a similar temperature at maximum light, and it is the temperature evolution, rather than time since explosion, that controls the spectrum.

(vi) We find good agreement between the velocity based on blackbody fits (Gomez et al. 2024), and the Fe II λ5169 line velocity at peak. From this we can infer the Fe line forming region is close to the photosphere where the bulk of the thermal emission is produced. This is naturally consistent with a centrally powered model, where the continuum-forming photosphere lies within the SN ejecta, with Fe II lines just outside. Interaction models could also be viable if the CSM is compact and the Fe II lines form in the fast ejecta close to the CSM but that has not yet collided with it. However, this may require an aspherical CSM and a favourable viewing angle to observe both the fast ejecta and dense CSM simultaneously.

(vii) We find events with faster photospheric velocities, also have a faster velocity gradient, consistent with previous findings in the literature. We suggest that this correlation arises naturally from a physical interpretation in which larger scale velocities within a homologously expanding ejecta lead us to see deeper into the ejecta after any given time interval, and therefore lead to larger changes in line velocities. KMeans clustering indicates a slight preference for two clusters with a silhouette score of 0.57; however, each cluster group is composed of a mixture of events with 'fast' and 'slow' light-curve evolutions, complicating any picture where SLSNe separate cleanly by both time-scale and velocity.

The analysis in this paper suggests that most SLSNe can be explained as a single population of events, with the bulk of the spectral lines forming above a photosphere within homologously expanding ejecta. We suggest that this is more naturally consistent with an internal powering mechanism, but the identification of outliers such as SN 2017egm shows that interaction, when present, can significantly alter this evolution.

Next-generation surveys will dramatically expand our sample of SLSNe. These facilities will provide an unprecedented opportunity for spectroscopic follow-up, allowing us to characterize the diversity of SLSNe, track their evolution, and test explosion models. The spectral data set presented here will serve as an important benchmark for interpreting these future observations, and in particular in identifying outliers that follow-up efforts should focus on, maximizing the scientific return from these upcoming surveys.

ACKNOWLEDGEMENTS

We would like to thank Maryam Modjaz for helpful inputs and discussions.

AA and MN are supported by the European Research Council (ERC) under the European Union's Horizon 2020 research and innovation programme (grant agreement no. 948381).

SG is supported by an STScI Postdoctoral Fellowship.

The Berger Time-Domain Group is supported in part by NSF and NASA funds.

AA and T-WC acknowledge the Yushan Young Fellow Program by the Ministry of Education, Taiwan, for the financial support (MOE-111-YSFMS-0008-001-P1).

This work was funded by ANID, Millennium Science Initiative, ICN12_009.

LG and CPG acknowledge financial support from Centro Superior de Investigaciones Científicas (CSIC) under the PIE project 20215AT016, the Spanish Ministerio de Ciencia e Innovación (MCIN) and the Agencia Estatal de Investigación (AEI) 10.13039/501100011033 under the PID2023-151307NB-I00 SNNEXT project, the program Unidad de Excelencia María de Maeztu CEX2020-001058-M, and the Departament de Recerca i Universitats de la Generalitat de Catalunya through the 2021-SGR-01270 grant. LG also acknowledges financial support from AGAUR, ILINK23001, and COOPB2304. CPG acknowledges financial support from the Secretary of Universities and Research (Government of Catalonia) and by the Horizon 2020 Research and Innovation Programme of the European Union under the Marie Skłodowska-Curie and the Beatriu de Pinós 2021 BP 00168 programme.

HK was funded by the Research Council of Finland projects 324504, 328898, and 353019.

GL was supported by a research grant (VIL60862) from VILLUM FONDEN.

TEMB is funded by Horizon Europe ERC grant no. 101125877.

MR acknowledge support from National Agency for Research and Development (ANID) grants ANID-PFCHA/Doctorado Nacional/2020-21202606.

AS acknowledges support from the Knut and Alice Wallenberg foundation through the 'Gravity Meets Light' project.

SS is partially supported by LBNL Subcontract 7707915.

This paper includes data gathered with the 6.5m Magellan Telescopes located at Las Campanas Observatory, Chile. Observations reported here were obtained at the MMT Observatory, a joint facility of the Smithsonian Institution and the University of Arizona.

Based on observations collected at the European Organisation for Astronomical Research in the Southern Hemisphere, Chile, as part of PESSTO (the Public ESO Spectroscopic Survey for Transient Objects – PI: Smartt), ePESSTO, and ePESSTO + (the advanced Public ESO Spectroscopic Survey for Transient Objects Survey – PI: Inserra), under ESO programme IDs 188.D-3003, 191.D-0935, 1103.D-0328, 106.216C and 108.220C.

This work made use of the data products generated by the Modjaz group (formerly NYU SN group), and released under DOI:10.5281/zenodo.58766, available at https://github.com/nyusngroup/SESNtemple/.

DATA AVAILABILITY

This data will be publicly available on Github.[8] Previously unpublished raw spectra will also be publicly uploaded to the Weizmann Interactive Supernova Data Repository (WISeREP[9])

REFERENCES

Aamer A. et al., 2024, MNRAS, 527, 11970
Anderson J. P., 2019, A&A, 628, A7
Anderson J. P. et al., 2018, A&A, 620, A67
Angus C., 2022, Transient Name Serv. Classif. Rep., 2022-1769, 1
Angus C. R., Levan A. J., Perley D. A., Tanvir N. R., Lyman J. D., Stanway E. R., Fruchter A. S., 2016, MNRAS, 458, 84
Angus C. R. et al., 2019, MNRAS, 487, 2215
Angus C. R. et al., 2024, ApJ, 977, L41
Arcavi I. et al., 2016, ApJ, 819, 35
Arnett W. D., 1982, ApJ, 253, 785

[8] https://github.com/gmzsebastian/SLSNe
[9] https://www.wiserep.org

Astropy Collaboration et al., 2018, AJ, 156, 123
Ayala B., Gutierrez C., Kravtsov T., Yaron O., 2022, Transient Name Serv. Classif. Rep., 2022-2393, 1
Barbary K. et al., 2009, ApJ, 690, 1358
Barkat Z., Rakavy G., Sack N., 1967, Phys. Rev. Lett., 18, 379
Bellm E. C. et al., 2019, PASP, 131, 018002
Blanchard P. K. et al., 2018a, ApJ, 865, 9
Blanchard P., Nicholl M., Berger E., 2018b, Transient Name Serv. Classif. Rep., 2018-2025, 1
Blanchard P. K., Berger E., Nicholl M., Villar V. A., 2020a, ApJ, 897, 114
Blanchard P., Gomez S., Hosseinzadeh G., Berger E., 2020b, Transient Name Serv. Classif. Rep., 2020-3871, 1
Blanchard P., Chornock R., Nicholl M., Berger E., Gomez S., Hosseinzadeh G., 2021a, Transient Name Serv. Classif. Rep., 2021-1566, 1
Blanchard P., Berger E., Gomez S., Hosseinzadeh G., 2021b, Transient Name Serv. Classif. Rep., 2021-276, 1
Bose S. et al., 2018, ApJ, 853, 57
Branch D., Jeffery D. J., Blaylock M., Hatano K., 2000, PASP, 112, 217
Branch D. et al., 2002, ApJ, 566, 1005
Bromm V., Larson R. B., 2004, ARA&A, 42, 79
Bruch R., Anderson J., Gutierrez C., Irani I., 2021, Transient Name Serv. Classif. Rep., 2021-3392, 1
Burke J., Hiramatsu D., Arcavi I., Howell D. A., Mccully C., Valenti S., 2018, Transient Name Serv. Classif. Rep., 2018-1719, 1
Campbell H. et al., 2014, Astron. Telegram, 6524, 1
Chambers K. C. et al., 2016, preprint (arXiv:1612.05560)
Chatzopoulos E., Wheeler J. C., Vinko J., 2012, ApJ, 746, 121
Chatzopoulos E., Wheeler J. C., Vinko J., Horvath Z. L., Nagy A., 2013, ApJ, 773, 76
Chen T.-W. et al., 2013, ApJ, 763, L28
Chen K.-J., Woosley S. E., Sukhbold T., 2016, ApJ, 832, 73
Chen T. W. et al., 2017, A&A, 602, A9
Chen K.-J., Woosley S. E., Whalen D. J., 2020, ApJ, 893, 99
Chen T. W. et al., 2021, preprint (arXiv:2109.07942)
Chen Z. H. et al., 2023a, ApJ, 943, 41
Chen Z. H. et al., 2023b, ApJ, 943, 42
Chevalier R. A., Irwin C. M., 2011, ApJ, 729, L6
Childress M. J. et al., 2016, PASA, 33, e055
Chomiuk L. et al., 2011, ApJ, 743, 114
Chornock R., Bhirombhakdi K., Katebi R., Blanchard P., Nicholl M., Berger E., 2018, Transient Name Serv. Classif. Rep., 2018-1257, 1
Christensen L., Fynbo J. P. U., Prochaska J. X., Thöne C. C., de Ugarte Postigo A., Jakobsson P., 2011, ApJ, 727, 73
Chu M., Dahiwale A., Fremling C., 2021a, Transient Name Serv. Classif. Rep., 2021-2748, 1
Chu M., Dahiwale A., Fremling C., 2021b, Transient Name Serv. Classif. Rep., 2021-3171, 1
Chu M., Dahiwale A., Fremling C., 2022, Transient Name Serv. Classif. Rep., 2022-1071, 1
Clark P., McBrien O., Magee M., Yaron O., Knezevic N., 2018, Transient Name Serv. Classif. Rep., 2018-2100, 1
Cleland C., McGee S. L., Nicholl M., 2023, MNRAS, 524, 3559
Colgate S. A., McKee C., 1969, ApJ, 157, 623
Dahiwale A., Fremling C., 2020a, Transient Name Serv. Classif. Rep., 2020-1494, 1
Dahiwale A., Fremling C., 2020b, Transient Name Serv. Classif. Rep., 2020-1504, 1
Dahiwale A., Fremling C., 2020c, Transient Name Serv. Classif. Rep., 2020-1756, 1
Dahiwale A., Fremling C., 2021, Transient Name Serv. Classif. Rep., 2021-1234, 1
Dahiwale A., Fremling C., Sharma Y., 2019a, Transient Name Serv. Classif. Rep., 2019-2837, 1
Dahiwale A., Dugas A., Fremling C., 2019b, Transient Name Serv. Classif. Rep., 2019-2859, 1
Davis K., Foley R., Dimitriadis G., Soto K. D., 2022, Transient Name Serv. Classif. Rep., 2022-1881, 1
De Cia A. et al., 2018, ApJ, 860, 100
Deckers M., Prentice S., Maguire K., Dimitriadis G., Magee M., Harvey L., Terwel J., 2021, Transient Name Serv. Classif. Rep., 2021-1365, 1
Decleir M. et al., 2022, ApJ, 930, 15
Dessart L., 2019, A&A, 621, A141
Dessart L., Hillier D. J., Waldman R., Livne E., Blondin S., 2012, MNRAS, 426, L76
Dexter J., Kasen D., 2013, ApJ, 772, 30
Dong S. et al., 2017, Astron. Telegram, 10498, 1
Dong S. et al., 2018, Astron. Telegram, 11654, 1
Dressler A. et al., 2011, PASP, 123, 288
Drout M. R. et al., 2011, ApJ, 741, 97
Fabricant D., Cheimets P., Caldwell N., Geary J., 1998, PASP, 110, 79
Fabricant D. et al., 2019, PASP, 131, 075004
Finneran G., Cotter L., Martin-Carrillo A., 2024, preprint (arXiv:2411.11503)
Fiore A. et al., 2021, MNRAS, 502, 2120
Fiore A. et al., 2022, MNRAS, 512, 4484
Fitzpatrick E. L., Massa D., Gordon K. D., Bohlin R., Clayton G. C., 2019, ApJ, 886, 108
Fremling C., Dahiwale A., 2019, Transient Name Serv. Classif. Rep., 2019-1774, 1
Fremling C., Dugas A., Sharma Y., 2018a, Transient Name Serv. Classif. Rep., 2018-1416, 1
Fremling C., Dugas A., Sharma Y., 2018b, Transient Name Serv. Classif. Rep., 2018-1877, 1
Fremling C., Dugas A., Sharma Y., 2018c, Transient Name Serv. Classif. Rep., 2018-2145, 1
Fremling C., Sharma Y., Dahiwale A., 2019a, Transient Name Serv. Classif. Rep., 2019-1838, 1
Fremling C., Dugas A., Sharma Y., 2019b, Transient Name Serv. Classif. Rep., 2019-188, 1
Fremling C., Dahiwale A., Dugas A., 2019c, Transient Name Serv. Classif. Rep., 2019-1923, 1
Fremling C., Dugas A., Sharma Y., 2019d, Transient Name Serv. Classif. Rep., 2019-636, 1
Fremling C., Dugas A., Sharma Y., 2019e, Transient Name Serv. Classif. Rep., 2019-747, 1
Fremling C., Dugas A., Sharma Y., 2019f, Transient Name Serv. Classif. Rep., 2019-799, 1
Fremling C., Dugas A., Sharma Y., 2019g, Transient Name Serv. Classif. Rep., 2019-952, 1
Frohmaier C. et al., 2019, Astron. Telegram, 12844, 1
Fulton M. et al., 2022, Transient Name Serv. Classif. Rep., 2022-2128, 1
Gal-Yam A., 2019a, ARA&A, 57, 305
Gal-Yam A., 2019b, ApJ, 882, 102
Gal-Yam A., Cenko S. B., Fox D. B., Leonard D. C., Moon D. S., Sand D. J., Soderberg A. M., 2007, in di Salvo T., Israel G. L., Piersant L., Burderi L., Matt G., Tornambe A., Menna M. T., eds, AIP Conf. Ser. Vol. 924, The Multicolored Landscape of Compact Objects and Their Explosive Origins. Am. Inst. Phys., New York, p. 297
Gal-Yam A. et al., 2009, Nature, 462, 624
Ginzburg S., Balberg S., 2012, ApJ, 757, 178
Gkini A. et al., 2024, A&A, 685, A20
Gkini A. et al., 2025, A&A, 694, A292
Gomez S., 2019, Transient Name Serv. Classif. Rep., 2019-1246, 1
Gomez S. et al., 2019, ApJ, 881, 87
Gomez S., Berger E., Blanchard P. K., Hosseinzadeh G., Nicholl M., Villar V. A., Yin Y., 2020a, ApJ, 904, 74
Gomez S., Hosseinzadeh G., Berger E., Blanchard P., 2020b, Transient Name Serv. Classif. Rep., 2020-3149, 1
Gomez S., Hosseinzadeh G., Berger E., Blanchard P., 2020c, Transient Name Serv. Classif. Rep., 2020-3506, 1
Gomez S., Hosseinzadeh G., Berger E., Blanchard P., 2021a, Transient Name Serv. Classif. Rep., 2021-1647, 1
Gomez S., Berger E., Blanchard P., Nicholl M., 2021b, Transient Name Serv. Classif. Rep., 2021-1675, 1
Gomez S., Hosseinzadeh G., Berger E., Blanchard P., 2021c, Transient Name Server Classif. Rep., 2021-1716, 1

Gomez S., Hosseinzadeh G., Berger E., Blanchard P., 2021d, Transient Name Serv. Classif. Rep., 2021-2719, 1
Gomez S., Hosseinzadeh G., Berger E., Blanchard P., 2021e, Transient Name Serv. Classif. Rep., 2021-3270, 1
Gomez S., Hosseinzadeh G., Blanchard P., Berger E., 2021f, Transient Name Serv. Classif. Rep., 2021-3444, 1
Gomez S., Hosseinzadeh G., Blanchard P., Berger E., 2021g, Transient Name Serv. Classif. Rep., 2021-3662, 1
Gomez S., Berger E., Blanchard P., Nicholl M., 2021h, Transient Name Serv. Classif. Rep., 2021-564, 1
Gomez S., Hosseinzadeh G., Berger E., Blanchard P., 2021i, Transient Name Serv. Classif. Rep., 2021-565, 1
Gomez S., Berger E., Nicholl M., Blanchard P. K., Hosseinzadeh G., 2022a, ApJ, 941, 107
Gomez S., Hiramatsu D., Blanchard P., Berger E., 2022b, Transient Name Serv. Classif. Rep., 2022-777, 1
Gomez S., Berger E., Blanchard P. K., Hosseinzadeh G., Nicholl M., Hiramatsu D., Villar V. A., Yin Y., 2023a, ApJ, 949, 114
Gomez S., Hiramatsu D., Blanchard P., Berger E., 2023b, Transient Name Serv. Classif. Rep., 2023-1030, 1
Gomez S. et al., 2024, MNRAS, 535, 471
Gonzalez E. P., Hiramatsu D., Burke J., Howell D. A., McCully C., Pellegrino C., 2021, Transient Name Serv. Classif. Rep., 2021-1220, 1
Gordon K. D., Cartledge S., Clayton G. C., 2009, ApJ, 705, 1320
Gordon K. D. et al., 2021, ApJ, 916, 33
Gordon K. D., Clayton G. C., Decleir M., Fitzpatrick E. L., Massa D., Misselt K. A., Tollerud E. J., 2023, ApJ, 950, 86
Greiner J. et al., 2015, Nature, 523, 189
Gromadzki M., Cartier R., Yaron O., 2021, Transient Name Serv. Classif. Rep., 2021-3651, 1
Grzesiak K., Gromadzki M., Kravtsov T., Ihanec N., Bruch R. J., 2022, Transient Name Serv. Classif. Rep., 2022-3521, 1
Gutiérrez C. P. et al., 2022, MNRAS, 517, 2056
Heger A., Woosley S. E., 2002, ApJ, 567, 532
Hiramatsu D., Arcavi I., Burke J., Hosseinzadeh G., Howell D. A., Mccully C., Valenti S., 2018, Transient Name Serv. Classif. Rep., 2018-679, 1
Hiramatsu D., Berger E., Gomez S., Blanchard P. K., Kumar H., Athukoralalage W., 2024, preprint (arXiv:2411.07287)
Hosseinzadeh G., Berger E., Metzger B. D., Gomez S., Nicholl M., Blanchard P., 2022, ApJ, 933, 14
Hotelling H., 1933, J. Educ. Psychol., 24, 498
Howell D. A. et al., 2013, ApJ, 779, 98
Hsiao E. Y., Conley A., Howell D. A., Sullivan M., Pritchet C. J., Carlberg R. G., Nugent P. E., Phillips M. M., 2007, ApJ, 663, 1187
Ihanec N., Gromadzki M., Wevers T., Irani I., 2020, Transient Name Serv Classif. Rep., 2020-3296, 1
Inserra C., 2019, Nat. Astron., 3, 697
Inserra C. et al., 2013, ApJ, 770, 128
Inserra C. et al., 2017, MNRAS, 468, 4642
Inserra C., Prajs S., Gutierrez C. P., Angus C., Smith M., Sullivan M., 2018, ApJ, 854, 175
Jaeger T. D., Huber M., 2020, Transient Name Serv. Classif. Rep., 2020-3720, 1
Jerkstrand A. et al., 2017, ApJ, 835, 13
Kangas T. et al., 2017, MNRAS, 469, 1246
Kangas T. et al., 2022, MNRAS, 516, 1193
Kasen D., Bildsten L., 2010, ApJ, 717, 245
Kass R. E., Raftery A. E., 1995, Journal of the American Statistical Association, 90, 773
Kirshner R. P., Kwan J., 1974, ApJ, 193, 27
Könyves-Tóth R., 2022, ApJ, 940, 69
Könyves-Tóth R., Vinkó J., 2021, ApJ, 909, 24
Kouveliotou C. et al., 1998, Nature, 393, 235
Kumar A. et al., 2020, ApJ, 892, 28
Kuncarayakti H. et al., 2023, A&A, 678, A209
Leloudas G. et al., 2012, A&A, 541, A129
Leloudas G. et al., 2015, MNRAS, 449, 917
Lin W. L. et al., 2020, MNRAS, 497, 318
Lin W. et al., 2023, Nat. Astron., 7, 779
Liu Y.-Q., Modjaz M., Bianco F. B., 2017, ApJ, 845, 85
Lloyd S., 1982, IEEE Trans. Inf. Theor., 28, 129
Lunnan R. et al., 2013, ApJ, 771, 97
Lunnan R. et al., 2014, ApJ, 787, 138
Lunnan R. et al., 2016, ApJ, 831, 144
Lunnan R. et al., 2018a, Nat. Astron., 2, 887
Lunnan R. et al., 2018b, ApJ, 852, 81
Lunnan R. et al., 2020, ApJ, 901, 61
Margalit B., Metzger B. D., Thompson T. A., Nicholl M., Sukhbold T., 2018, MNRAS, 475, 2659
Matheson T., Filippenko A. V., Li W., Leonard D. C., Shields J. C., 2001, AJ, 121, 1648
Mazzali P. A., Sullivan M., Pian E., Greiner J., Kann D. A., 2016, MNRAS, 458, 3455
Mcbrien O., Clark P., Kankare E., Yaron O., Knezevic N., 2018, Transient Name Serv. Classif. Rep., 2018-587, 1
Metzger B. D., Margalit B., Kasen D., Quataert E., 2015, MNRAS, 454, 3311
Metzger B. D., Beniamini P., Giannios D., 2018, ApJ, 857, 95
Modjaz M., Liu Y. Q., Bianco F. B., Graur O., 2016, ApJ, 832, 108
Moriya T. J., 2024, preprint (arXiv:2407.12302)
Moriya T. J., Blinnikov S. I., Tominaga N., Yoshida N., Tanaka M., Maeda K., Nomoto K., 2013, MNRAS, 428, 1020
Neill J., 2017, Transient Name Serv. Classif. Rep., 2017-1084, 1
Neill J. D. et al., 2011, ApJ, 727, 15
Nicholl M., 2021, Astron. Geophys., 62, 5
Nicholl M. et al., 2013, Nature, 502, 346
Nicholl M. et al., 2014, MNRAS, 444, 2096
Nicholl M. et al., 2015a, MNRAS, 452, 3869
Nicholl M. et al., 2015b, ApJ, 807, L18
Nicholl M. et al., 2016a, ApJ, 826, 39
Nicholl M. et al., 2016b, ApJ, 828, L18
Nicholl M., Berger E., Margutti R., Blanchard P. K., Milisavljevic D., Challis P., Metzger B. D., Chornock R., 2017a, ApJ, 835, L8
Nicholl M., Berger E., Margutti R., Blanchard P. K., Guillochon J., Leja J., Chornock R., 2017b, ApJ, 845, L8
Nicholl M., Guillochon J., Berger E., 2017c, ApJ, 850, 55
Nicholl M., Gomez S., Blanchard P., (harvard/cfa E. B., 2018, Transient Name Serv. Classif. Rep., 2018-653, 1
Nicholl M., Berger E., Blanchard P. K., Gomez S., Chornock R., 2019a, ApJ, 871, 102
Nicholl M., Short P., Lawrence A., Ross N., Smartt S., Oates S., 2019b, Transient Name Serv. Classif. Rep., 2019-2271, 1
Omand C. M. B., Jerkstrand A., 2023, A&A, 673, A107
Ostriker J. P., Gunn J. E., 1971, ApJ, 164, L95
Pan Y. C. et al., 2017, MNRAS, 470, 4241
Pastorello A. et al., 2010, ApJ, 724, L16
Pearson K., 1901, London, Edinburgh, and Dublin Phil. Mag. J. Sci., 2, 559
Perez-Fournon I. et al., 2020, Transient Name Serv. Classif. Rep., 2020-2456, 1
Perez-Fournon I. et al., 2022, Transient Name Serv. Classif. Rep., 2022-2201, 1
Perley D. A., 2019, Transient Name Serv. Classif. Rep., 2019-1646, 1
Perley D. A. et al., 2016, ApJ, 830, 13
Perley D., Yan L., Lunnan R., Gal-Yam A., Schulze S., Yaron O., 2019a, Transient Name Serv. Classif. Rep., 2019-1186, 1
Perley D., Yan L., Andreoni I., Karambelkar V., Sharma Y., De K., Fremling C., Kulkarni S., 2019b, Transient Name Serv. Classif. Rep., 2019-1712, 1
Perley D., Sollerman J., Fremling C., Dahiwale A., Walters R., 2020, Transient Name Serv. Classif. Rep., 2020-3125, 1
Perley D. A., Yao Y., Chen T., Schulze S., Sharma Y., Ho A. Y. Q., Yan L., Kulkarni S. R., 2021, Transient Name Serv. Classif. Rep., 2021-1649, 1
Perley D., Meynardie W., Chu M., Fremling C., 2022a, Transient Name Serv. Classif. Rep., 2022-3555, 1
Perley Yan Group Z. S., 2022b, Transient Name Serv. Classif. Rep., 2022-49, 1

Poidevin F. et al., 2020, Transient Name Serv. Classif. Rep., 2020-500, 1
Poidevin F. et al., 2021, Transient Name Serv. Classif. Rep., 2021-2271, 1
Poidevin F. et al., 2022a, Transient Name Serv. Classif. Rep., 2022-1175, 1
Poidevin F. et al., 2022b, Transient Name Serv. Classif. Rep., 2022-3606, 1
Poidevin F. et al., 2023, MNRAS, 521, 5418
Prentice S. J., Maguire K., Skillen K., Magee M. R., Clark P., 2019a, Transient Name Serv. Classif. Rep., 2019-1598, 1
Prentice S. J., Maguire K., Skillen K., Magee M. R., Clark P., 2019b, Transient Name Serv. Classif. Rep., 2019-2339, 1
Prentice S. J. et al., 2021, MNRAS, 508, 4342
Pursiainen M. et al., 2022, A&A, 666, A30
Quimby R. M., Aldering G., Wheeler J. C., Höflich P., Akerlof C. W., Rykoff E. S., 2007, ApJ, 668, L99
Quimby R. M. et al., 2011, Nature, 474, 487
Quimby R. M. et al., 2018, ApJ, 855, 2
Rau A. et al., 2009, PASP, 121, 1334
Ridley E., Gompertz B., Nicholl M., Galbany L., Yaron O., 2021, Transient Name Serv. Classif. Rep., 2021-2795, 1
Rodríguez Ó., Maoz D., Nakar E., 2023, ApJ, 955, 71
Rodríguez Ó., Nakar E., Maoz D., 2024, Nature, 628, 733
Sarin N. et al., 2024, MNRAS, 531, 1203
Savitzky A., Golay M. J. E., 1964, Anal. Chem., 36, 1627
Schlafly E. F., Finkbeiner D. P., 2011, ApJ, 737, 103
Schmidt G. D., Weymann R. J., Foltz C. B., 1989, PASP, 101, 713
Schulze S. et al., 2018, MNRAS, 473, 1258
Schulze S. et al., 2021, ApJS, 255, 29
Schulze S. et al., 2024, A&A, 683, A223
Schwarz G., 1978, Ann. Stat., 6, 461
Selsing J., Fynbo J. P. U., Christensen L., Krogager J. K., 2016, A&A, 585, A87
Shivvers I. et al., 2019, MNRAS, 482, 1545
Smartt S. J. et al., 2015, A&A, 579, A40
Smith M., 2019, Transient Name Serv. Classif. Rep., 2019-522, 1
Smith N. et al., 2007, ApJ, 666, 1116
Smith M. et al., 2016, ApJ, 818, L8
Smith M. et al., 2018, ApJ, 854, 37
Sollerman J., 2022, Transient Name Serv. Classif. Rep., 2022-1899, 1
Sollerman J. et al., 2020, A&A, 643, A79
Sorokina E., Blinnikov S., Nomoto K., Quimby R., Tolstov A., 2016, ApJ, 829, 17
Srivastav S. et al., 2021, Transient Name Serv. AstroNote, 11, 1
Stevenson K. B., Bean J. L., Seifahrt A., Gilbert G. J., Line M. R., Désert J.-M., Fortney J. J., 2016, ApJ, 817, 141
Suzuki A., Maeda K., 2019, ApJ, 880, 150
Suzuki A., Nicholl M., Moriya T. J., Takiwaki T., 2021, ApJ, 908, 99
Taddia F. et al., 2019, A&A, 621, A71
Terreran G., 2020a, Transient Name Serv. Classif. Rep., 2020-2618, 1
Terreran G., 2020b, Transient Name Serv. Classif. Rep., 2020-2902, 1
Terreran G., 2020c, Transient Name Serv. Classif. Rep., 2020-3507, 1
Thornton I., Villar V. A., Gomez S., Hosseinzadeh G., 2024, Res. Notes Am. Astron. Soc., 8, 48
Tinyanont S., Dimitriadis G., Foley R. J., 2020, Transient Name Serv. Classif. Rep., 2020-3473, 1
Vreeswijk P. M. et al., 2014, ApJ, 797, 24
Wang L.-J., Liu L.-D., Lin W.-L., Wang X.-F., Dai Z.-G., Li B., Song L.-M., 2022, ApJ, 933, 102
Weil K. E., Milisavljevic D., 2020, Transient Name Serv. Classif. Rep., 2020-3413, 1
Weil K. E., Milisavljevic D., 2021, Transient Name Serv. Classif. Rep., 2021-2881, 1
Weil K. E., Subrayan B. M., Milisavljevic D., 2021, Transient Name Serv. Classif. Rep., 2021-2270, 1
West S. L. et al., 2023, A&A, 670, A7
Williamson M., Modjaz M., Bianco F. B., 2019, ApJ, 880, L22
Woods P. M., Thompson C., 2006, in Lewin W. H. G., van der Klis M., eds, Compact stellar X-ray sources, Vol. 39. Cambridge Astrophysics Series, Cambridge, p. 547
Woosley S. E., 2010, ApJ, 719, L204
Woosley S. E., Blinnikov S., Heger A., 2007, Nature, 450, 390
Xiang D., Rui L., Wang X., Song H., Xiao F., Zhang T., Zhang J., 2017, Transient Name Serv. Classif. Rep., 2017-599, 1
Yan L., Group Z. S., 2022, Transient Name Serv. Classif. Rep., 2022-45, 1
Yan L. et al., 2015, ApJ, 814, 108
Yan L. et al., 2017a, ApJ, 840, 57
Yan L. et al., 2017b, ApJ, 848, 6
Yan L., Perley D. A., De Cia A., Quimby R., Lunnan R., Rubin K. H. R., Brown P. J., 2018, ApJ, 858, 91
Yan L. et al., 2020, ApJ, 902, L8
Yan L., Schulze S., Group Z. S., 2022, Transient Name Serv. Classif. Rep., 2022-47, 1
Yao Y., Velzen S. V., Tzanidakis A., Gezari S., Hammerstein E., Somalwar J., Kulkarni S., 2021, Transient Name Serv. Classif. Rep., 2021-1614, 1
Yaron O., Young D., Smith K., Smartt S., 2023, Transient Name Serv. AstroNote, 112, 1
Young D. R. et al., 2010, A&A, 512, A70
Zheng W., Patra K., Brink T., Filippenko A. V., 2019, Transient Name Serv. Classif. Rep., 2019-1331, 1
Zhu J. et al., 2023, ApJ, 949, 23

SUPPORTING INFORMATION

Supplementary data are available at *MNRAS* online.

suppl_data

Please note: Oxford University Press is not responsible for the content or functionality of any supporting materials supplied by the authors. Any queries (other than missing material) should be directed to the corresponding author for the article.

APPENDIX A: OBJECTS AND DATA IN SAMPLE

Table A1. Phases of spectra used in the analysis of this paper with both phases from peak, and phases from explosion presented. Superscript [a] denotes extra levels of processing where telluric removal was rerun on smoothed and rebinned spectra. Superscript [b] denotes where host galaxy line removal was not performed, and superscript [c] indicates spectra that had their edges cut to remove noise. Superscript [d] indicates where spectra had chip gaps or noisy middles which were masked, and superscript [e] denotes spectra that were not used in the analysis of this paper.

Object	Redshift	Phase from Peak	Phase from Explosion	Source
1991D	0.04179	29.17, 43.04	45.71, 59.58	Matheson et al. (2001)
1999as	0.127	0.98, 10.75, 10.75, 31.15, 36.48	31.18, 40.94, 40.94, 61.35, 66.67	
2002gh	0.3653	35.59, 58.29, 61.96, -0.3, 7.02, 9.95, 16.55, 19.48, 20.21	101.15, 123.86, 127.52, 65.26, 72.58, 75.51, 82.11, 85.04, 85.77	
2005ap	0.2832	−4.13, 2.88, 26.26	10.06, 17.07, 40.45	Gal-Yam et al. (2007); Quimby et al. (2007)
2006oz	0.376	-17.65^{ace}	23.7^{ace}	Leloudas et al. (2012)
2007bi	0.1279	51.13^{ac}, 52.9, 99.01, 130.92, 45.46, 45.81	104.68^{ac}, 106.45, 152.56, 184.48, 99.01, 99.36	Gal-Yam et al. (2009); Young et al. (2010); Shivvers et al. (2019)
2009cb	0.1867	15.66	33.28	Quimby et al. (2018)
2009jh	0.3499	77.5, 117.51, -8.43, -8.43, 13.05, 30.83	135.16, 175.16, 49.23, 49.23, 70.71, 88.49	Quimby et al. (2011, 2018)
2010gx	0.2297	-7.34, -4.9, -4.08^{ad}, 4.05, 9.74, 10.56, 21.13^{acd}, 29.26, 33.33, 56.91^{ac}, 66.67	16.08, 18.52, 19.33^{ad}, 27.46, 33.15, 33.97, 44.54^{acd}, 52.67, 56.74, 80.32^{ac}, 90.08	Pastorello et al. (2010); Quimby et al. (2011, 2018)
2010hy	0.1901	16.78, 38.66, 40.12, 60.47	56.04, 77.92, 79.38, 99.73	Quimby et al. (2018); Shivvers et al. (2019)
2010kd	0.101	83.0, 126.58, -29.42, -25.81, -24.91, -23.97, 9.53, 26.75	134.88, 178.47, 22.46, 26.07, 26.97, 27.91, 61.41, 78.63	Kumar et al. (2020)
2010md	0.0987	67.34^{ac}, 74.62, 79.18, 80.09, 100.11, 126.5, -22.76, -3.65, 20.01, 20.92, 26.39, 30.94, 31.85, 51.87	107.96^{ac}, 115.25, 119.8, 120.71, 140.73, 167.12, 17.86, 36.97, 60.64, 61.55, 67.01, 71.56, 72.47, 92.49	Inserra et al. (2013); Quimby et al. (2018); Shivvers et al. (2019)
2011ke	0.1428	10.96, 12.71, 14.46, 20.59, 23.21, 27.59, 29.34, 29.34, 34.59, 36.34, 44.22, 50.34^{ac}, 56.47	36.88, 38.63, 40.38, 46.51, 49.13, 53.51, 55.26, 55.26, 60.51, 62.26, 70.13, 76.26^{ac}, 82.39	Inserra et al. (2013); Quimby et al. (2018)
2011kf	0.245	17.33, 43.83	42.44, 68.95	Inserra et al. (2013)
2011kg	0.1924	−11.51, 157.05, -8.16, -0.61, 6.1, 6.1, 6.94, 13.64^{a}, 18.68, 43.0, 44.67^{ac}	18.47, 187.03, 21.82, 29.37, 36.08, 36.08, 36.92, 43.63^{a}, 48.66, 72.98, 74.66^{ac}	Inserra et al. (2013); Quimby et al. (2018)
2011kl	0.677	−3.97	12.06	
2012aa	0.083	94.63, -2.37, 17.04, 36.55	132.07, 35.07, 54.48, 74.0	Shivvers et al. (2019)
2012il	0.175	12.4, 40.49, 52.4^{a}	32.78, 60.87, 72.78^{a}	Inserra et al. (2013)
2013dg	0.265	5.02^{ac}, 7.39^{a}, 8.43, 16.11^{a}, 23.21^{a}, 35.87^{e}, 47.71	31.92^{ac}, 34.29^{a}, 35.33, 43.01^{ae}, 50.11^{a}, 62.77^{e}, 74.61	Nicholl et al. (2014); Shivvers et al. (2019)
2013hy	0.663	33.44	60.18	
2015bn	0.1136	21.56, 22.66, 22.68, 32.34, 32.34, 33.23, 36.98, 45.81, 52.09, 59.28, 73.64, 85.32, 91.6, 100.58, 107.77, -26.03, -24.91, -18.6^{ae}, -17.7, -17.68^{a}, -15.26^{a}, -6.08^{ae}, -5.29, -5.27, 0.01, 1.14, 1.16^{ac}, 2.8^{ae}, 5.4, 9.22^{ac}, 9.24	108.27, 109.37, 109.39, 119.05, 119.05, 119.94, 123.69, 132.52, 138.8, 145.99, 160.35, 172.03, 178.31, 187.29, 194.48, 60.68, 61.8, 68.11^{ae}, 69.01, 69.03^{a}, 71.45^{a}, 80.63^{ae}, 81.42, 81.44, 86.72, 87.85, 87.87^{ac}, 89.51^{ae}, 92.11, 95.93^{ac}, 95.95	Nicholl et al. (2016a); Shivvers et al. (2019)
2016ard	0.2025	79.13, 119.88, -4.03, -3.7^{ac}, 6.78, 24.24, 31.73	109.63, 150.38, 26.47, 26.8^{ac}, 37.28, 54.74, 62.23	Chornock et al. (2018); Blanchard et al. (2018a)
2016eay	0.1013	−19.68, 150.4, 159.27, -16.88, -14.17, -10.53^{ac}, -10.53^{ac}, -8.72, -6.9, -5.08, -4.18, 2.18, 2.18, 12.14^{a}, 16.71, 20.34, 21.2^{a}, 25.79, 31.17, 42.95	18.92, 189.0, 197.87, 21.72, 24.43, 28.07^{ac}, 28.07^{ac}, 29.88, 31.7, 33.51, 34.42, 40.78, 40.78, 50.74^{a}, 55.31, 58.94, 59.8^{a}, 64.39, 69.77, 81.55	Kangas et al. (2017); Nicholl et al. (2017a); Yan et al. (2017a)
2016inl	0.3057	15.02	74.39	Blanchard et al. (2021a)
2016wi	0.224	84.64^{ac}, 105.07^{ac}, -10.34, 7.63, 12.2, 28.87, 33.16^{ac}, 34.92, 56.11	126.92^{ac}, 147.36^{ac}, 31.94, 49.92, 54.49, 71.16, 75.44^{ac}, 77.21, 98.4	Yan et al. (2017b)
2017dwh	0.13	6.88	29.63	Blanchard, Nicholl & Berger (2018b)
2017egm	0.03072	−61.16, -57.25, -56.92, -56.91, -56.3, 48.44, -46.23, 59.15, -45.3, 80.5, 80.8, 86.31, 87.2, 90.65, 91.1^{ad}, 91.17, -41.4, 105.2, 106.74, -40.18, -40.16^{ac}, 112.47, -39.8^{ac}, -39.43, 123.63, -38.39^{e}, 132.83, 138.67, -36.52, -35.32, -32.66, -30.69^{a}, -25.87, -9.43, -51.35, -49.47, -49.08	−3.2, 0.71, 1.04, 1.05, 1.66, 106.4, 11.73, 117.11, 12.66, 138.46, 138.76, 144.27, 145.16, 148.6, 149.06^{ad}, 149.13, 16.55, 163.16, 164.7, 17.78, 17.8^{ac}, 170.43, 18.16^{ac}, 18.53, 181.59, 19.57^{e}, 190.79, 196.63, 21.44, 22.63, 25.3, 27.27^{a}, 32.09, 48.53, 6.61, 8.49, 8.88	Dong et al. (2017); Xiang et al. (2017); Nicholl et al. (2017b); Bose et al. (2018); Lin et al. (2023); Zhu et al. (2023)
2017gci	0.087	72.85, 103.2, 131.03, 133.62, 155.67, -7.02, -5.17, -3.35, -2.43, 3.1^{e}, 23.65, 29.17^{e}, 32.46, 37.43^{e}, 42.05^{e}, 50.87^{b}	100.09, 130.43, 158.26, 160.85, 182.9, 20.21, 22.06, 23.88, 24.8, 30.33^{e}, 50.88, 56.4^{e}, 59.69, 64.67^{e}, 69.28^{e}, 78.1^{b}	Fiore et al. (2021)

Table A1 – *continued*

Object	Redshift	Phase from Peak	Phase from Explosion	Source
2017hbx	0.1652	9.43[b]	32.05[b]	Neill (2017)
2018avk	0.132	−21.54[a], -21.54[a], -13.46, -12.7	43.93[a], 43.93[a], 52.0, 52.77	Nicholl et al. (2018); Lunnan et al. (2020)
2018beh	0.06	−9.4[e], -8.49, -5.49[b], -2.87, 7.5[a]	28.45[e], 29.36, 32.36[b], 34.98, 45.35[a]	Mcbrien et al. (2018)
2018bgv	0.0795	−1.81[ac], 0.07, 2.85, 11.14[ac], 13.97, 13.97, 19.44[ac], 22.31, 53.8	13.79[ac], 15.67, 18.45, 26.74[ac], 29.57, 29.57, 35.04[ac], 37.91, 69.4	Dong et al. (2018); Lunnan et al. (2020)
2018bsz	0.0267	−12.73, 88.39, 102.95, 102.98, -10.72[ac], -10.71, 115.61[a], -2.24, 5.55, 12.37[a], 19.19[a], 27.95[ad], 33.8[e], 59.16, 59.19, 60.16, 60.2[a], 68.91, 68.95[a]	11.1, 112.21, 126.78, 126.81, 13.1[ac], 13.12, 139.44[a], 21.58, 29.38, 36.19[a], 43.01[a], 51.78[ad], 57.62[e], 82.98, 83.01, 83.99, 84.03[a], 92.74, 92.77[a]	Anderson et al. (2018); Clark et al. (2018); Hiramatsu et al. (2018); Chen et al. (2021); Pursiainen et al. (2022)
2018bym	0.274	73.76, 115.99[ac], 116.86[e], -5.75, 3.67[a], 3.67[a], 7.59, 27.21	115.84, 158.07[ac], 158.94[e], 36.33, 45.75[a], 45.75[a], 49.67, 69.29	Lunnan et al. (2020); Hosseinzadeh et al. (2022)
2018cxa	0.19	19.83[ac], 20.15[ac], 71.41[e]	43.26[ac], 43.58[ac], 94.84[e]	Gomez et al. (2021h)
2018don	0.0734	36.03, -21.73, -8.69, 0.62, 0.62, 1.56[ac], 15.53	108.99, 51.23, 64.27, 73.59, 73.59, 74.52[ac], 88.49	Lunnan et al. (2018b); Fremling, Sharma & Dahiwale (2019a)
2018fcg	0.1011	−6.42, 11.15[a], 60.02[a]	14.87, 32.44[a], 81.31[a]	
2018fd	0.263	56.7[e]	167.23[e]	Gomez et al. (2021h)
2018ffs	0.141	−8.85[e], 49.67[a]	32.64[e], 91.16[a]	Fremling, Dugas & Sharma (2018c)
2018gbw	0.3454	−2.74	29.43	
2018gft	0.232	−44.96	31.26	
2018gkz	0.2405	12.87[b], 26.2	81.51[b], 94.84	Fremling, Dugas & Sharma (2018a)
2018hpq	0.124	14.98	65.47	
2018hti	0.0612	47.34, 49.38, 49.4, 61.46[ac], 64.87, 68.95, 69.89, 72.22, 81.87, 84.42, 101.39, -37.12, -34.53, -32.89, -30.63, -30.59, -27.72[a], -26.36, -21.79, -18.51, -17.14, -16.88, -15.71, -11.25, -10.51, -8.89, -8.87[a], -1.39[ac], -1.38[a], 4.54, 5.69, 9.34, 10.53, 12.59, 16.36, 17.6, 18.87, 19.06, 20.25, 20.26, 24.2, 25.67, 26.36, 32.73, 34.13, 38.03, 44.16	102.51, 104.55, 104.56, 116.62[ac], 120.03, 124.11, 125.05, 127.38, 137.03, 139.58, 156.56, 18.04, 20.64, 22.27, 24.54, 24.58, 27.45[a], 28.8, 33.37, 36.66, 38.02, 38.28, 39.45, 43.91, 44.66, 46.27, 46.29[a], 53.77[ac], 53.79[a], 59.7, 60.85, 64.5, 65.69, 67.75, 71.52, 72.77, 74.04, 74.23, 75.41, 75.43, 79.36, 80.83, 81.52, 87.89, 89.29, 93.2, 99.33	Burke et al. (2018); Lin et al. (2020); Fiore et al. (2022)
2018ibb	0.166	−5.51, -5.21, 1.57[b], 4.12[b], 5.01, 6.72, 6.74, 17.9[e], 20.47, 23.85, 27.28, 27.3, 28.88[ae], 28.88[ae], 43.3[ac], 43.3[ac], 43.53[e], 47.75, 47.77, 56.28[a], 66.49, 70.04, 70.06, 77.72[a], 85.53	107.75, 108.05, 114.83[b], 117.38[b], 118.27, 119.98, 120.0, 131.16[e], 133.73, 137.11, 140.54, 140.56, 142.14[ae], 142.14[ae], 156.56[ac], 156.56[ac], 156.79[e], 161.01, 161.03, 169.54[a], 179.75, 183.3, 183.32, 190.98[a], 198.79	Fremling, Dugas & Sharma (2018b); Schulze et al. (2024)
2018kyt	0.108	9.49[a], 49.4	46.95[a], 86.86	Fremling, Dugas & Sharma (2019b)
2018lfd	0.2686	−4.33	36.55	
2018lfe	0.35	82.63[a], 32.93, 33.86[ac], 39.84[ac], 57.37[ad], 64.19[e]	111.89[a], 62.19, 63.12[ac], 69.1[ac], 86.63[ad], 93.45[e]	Gomez (2019)
2018lzv	0.434	−19.74, -19.74	31.21, 31.21	Perley, Yan & Group (2022b)
2018lzw	0.3198	31.36, 31.36	79.88, 79.88	Yan, Schulze & Group (2022)
2018lzx	0.4373	20.09	108.55	
2019J	0.1346	18.13, 18.31	66.49, 66.67	Fremling, Dugas & Sharma (2019e)
2019aamp	0.404	−3.6[b], 10.65	25.38[b], 39.63	Yan & Group (2022)
2019aamq	0.386	2.55	75.19	
2019aamr	0.42	5.32	29.68	
2019aams	0.636	4.63	31.56	
2019aamt	0.2138	16.31	51.19	
2019aamu	0.259	16.07	82.49	
2019aamv	0.3996	−6.65	62.35	
2019aamw	0.22	140.85	198.48	
2019aamx	0.41	22.45	67.94	
2019bgu	0.148	18.82	43.78	
2019cca	0.4103	31.38	66.5	
2019cdt	0.153	12.71, 12.86	37.88, 38.03	Fremling, Dugas & Sharma (2019d)
2019cwu	0.32	−18.56, 23.86[a]	27.42, 69.84[a]	Smith (2019)
2019dgr	0.3815	17.09	46.35	
2019dlr	0.26	60.71[c]	101.71[c]	

Table A1 – *continued*

Object	Redshift	Phase from Peak	Phase from Explosion	Source
2019dwa	0.082	3.49[b]	37.8[b]	Fremling, Dugas & Sharma (2019f)
2019eot	0.3057	−11.84, -11.52	39.84, 40.16	Fremling, Dugas & Sharma (2019g)
2019gam	0.1235	−7.66	61.98	
2019gfm	0.18167	−8.74, -6.05, 13.26, 14.99, 44.59[e], 45.41[e], 56.4[e]	12.12, 14.81, 34.12, 35.85, 65.45[e], 66.27[e], 77.26[e]	Frohmaier et al. (2019)
2019gqi	0.3642	25.92, 31.98[e], 45.7[a], 46.43, 47.17	56.01, 62.08[e], 75.79[a], 76.52, 77.26	
2019hge	0.0866	87.94, 87.97, 97.15, 97.18, -19.37, -18.83, 29.03, 33.74, 33.77, 33.8[a], 33.82, 33.86[a], 33.88[a]	146.0, 146.03, 155.21, 155.24, 38.69, 39.23, 87.09, 91.8, 91.83, 91.86[a], 91.88, 91.92[a], 91.94[a]	Prentice et al. (2019a); Dahiwale, Dugas & Fremling (2019b); Prentice et al. (2021)
2019hno	0.26	3.15	32.66	
2019ieh	0.032	19.33[b], -2.89	32.21[b], 9.99	Zheng et al. (2019); Dahiwale, Fremling & Sharma (2019a)
2019itq	0.481	7.92[a], 10.72[a], 13.87[a], 13.95[a], 28.92[a]	39.76[a], 42.56[a], 45.71[a], 45.79[a], 60.77[a]	Gomez et al. (2021i)
2019kcy	0.399	−18.78, -3.04[a], -3.02[a], 1.27[a], 16.94, 16.95	27.78, 43.53[a], 43.55[a], 47.84[a], 63.51, 63.52	Perley et al. (2019a)
2019kwq	0.49	74.25	111.52	
2019kws	0.1977	20.54	56.72	
2019kwt	0.3562	22.89	86.67	
2019kwu	0.6	27.27	52.26	
2019lsq	0.1295	−4.46, -4.13	32.78, 33.12	Fremling & Dahiwale (2019)
2019neq	0.1059	−10.39, 12.32	19.6, 42.31	Perley (2019)
2019nhs	0.189	−8.72, -8.4[ac], 37.68, 49.43	24.79, 25.1[ac], 71.19, 82.94	Perley et al. (2019b)
2019obk	0.1656	14.31	54.02	
2019otl	0.514	80.89[a], 88.26[a], 10.87	137.58[a], 144.96[a], 67.57	Gomez et al. (2021i)
2019pud	0.1136	−7.81[b], -4.18[ac], -4.18[ac], 53.18	17.0[b], 20.62[ac], 20.62[ac], 77.98	Fremling, Dahiwale & Dugas (2019c); Kangas et al. (2022)
2019pvs	0.167	60.64[ac], 40.95[ac]	114.94[ac], 95.24[ac]	Gomez et al. (2021i)
2019qgk	0.3468	41.82	73.92	
2019sgg	0.5726	−8.43	37.61	
2019sgh	0.344	15.41[a], 32.61, 36.99	36.16[a], 53.36, 57.74	Gomez et al. (2021i)
2019szu	0.212	−12.4, -0.87[a], -0.06[a], -62.8[e], -47.86, -44.65, -42.06[a], -33.88, -23.95[a]	105.89, 117.42[a], 118.22[a], 55.49[e], 70.42, 73.64, 76.22[a], 84.41, 94.34[a]	Nicholl et al. (2019b); Aamer et al. (2024)
2019ujb	0.2008	68.03, -4.3[a], 26.99	106.01, 33.68[a], 64.97	Gomez et al. (2021i)
2019unb	0.0635	53.19, 67.4, 68.28, 97.37, -34.14, -11.51[a], -9.63, 7.93, 18.59, 21.47, 25.06[ae], 35.46[e], 37.34[ac], 41.11	111.55, 125.76, 126.64, 155.73, 24.23, 46.86[a], 48.73, 66.29, 76.96, 79.84, 83.43[ae], 93.82[e], 95.71[ac], 99.47	Prentice et al. (2019b); Dahiwale & Fremling (2020b); Prentice et al. (2021)
2019une	0.1666	72.2[e]	113.57[e]	
2019vvc	0.3314	25.9	67.65	
2019xaq	0.2	25.43[a], 25.87[a]	48.47[a], 48.91[a]	Gomez et al. (2021i)
2019xdy	0.2206	30.79	78.31	
2019zbv	0.3785	−3.69, 6.18	38.94, 48.81	Gomez et al. (2021i)
2019zeu	0.39	31.57	58.57	Gomez et al. (2021i)
2020abjc	0.219	33.48[e], -34.36	140.62[e], 72.78	Blanchard et al. (2020b)
2020abjx	0.39	20.09	115.32	
2020adkm	0.226	32.4[a], -13.91, -7.5, 3.07	106.18[a], 59.87, 66.27, 76.85	Blanchard et al. (2021b)
2020afag	0.3815	14.16	54.98	
2020afah	0.3754	−23.8	36.67	
2020ank	0.2485	−2.6, 1.54, 7.94, 27.9	24.63, 28.78, 35.17, 55.13	Poidevin et al. (2020); Dahiwale & Fremling (2020a)
2020aup	0.31	14.89	35.6	
2020auv	0.28	3.49	26.58	
2020dlb	0.398	0.67	46.49	
2020exj	0.1216	42.39, 42.69[ac]	63.28, 63.58[ac]	Dahiwale & Fremling (2020c)
2020fvm	0.2428	23.84	127.81	
2020fyq	0.1765	46.35	116.57	
2020htd	0.3515	10.83	78.08	
2020iyj	0.369	2.75	47.08	
2020jii	0.396	2.55, 36.22[a]	38.29, 71.96[a]	Gomez et al. (2020b)
2020kox	0.456	−6.37	41.16	
2020myh	0.283	73.61[e], 115.0[ac]	101.69[e], 143.09[ac]	Gomez et al. (2020b)
2020onb	0.153	−27.91, 24.13	18.74, 70.78	Gomez et al. (2020b)

Table A1 – *continued*

Object	Redshift	Phase from Peak	Phase from Explosion	Source
2020qef	0.1831	7.63[a], 30.12	57.08[a], 79.57	Terreran (2020a)
2020qlb	0.1585	53.27, -56.88[b], 110.5, -26.33, 3.56[b], 24.97[ac]	127.83, 17.67[b], 185.06, 48.23, 78.11[b], 99.53[ac]	Perez-Fournon et al. (2020); West et al. (2023)
2020rmv	0.2621	56.06, -8.18, 12.42	114.14, 49.9, 70.5	Terreran (2020b)
2020tcw	0.064	2.83[b]	39.94[b]	Perley et al. (2020)
2020uew	0.22367	77.36[ae], 95.27[a], 119.76, 9.54, 15.22, 17.02, 28.4[a], 32.59, 47.99[a], 54.54[a], 66.74	103.23[ae], 121.14[a], 145.63, 35.41, 41.09, 42.89, 54.27[a], 58.46, 73.86[a], 80.41[a], 92.61	Ihanec et al. (2020); Jaeger & Huber (2020)
2020vpg	0.257	10.42	54.91	Terreran (2020c)
2020wnt	0.032	33.52, 41.08, 47.69, 51.19[ac], 52.16[ac], 52.85, 75.16, 80.97[ac], 101.26, -39.83, -38.64, -38.08, -38.08, -31.38, -29.23, -23.75, -20.54, -11.82, -8.96, -7.22, -6.01, -3.41, 8.14, 8.86, 17.07, 20.57, 21.49, 24.67, 28.32	105.11, 112.66, 119.28, 122.77[ac], 123.75[ac], 124.44, 146.74, 152.56[ac], 172.85, 31.76, 32.95, 33.51, 33.51, 40.21, 42.35, 47.84, 51.05, 59.77, 62.63, 64.37, 65.58, 68.18, 79.73, 80.45, 88.66, 92.16, 93.08, 96.26, 99.91	Tinyanont, Dimitriadis & Foley (2020); Gutiérrez et al. (2022)
2020xga	0.44	−4.3, 2.79, 3.39, 17.22, 33.21[a]	32.85, 39.94, 40.54, 54.37, 70.36[a]	Gkini et al. (2025)
2020xgd	0.454	−1.47, -0.02, 8.27[a], 9.53[a], 10.32[ac], 19.18	28.94, 30.4, 38.68[a], 39.94[a], 40.74[ac], 49.6	Weil & Milisavljevic (2020); Gomez et al. (2020c)
2020xkv	0.241	−13.52	64.41	
2020zbf	0.35	−2.66, 1.78, 18.04[e], 29.14, 38.03[a], 49.82[a]	23.15, 27.58, 43.84[e], 54.94, 63.84[a], 75.63[a]	Gkini et al. (2024)
2020znr	0.1	44.18[a], 0.69[ac], 18.91[ac], 19.79, 20.78[ac], 22.52[ac], 23.54[ac]	117.77[a], 74.28[ac], 92.5[ac], 93.38, 94.37[ac], 96.11[ac], 97.13[ac]	
2020zzb	0.1659	5.76[ac]	78.43[ac]	
2021een	0.16	104.07[a], 31.1, 55.06[e]	132.93[a], 59.96, 83.92[e]	Dahiwale & Fremling (2021)
2021ejo	0.44	39.09[a]	91.86[a]	Gomez et al. (2021b)
2021ek	0.193	−10.47, -6.29, -6.27, 7.96	13.33, 17.5, 17.53, 31.75	Srivastav et al. (2021)
2021fpl	0.121	59.94[a], 115.07[ac], -5.24, 9.07, 9.09[a]	123.64[a], 178.77[ac], 58.46, 72.77, 72.79[a]	Deckers et al. (2021); Poidevin et al. (2023)
2021gtr	0.303	84.56	184.8	Gomez et al. (2021c)
2021hpc	0.24	15.9[a]	56.56[a]	Gomez et al. (2021a)
2021hpx	0.213	−11.01, 12.13	36.33, 59.46	Gonzalez et al. (2021)
2021kty	0.159	−6.45[a]	31.67[a]	Yao et al. (2021)
2021lwz	0.065	−4.72	5.22	Perley et al. (2021)
2021mkr	0.28	−5.68[a], 6.27[ad]	49.11[a], 61.05[ad]	Poidevin et al. (2021); Chu, Dahiwale & Fremling (2021a)
2021nxq	0.15	−26.1	49.12	Weil, Subrayan & Milisavljevic (2021)
2021rwz	0.19	33.39	67.36	Weil & Milisavljevic (2021)
2021txk	0.46	10.43[a], 11.56, 33.58[ace]	40.82[a], 41.95, 63.97[ace]	Gomez et al. (2021d)
2021uvy	0.095	45.95, 56.94, 65.1, 65.14, 71.48, 91.62[ae], 125.35, -12.49[ac], -12.33[ac], 1.37, 6.85, 11.45[ac], 12.59[be], 17.73, 27.88, 35.02[ac]	101.06, 112.04, 120.21, 120.24, 126.58, 146.72[ae], 180.46, 42.61[ac], 42.77[ac], 56.48, 61.95, 66.56[ac], 67.7[be], 72.83, 82.99, 90.12[ac]	Ridley et al. (2021); Chu, Dahiwale & Fremling (2021b)
2021vuw	0.2	61.53[a], 141.44, 22.11[a], 22.51[a], 46.59[a]	107.62[a], 187.53, 68.2[a], 68.6[a], 92.68[a]	Gomez et al. (2021g)
2021xfu	0.32	110.27[a], -19.66, 4.68	172.39[ae], 42.47, 66.81	Gomez et al. (2021e)
2021ybf	0.13	11.47[a], 15.0	61.44[a], 64.97	Bruch et al. (2021)
2021ynn	0.22	84.19[ac], 45.55[ac], 46.55[ac]	110.18[ac], 71.54[ac], 72.55[ac]	Gomez et al. (2023b)
2021yrp	0.3	3.47[a]	38.5[a]	Gomez et al. (2021f)
2021zcl	0.117	56.06, 63.34[a], 89.22[a], -0.25[a], 1.6, 7.84[a], 10.71[a], 26.69[a], 27.57[a], 33.8, 41.81[a]	104.26, 111.54[a], 137.42[a], 47.95[a], 49.8, 56.04[a], 58.91[a], 74.89[a], 75.77[a], 82.0, 90.01[a]	Gromadzki, Cartier & Yaron (2021)
2022aawb	0.13	−11.83	34.51	Poidevin et al. (2022b)
2022abdu	0.13	0.23[a], 1.06[a], 1.09[a], 17.92[a], 25.86[e], 38.25[a], 52.35[ac]	18.23[a], 19.07[a], 19.1[a], 35.93[a], 43.87[e], 56.25[a], 70.36[ac]	Grzesiak et al. (2022)
2022ful	0.15	−4.5[ab], 31.67	35.57[ab], 71.74	Chu, Dahiwale & Fremling (2022); Sollerman (2022)
2022gyv	0.39	5.47	64.6	Poidevin et al. (2022a)
2022le	0.2491	−49.0[a], -47.97[a], -36.91[ac]	174.09[a], 175.12[a], 186.18[ac]	Gomez et al. (2022b)
2022ljr	0.2	13.2	36.15	Davis et al. (2022)
2022lxd	0.54	−8.06[a], 1.93[a]	30.36[a], 40.34[a]	Angus (2022)
2022npq	0.26	−4.1[a]	57.94[a]	Ayala et al. (2022)
2022ojm	0.47	−5.03	41.6	Perez-Fournon et al. (2022)
2022pjq	0.17	−0.93, 27.69[ac]	18.5, 47.12[ac]	Fulton et al. (2022)
2022ued	0.1087	84.04, 35.91[ad]	127.03, 78.9[ad]	Perley et al. (2022a)
2022vxc	0.1	−26.47[ac], -23.75, -54.61, -51.94[a]	117.15[ac], 119.87, 89.01, 91.67[a]	
CSS140925	0.46	8.51, 16.79, 16.81, 16.83	32.75, 41.03, 41.06, 41.08	Campbell et al. (2014)
DES14C1fi	1.302	10.02[e]	43.51[e]	Yaron et al. (2023)

Table A1 – *continued*

Object	Redshift	Phase from Peak	Phase from Explosion	Source
	0.481	4.54	24.44	
DES14C1rhg				
	0.57	−15.52[a]	12.28[a]	
DES14E2slp				
	1.5	9.98	27.66	
DES14S2qri				
	0.868	−2.13[ac]	19.09[ac]	
DES14X2byo				
	0.608	−21.7, -15.39	10.71, 17.02	
DES14X3taz				
	0.392	−1.1[ac]	25.19[ac]	Smith et al. (2016)
DES15C3hav				
	1.861	−2.79, 0.32, 10.83	12.9, 16.01, 26.52	Pan et al. (2017)
DES15E2mlf				
	0.565	32.79[ac]	55.01[ac]	
DES15S1nog				
	1.188	−9.82	36.04	
DES15X1noe				
	0.86	19.96[a]	46.07[a]	
DES15X3hm				
	1.068	−10.01	38.11	
DES16C2aix				
	1.998	15.97, 16.3, 21.06, 21.45, 30.72	41.66, 41.99, 46.75, 47.14, 56.41	Smith et al. (2018)
DES16C2nm				
DES16C3cv	0.727	−3.43	53.79	
	0.562	4.46[ac]	27.06[ac]	
DES16C3dmp				
	0.949	−24.81	31.22	
DES16C3ggu				
	0.47	−7.54	24.69	
DES17C3gyp				
	0.92	−0.42	28.71	
DES17X1amf				
	0.69	2.33[ac]	28.23[ac]	
DES17X1blv				
LSQ12dlf	0.255	7.24, 8.85, 9.91, 10.73, 11.45[ac], 15.99, 19.3[e], 20.75[a], 33.53, 34.86, 43.88	38.81, 40.42, 41.49, 42.31, 43.03[ac], 47.56, 50.88[e], 52.33[a], 65.11, 66.44, 75.46	Nicholl et al. (2014); Childress et al. (2016); Shivvers et al. (2019)
LSQ14an	0.1637	48.92, 53.2, 54.09, 72.14, 91.75, 92.58, 104.66	132.98, 137.26, 138.14, 156.19, 175.8, 176.63, 188.71	Inserra et al. (2017)
LSQ14bdq	0.345	−41.16, -40.35, -39.64	36.61, 37.42, 38.13	Nicholl et al. (2015b)
LSQ14mo	0.256	−5.34, -0.54, 10.47, 16.91, 23.34, 58.27[e]	19.58, 24.38, 35.39, 41.83, 48.27, 83.19[e]	Chen et al. (2017)
OGLE15xl	0.198	102.67, 105.18[a], 106.0[e], 7.75, 8.63, 19.44, 25.3, 42.68[a], 58.57	139.77, 142.27[a], 143.1[e], 44.85, 45.73, 56.53, 62.4, 79.77[a], 95.67	Yaron et al. (2023)
PS110ahf	1.1	−79.19	5.43	
PS110awh	0.9084	−16.79, 7.32, 13.6	11.67, 35.77, 42.06	Chomiuk et al. (2011)
PS110bzj	0.65	8.6, 8.6, 15.87, 17.69[a], 56.48[e]	26.81, 26.81, 34.08, 35.9[a], 74.68[e]	Lunnan et al. (2013)
PS110ky	0.9558	0.08, 2.12, 16.44, 27.69[ac]	13.61, 15.65, 29.97, 41.22[ac]	Chomiuk et al. (2011)
PS110pm	1.206	13.92	41.09	
PS111afv	1.407	4.75	32.75	Lunnan et al. (2018b)
PS111aib	0.997	26.77	92.95	Lunnan et al. (2018b)
PS111ap	0.524	0.98	48.56	
PS111bam	1.565	8.91	30.05	
PS111bdn	0.738	−1.23, -1.17	18.5, 18.56	Lunnan et al. (2018b)
PS111tt	1.283	19.01	63.74	Lunnan et al. (2018b)
PS112bmy	1.572	41.21, 41.25	72.88, 72.92	Lunnan et al. (2018b)
PS112bqf	0.522	1.71	41.16	Lunnan et al. (2018b)
PS112cil	0.32	2.8	31.45	Lunnan et al. (2018b)
PS113gt	0.884	26.13	53.56	Lunnan et al. (2018b)
PS113or	1.52	8.21, 8.21	44.34, 44.34	Lunnan et al. (2018b)
PS114bj	0.5215	−4.94, -4.38, -3.85, -0.57, 34.26[ac], 35.58[ac], -37.82, -24.65	118.43, 118.99, 119.52, 122.8, 157.63[ac], 158.95[ac], 85.55, 98.72	Lunnan et al. (2016)
PS15cjz	0.22	−29.11	25.12	
PTF09atu	0.5015	34.51, 94.45, 113.09, -24.1, -22.77, -0.13, -0.13, 19.19	107.96, 167.9, 186.55, 49.35, 50.68, 73.33, 73.33, 92.64	Quimby et al. (2011, 2018)

Table A1 – *continued*

Object	Redshift	Phase from Peak	Phase from Explosion	Source
PTF09cnd	0.2584	97.66, 119.91, -25.51, -22.33, -15.18, 1.51, 7.87, 22.97, 26.94, 31.71	153.29, 175.54, 30.12, 33.3, 40.45, 57.14, 63.49, 78.59, 82.57, 87.33	Quimby et al. (2011, 2018); Shivvers et al. (2019)
PTF10aagc	0.206	1.86, 2.69, 119.6, 4.34, 13.47, 23.42, 30.05, 75.66	11.88, 12.71, 129.63, 14.37, 23.49, 33.44, 40.07, 85.68	Quimby et al. (2018)
PTF10bfz	0.1701	1.97, 5.39, 13.94, 25.9	22.99, 26.41, 34.95, 46.92	Quimby et al. (2018)
PTF10bjp	0.3584	11.62, 16.78	55.21, 60.37	Quimby et al. (2018)
PTF10iam	0.109	1.36^{a}, 27.84^{ad}, 37.43^{ad}	15.04^{a}, 41.52^{ad}, 51.11^{ad}	Arcavi et al. (2016)
PTF10nmn	0.1237	51.69, 57.92, 58.81, 81.05	113.43, 119.66, 120.55, 142.8	Quimby et al. (2018)
PTF10uhf	0.2882	−3.03, 16.38	18.23, 37.63	Quimby et al. (2018)
PTF10vqv	0.4518	85.02, 85.71, 7.87, 12.01, 22.34, 46.45, 47.82	115.06, 115.75, 37.91, 42.04, 52.38, 76.48, 77.86	Quimby et al. (2018)
PTF12dam	0.1073	40.43^{ac}, 50.37, 50.37, 50.37, 80.17^{a}, 80.17^{a}, -32.72, -31.82, -30.91, -30.01^{ac}, -29.11, -28.2, -28.2, -28.2, -27.3, -21.88^{a}, -15.56^{a}, -10.14, -6.53, -3.82^{a}, -0.21, -0.21, 3.4, 9.73, 14.24, 15.14, 19.66	115.54^{ac}, 125.48, 125.48, 125.48, 155.28^{a}, 155.28^{a}, 42.39, 43.29, 44.2, 45.1^{ac}, 46.0, 46.91, 46.91, 46.91, 47.81, 53.23^{a}, 59.55^{a}, 64.97, 68.58, 71.29^{a}, 74.9, 74.9, 78.52, 84.84, 89.35, 90.26, 94.77	Nicholl et al. (2013); Quimby et al. (2018); Shivvers et al. (2019)
PTF12gty	0.1768	−11.2, -6.95	50.14, 54.39	Quimby et al. (2018)
PTF12hni	0.1056	−6.54, 2.51	20.35, 29.4	Quimby et al. (2018)
PTF12mxx	0.3296	−7.58, 8.21	37.89, 53.69	Quimby et al. (2018)
SCP06F6	1.189	-1.85^{e}, 10.02, 14.59	39.86^{e}, 51.74, 56.31	Barbary et al. (2009)
	1.5881	−7.93	11.85	Howell et al. (2013)
SNLS06D4eu	1.5	−4.2	15.48	Howell et al. (2013)
SNLS07D2bv				
SSS120810	0.156	6.52, 7.42, 12.54^{acd}, 23.81, 31.61, 38.55, 40.05^{a}, 56.72	31.58, 32.48, 37.6^{acd}, 48.88, 56.67, 63.61, 65.11^{a}, 81.78	Nicholl et al. (2014)
iPTF13ajg	0.7403	82.81, -5.68, -5.34, -5.11, -0.51^{ac}, 11.56^{a}, 12.7, 13.01, 28.22, 30.52^{a}, 30.52^{a}, 48.91	111.41, 22.92, 23.27, 23.5, 28.09^{ac}, 40.16^{a}, 41.31, 41.62, 56.82, 59.12^{a}, 59.12^{a}, 77.51	Vreeswijk et al. (2014)
iPTF13bdl	0.403	−33.09, -31.82, -30.76	112.4, 113.66, 114.73	De Cia et al. (2018); Schulze et al. (2021)
iPTF13bjz	0.2712	−0.19, 4.53	27.5, 32.22	De Cia et al. (2018); Schulze et al. (2021)
iPTF13cjq	0.3962	−3.13	13.43	Schulze et al. (2021)
iPTF13dcc	0.4305	37.7^{a}	96.92^{a}	Schulze et al. (2021)
iPTF13ehe	0.3434	−9.83, -6.1, 13.57	68.59, 72.32, 91.99	Yan et al. (2015); Schulze et al. (2021)
iPTF15eov	0.0535	−10.91, -9.9, -8.86, -5.2, 4.23^{e}, 11.91, 14.34, 27.05, -16.98, 34.66, 42.12, -14.6, 49.78, 53.48, -13.74, -12.24, 68.71	11.19, 12.2, 13.24, 16.9, 26.33^{e}, 34.01, 36.44, 49.15, 5.12, 56.75, 64.21, 7.5, 71.87, 75.58, 8.36, 9.86, 90.81	Taddia et al. (2019)
iPTF16asu	0.187	7.86, 9.57, 16.63, 19.13, 21.36, -1.38, 0.35	17.46, 19.17, 26.23, 28.74, 30.97, 8.22, 9.96	Taddia et al. (2019)
iPTF16bad	0.2467	94.89, 0.44, 2.87	116.73, 22.28, 24.71	Yan et al. (2017b)
iPTF16eh	0.427	54.75, 77.81, 79.95, 98.13^{ac}, 0.49, 6.8, 12.83, 37.17	100.94, 124.0, 126.14, 144.32^{ac}, 46.68, 52.99, 59.02, 83.36	Lunnan et al. (2018a)

APPENDIX B: BAYESIAN INFORMATION CRITERION

The Bayesian Information Criterion (BIC) is a statistical metric used for model selection (Schwarz 1978), based on Bayesian probability principles. It penalizes models with more parameters to prevent overfitting (Kass & Raftery 1995), favouring simpler models when possible. A lower BIC score indicates a better model. In this analysis, K-means clustering was applied to the first two components of the PCA parameter space, and BIC values were computed for cluster sizes ranging from one to five across all time bins and both binning schemes. The results, shown in Figs B1 and B2, indicate a smooth decrease in BIC values as the number of clusters increases, suggesting no strong evidence for distinct clusters.

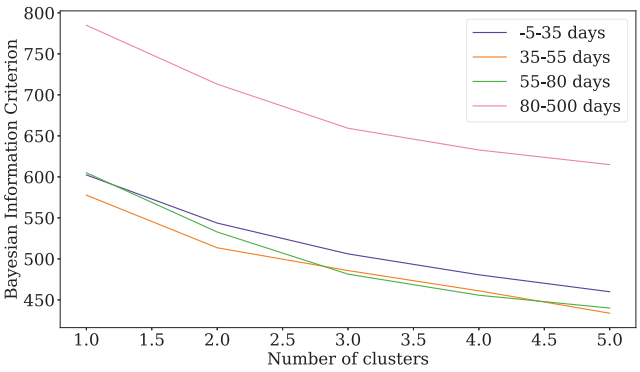

Figure B1. Bayesian information criterion (BIC) evaluated for varying numbers of clusters using KMeans clustering. Spectra have been split into varying time bins with phases relative to the peak of the light curve.

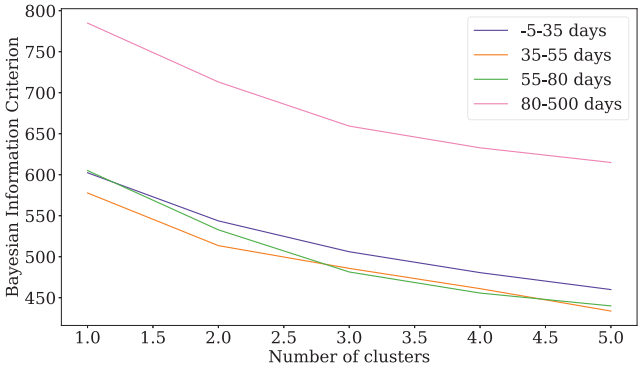

Figure B2. Bayesian information criterion (BIC) evaluated for varying numbers of clusters using KMeans clustering. Spectra have been split into varying time bins with phases relative to explosion and scaled by the median e-folding decline time (44 d).

APPENDIX C: THE EFFECT OF 'FAST' AND 'SLOW' EVENTS ON CLUSTERING

In Section 5, we discussed previous studies that identified spectral differences between fast and slow evolving SLSNe. To investigate whether similar trends appear in our sample, we repeat the analysis from Section 4, this time separating the two populations. The fast events are defined as those with an e-folding decline time of less than 30 d from Gomez et al. (2024), and slow events with a time greater or equal to 30 d.

Figs C1 and C2 show the component spectra from this decomposition represented in parameter space. This plots the coefficients of first few the PCA components against one another. Fast events are coloured in red, and slow events in blue. Here we see no correlation between the fast and slow events indicating there is no significant spectroscopic variation between these groups of SLSNe.

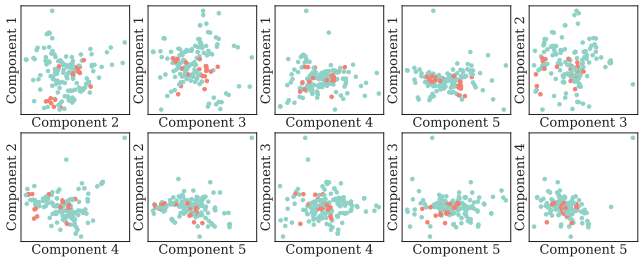

(a) Days -80 - -5

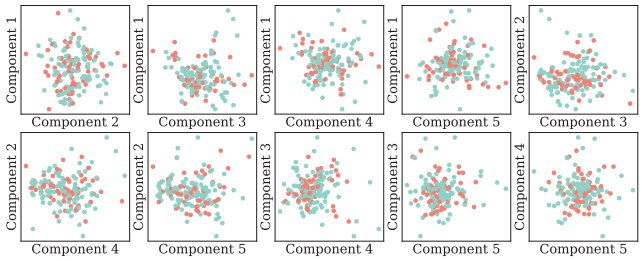

(b) Days -5 - 15

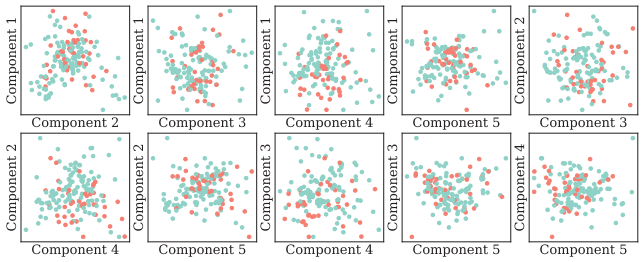

(c) Days 15 - 40

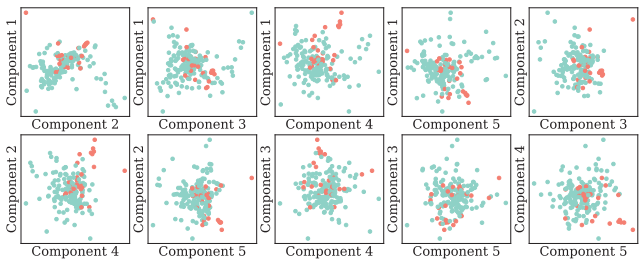

(d) Days 40 - 160

Figure C1. Representation of the SLSN photospheric spectra in the PCA parameter space in time bins relative to peak. Only the first five components for each bin are plotted for visualization. Events are split into fast and slow categories based on having an e-folding decline time in the light curve of above or below 30 d, and coloured red and blue respectively.

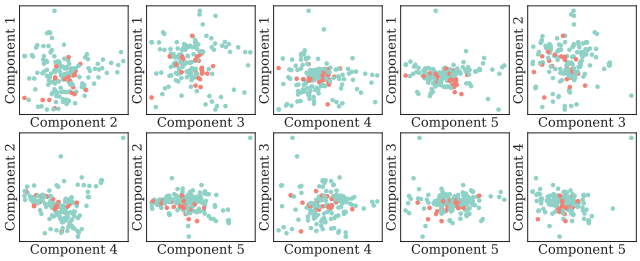

(a) Days 0 - 35

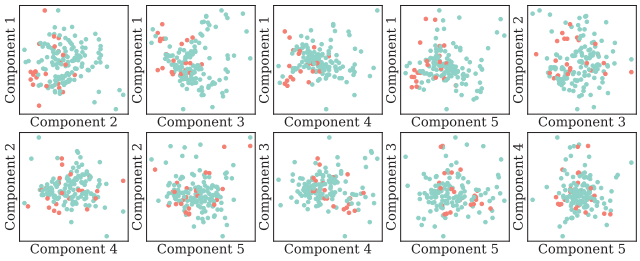

(b) Days 35 - 55

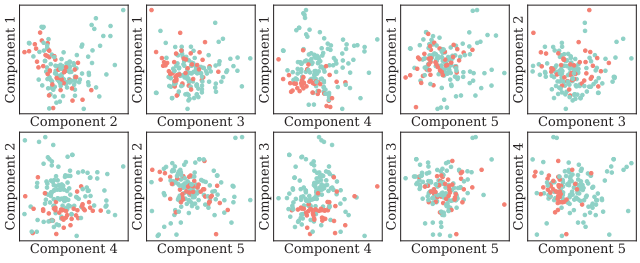

(c) Days 55 - 80

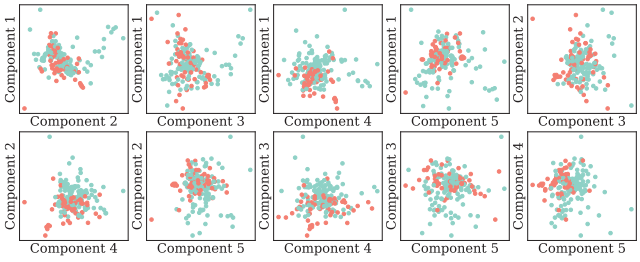

(d) Days 80 - 500

Figure C2. Representation of the SLSN photospheric spectra in the PCA parameter space in time bins relative to explosions with the phase scaled to match the median e-folding decline time of SLSNe (44 d). Only the first five components for each bin are plotted for visualization. Events are split into fast and slow categories based on having an e-folding decline time in the light curve of above or below 30 d, and coloured red and blue respectively.

APPENDIX D: THE EFFECT OF SN 2017EGM ON CLUSTERING

In Section 4, we performed PCA on different time bins in order to investigate spectral features and diversity of the population. We saw that at late times, the spectra of SN 2017egm deviated from the central clustering which was apparent when comparing the spectra to the average spectra generated. This resulted in the K-Means clustering favouring two separate clusters for the final time bin when grouping by scaled phase from explosion.

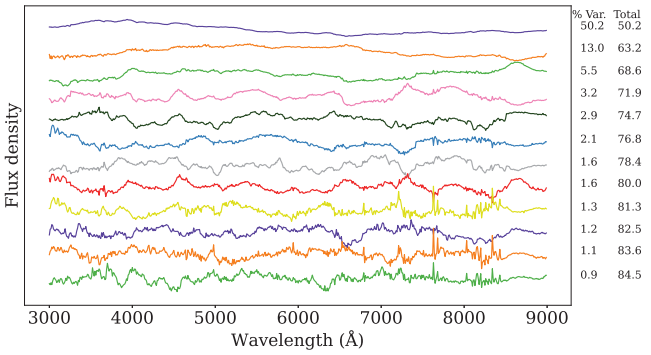

(a) PCA component spectra with the spectra of SN 2017egm removed, in the time bin 40 - 160 days relative to peak.

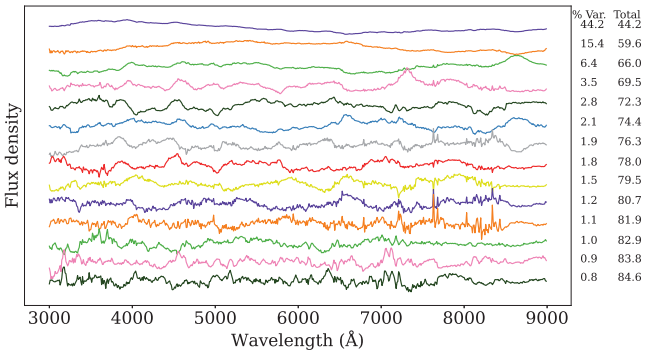

(b) PCA component spectra with the spectra of SN 2017egm removed, in the time bin 80 - 500 days relative to explosion with the phase scaled to match the median e-folding decline time of SLSNe (44 days).

Figure D1. PCA decomposition of SLSN spectra with the spectra of SN 2017egm removed. Explaining variations up to 85 per cent of the sample. More components are needed to explain the same level of variation with SN 2017egm removed supporting the idea that there is more diversity within the population at late times.

Here, we present the same analysis with the spectra from SN 2017egm removed from the final time bins in Section 4. This resulted in 170 spectra for the grouped by phase from peak bin, and 173 spectra in the grouped by scaled phases from explosion bin. Compared to their counterparts in Section 4.1, we can see many more components are needed to explain the same level of variation as shown in Table D1. However, the latter components in both binning schemes contribute $\lesssim 1$ per cent to the variation level. These smaller components also have few discernible features, appearing to be dominated by noise. This may signify the search for variation is limited by the noise in our data sample at this point. The largest component in both panels of Fig. D1 is a general blackbody shape and represents $\gtrsim 40$ per cent of the variation signifying the largest variation is due to the underlying blackbody. The increase in number of components needed with the spectra of SN 2017egm removed, reinforces the idea that the spectra of SN 2017egm were driving the diversity in the original sample. This is also seen by the lack of distinct groups in Fig. D2.

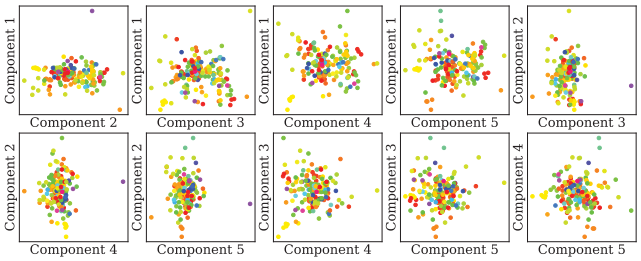

(a) PCA parameter space with the spectra of SN 2017egm removed, in the time bin 40 - 160 days relative to peak.

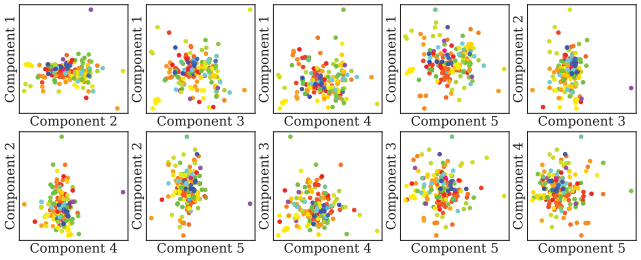

(b) PCA parameter space with the spectra of SN 2017egm removed. Explaining variations up to 85% of the sample. More components are needed to explain the same level of variation with SN 2017egm removed supporting the idea that there is more diversity within the population at late times.

Figure D2. Representation of the SLSNe photospheric spectra in the PCA parameter space without SN 2017egm. Only the first five components for each bin are plotted for ease of visualization. Each SLSN event is marked by a unique colour, consistent across all panels as well as Figs 16 and 17.

Table D1. The bins used for the PCA analysis using phases from peak and scaled phases from explosion, as well as the corresponding number of components needed to explain 85 per cent of the variation with and without the spectra of SN 2017egm included.

Time bin (d)	Components (all)	Components (without SN 2017egm)
40–160	8	12
80–500 (scaled)	8	14

[1]*Astrophysics Research Centre, School of Mathematics and Physics, Queen's University Belfast, Belfast BT7 1NN, UK*
[2]*Center for Astrophysics | Harvard & Smithsonian, 60 Garden Street, Cambridge, MA 02138-1516, USA*
[3]*The NSF AI Institute for Artificial Intelligence and Fundamental Interactions, Cambridge, MA 02138, USA*
[4]*European Southern Observatory, Alonso de Córdova 3107, Casilla 19, Santiago, Chile*
[5]*Millennium Institute of Astrophysics MAS, Nuncio Monsenor Sotero Sanz 100, Off. 104, Providencia, Santiago 7500011, Chile*
[6]*Graduate Institute of Astronomy, National Central University, 300 Jhongda Road, 32001 Jhongli, Taiwan*
[7]*Institute for Astronomy, University of Hawai'i, 2680 Woodlawn Drive, Honolulu HI 96822, USA*
[8]*Department of Physics, Lancaster University, Lancaster LA1 4YB, UK*
[9]*Institute of Space Sciences (ICE-CSIC), Campus UAB, Carrer de Can Magrans, s/n, E-08193 Barcelona, Spain*
[10]*Institut d'Estudis Espacials de Catalunya (IEEC), E-08860 Castelldefels (Barcelona), Spain*
[11]*The Oskar Klein Centre, Department of Astronomy, Stockholm University, Albanova University Center, SE-106 91 Stockholm, Sweden*
[12]*Astronomical Observatory, University of Warsaw, Al. Ujazdowskie 4, PL-00-478 Warszawa, Poland*
[13]*Department of Astronomy & Astrophysics, University of California, San Diego, 9500 Gilman Drive, MC 0424, La Jolla, CA 92093-0424, USA*
[14]*Cardiff Hub for Astrophysics Research and Technology, School of Physics & Astronomy, Cardiff University, Queens Buildings, The Parade, Cardiff CF24 3AA, UK*
[15]*Department of Physics, Royal Holloway, University of London, Egham TW20 0EX, UK*
[16]*Department of Physics, University of Warwick, Gibbet Hill Road, Coventry CV4 7AL, UK*
[17]*Tuorla Observatory, Department of Physics and Astronomy, University of Turku, FI-20014 Turku, Finland*
[18]*Finnish Centre for Astronomy with ESO (FINCA),University of Turku, FI-20014 Turku, Finland*
[19]*DTU Space, National Space Institute, Technical University of Denmark, Elektrovej 327, DK-2800 Kgs. Lyngby, Denmark*
[20]*Astrophysics Research Institute, Liverpool John Moores University, 146 Brownlow Hill, Liverpool L3 5RF, UK*
[21]*Max-Planck-Institut für Astrophysik, Karl-Schwarzschild Straße 1, D-85748 Garching, Germany*
[22]*School of Physics, Trinity College Dublin, The University of Dublin, Dublin 2, D02 PN40, Ireland*
[23]*Instituto de Ciencias Exactas y Naturales (ICEN), Universidad Arturo Prat, Santiago 8370133, Chile*
[24]*Instituto de Astrofisica, Departamento de Fisica, Facultad de Ciencias Exactas, Universidad Andres Bello, Fernandez Concha 700, Las Condes, Santiago 8370133 RM, Chile*
[25]*Center for Interdisciplinary Exploration and Research in Astrophysics (CIERA) and Department of Physics and Astronomy, Northwestern University, Evanston, IL 60208, USA*
[26]*Astrophysics sub-Department, Department of Physics, University of Oxford, Keble Road, Oxford OX1 3RH, UK*

This paper has been typeset from a TEX/LATEX file prepared by the author.